



Calhoun: The NPS Institutional Archive
DSpace Repository

Theses and Dissertations

1. Thesis and Dissertation Collection, all items

2010-09

A fully automated method of locating building shadows for aerosol optical depth calculations in high-resolution satellite imagery

Belson, Brian L.

Monterey, California. Naval Postgraduate School

<http://hdl.handle.net/10945/10553>

This publication is a work of the U.S. Government as defined in Title 17, United States Code, Section 101. Copyright protection is not available for this work in the United States.

Downloaded from NPS Archive: Calhoun



Calhoun is the Naval Postgraduate School's public access digital repository for research materials and institutional publications created by the NPS community. Calhoun is named for Professor of Mathematics Guy K. Calhoun, NPS's first appointed -- and published -- scholarly author.

Dudley Knox Library / Naval Postgraduate School
411 Dyer Road / 1 University Circle
Monterey, California USA 93943

<http://www.nps.edu/library>



NAVAL POSTGRADUATE SCHOOL

MONTEREY, CALIFORNIA

DISSERTATION

**A FULLY AUTOMATED METHOD OF LOCATING
BUILDING SHADOWS FOR AEROSOL OPTICAL DEPTH
CALCULATIONS IN HIGH-RESOLUTION SATELLITE
IMAGERY**

by

Brian L. Belson

September 2010

Dissertation Supervisor:

Philip A. Durkee

Approved for public release; distribution is unlimited

THIS PAGE INTENTIONALLY LEFT BLANK

REPORT DOCUMENTATION PAGE			<i>Form Approved OMB No. 0704-0188</i>	
Public reporting burden for this collection of information is estimated to average 1 hour per response, including the time for reviewing instruction, searching existing data sources, gathering and maintaining the data needed, and completing and reviewing the collection of information. Send comments regarding this burden estimate or any other aspect of this collection of information, including suggestions for reducing this burden, to Washington headquarters Services, Directorate for Information Operations and Reports, 1215 Jefferson Davis Highway, Suite 1204, Arlington, VA 22202-4302, and to the Office of Management and Budget, Paperwork Reduction Project (0704-0188) Washington DC 20503.				
1. AGENCY USE ONLY (Leave blank)		2. REPORT DATE September 2010	3. REPORT TYPE AND DATES COVERED Dissertation	
4. TITLE AND SUBTITLE: A Fully Automated Method of Locating Building Shadows for Aerosol Optical Depth Calculations in High-Resolution Satellite Imagery			5. FUNDING NUMBERS	
6. AUTHOR(S) Brian L. Belson			8. PERFORMING ORGANIZATION REPORT NUMBER	
7. PERFORMING ORGANIZATION NAME(S) AND ADDRESS(ES) Naval Postgraduate School Monterey, CA 93943-5000			10. SPONSORING / MONITORING AGENCY REPORT NUMBER	
9. SPONSORING / MONITORING AGENCY NAME(S) AND ADDRESS(ES) N/A			11. SUPPLEMENTARY NOTES The views expressed in this thesis are those of the author and do not reflect the official policy or position of the Department of Defense or the U.S. Government. IRB Protocol number _____.	
12a. DISTRIBUTION / AVAILABILITY STATEMENT Approved for public release; distribution is unlimited			12b. DISTRIBUTION CODE	
13. ABSTRACT (maximum 200 words) <p>Vincent (2006) developed a technique for remotely measuring Aerosol Optical Depth (AOD) using commercial high-resolution satellite imagery. This technique measured the radiance difference between a building shadow and an adjacent sunlit region with the same surface reflectance to calculate Total Optical Depth (TOD). AOD is then determined by subtracting Rayleigh scattering from TOD. The procedure for making this calculation was time consuming, particularly locating suitable shadows within the region of interest. This paper outlines a fully automated method of performing the AOD calculation and examining shadow properties. The automated method relies on high-resolution Digital Surface Model (DSM) data collected using a Light Detection and Ranging (LIDAR) sensor coupled with sun and satellite geometry to identify shadow regions. Configuration settings allowed for specific regions in the shadow and sunlit area to be selected before determining their respective radiances. Finally, a technique for aligning the satellite and DSM pixels was developed to correct for small differences between the datasets. Results from the automated method were compared with AERONET data for validation. The automated method using WorldView-1 and QuickBird imagery worked best at Solar Village, Saudi Arabia and an area northeast of Washington, D.C., which included the Goddard Space Flight Center. Testing of IKONOS multispectral imagery suggested the resolution is inadequate in urban settings. Testing in areas that included downtown regions in Houston, TX and Baltimore, MD identified weaknesses in the alignment algorithm.</p>				
14. SUBJECT TERMS aerosol, optical depth, aerosol optical depth, automated shadow detection, high resolution commercial satellite imagery, digital surface model, WorldView-1, QuickBird, IKONOS, BuckEye, LIDAR			15. NUMBER OF PAGES 145	
			16. PRICE CODE	
17. SECURITY CLASSIFICATION OF REPORT Unclassified	18. SECURITY CLASSIFICATION OF THIS PAGE Unclassified	19. SECURITY CLASSIFICATION OF ABSTRACT Unclassified	20. LIMITATION OF ABSTRACT UU	

THIS PAGE INTENTIONALLY LEFT BLANK

Approved for public release; distribution is unlimited

**A FULLY AUTOMATED METHOD OF LOCATING BUILDING SHADOWS FOR
AEROSOL OPTICAL DEPTH CALCULATIONS IN HIGH-RESOLUTION SATELLITE
IMAGERY**

Brian L. Belson
Major, United States Air Force
B.S., Tulane University, 1997
M.S., Air Force Institute of Technology, 2004

Submitted in partial fulfillment of the
requirements for the degree of

DOCTOR OF PHILOSOPHY IN METEOROLOGY

from the

**NAVAL POSTGRADUATE SCHOOL
September 2010**

Author:

Brian L. Belson

Approved by:

Philip A. Durkee
Professor of Meteorology
Dissertation Supervisor/
Committee Chair

Richard C. Olsen
Professor of Physics

Karl D. Pfeiffer
Assistant Professor of Meteorology

Kurt E. Nielsen
Research Assistant, Meteorology

Douglas L. Westphal
Naval Research Laboratory, Monterey, CA

Approved by:

Philip A. Durkee, Chair, Department of Meteorology

Approved by:

Douglas Moses, Vice Provost for Academic Affairs

THIS PAGE INTENTIONALLY LEFT BLANK

ABSTRACT

Vincent (2006) developed a technique for remotely measuring Aerosol Optical Depth (AOD) using commercial high-resolution satellite imagery. This technique measured the radiance difference between a building shadow and an adjacent sunlit region with the same surface reflectance to calculate Total Optical Depth (TOD). AOD is then determined by subtracting Rayleigh scattering from TOD. The procedure for making this calculation was time consuming, particularly locating suitable shadows within the region of interest. This paper outlines a fully automated method of performing the AOD calculation and examining shadow properties. The automated method relies on high-resolution Digital Surface Model (DSM) data collected using a Light Detection and Ranging (LIDAR) sensor coupled with sun and satellite geometry to identify shadow regions. Configuration settings allowed for specific regions in the shadow and sunlit area to be selected before determining their respective radiances. Finally, a technique for aligning the satellite and DSM pixels was developed to correct for small differences between the datasets. Results from the automated method were compared with AERONET data for validation. The automated method using WorldView-1 and QuickBird imagery worked best at Solar Village, Saudi Arabia and an area northeast of Washington, D.C., which included the Goddard Space Flight Center. Testing of IKONOS multispectral imagery suggested the resolution is inadequate in urban settings. Testing in areas that included downtown regions in Houston, TX and Baltimore, MD identified weaknesses in the alignment algorithm.

THIS PAGE INTENTIONALLY LEFT BLANK

TABLE OF CONTENTS

I.	INTRODUCTION.....	1
II.	BACKGROUND	3
A.	OTHER SATELLITE-BASED AOD RETRIEVAL METHODS.....	3
1.	Contrast Reduction Method.....	4
2.	Dark Object Method.....	5
3.	Multi-angle method.....	5
B.	THE SHADOW METHOD.....	5
1.	General Calculation	6
2.	Sensitivities	8
3.	Limitations and Target Selection Criteria.....	9
4.	Other Observations.....	9
C.	SHADOW DETECTION IN SATELLITE IMAGERY	10
III.	METHODOLOGY	11
A.	TARGET SELECTION CRITERIA TESTING	11
1.	Hypothesis I: It Is Important to Avoid Partial Shadow Pixels Along the Shadow Edge.....	12
2.	Hypothesis II: It Is Important to Choose Shadow Pixels Far from the Shadow Generator to Calculate Optical Depth.....	12
3.	Hypothesis III: Sky Dome Blockage Is Important When Choosing Valid Shadow and Sunlit Pixels for Calculating Optical Depth	13
4.	Hypothesis IV: Eliminating the Extreme Radiance Values from the Sample Improves AOD Calculations	13
5.	Hypothesis V: It Is Possible to Get an Idea of Uncertainty When Calculating AOD on Entire Scenes.	14
6.	Hypothesis VI: The DSM Can Have Significantly Lower Resolution Than the Satellite Data and Still Work Effectively	14
B.	TRIGONOMETRIC SHADOW DETECTION METHOD	15
1.	Preparation.....	16
2.	Identify Shadow and Sunlit Pixels.....	19
3.	Identify Coherent Shadows.....	20
4.	Correct for Pixel Offset Between DSM and Satellite File	21
5.	Eliminate Unwanted Pixels	23
a.	<i>Pixels That Are Too Close to the Building.....</i>	<i>23</i>
b.	<i>Pixels Whose Sky Dome Is Blocked by Adjacent Pixels.....</i>	<i>25</i>
c.	<i>Pixels That Are Too Close to the Shadow Edge</i>	<i>26</i>
d.	<i>Pixels with Elevation Issues or Extreme Radiances.....</i>	<i>27</i>
6.	Identify Accompanying Sunlit Pixels	29
7.	Calculate AOD for Each Shadow	30
C.	DATA	30
1.	Digital Surface Model (DSM)	31

2.	Satellite Data.....	32
3.	Output Data.....	34
4.	Validation Data	35
D.	COMPUTATIONAL TECHNIQUES AND TESTING	37
IV.	RESULTS	39
A.	TARGET SELECTION CRITERIA TESTS.....	39
1.	Rejection by Minimum Shadow Generator Height (GSFC).....	39
2.	Rejection of Edge Pixels	42
a.	North Satellite Dish, Solar Village.....	42
b.	Goddard Space Flight Center Building.....	44
3.	Rejection Due to Distance from Shadow Generator.....	47
a.	North Satellite Dish, Solar Village.....	48
b.	Goddard Space Flight Center Building.....	50
4.	Rejection Due to Sky Dome Blockage	54
a.	North Satellite Dish, Solar Village.....	55
b.	Goddard Space Flight Center Building.....	58
5.	Rejection of Extreme Radiances.....	64
a.	North Satellite Dish, Solar Village.....	64
b.	Goddard Space Flight Center Building.....	66
B.	WHOLE SCENE AOD CALCULATION.....	68
1.	Solar Village	68
a.	Multispectral Images	69
b.	Panchromatic Images	74
2.	Goddard Space Flight Center.....	78
a.	Multispectral Images	79
b.	Panchromatic Images	82
3.	Other Location Tests	84
a.	Tucson	84
b.	Baltimore and Houston.....	87
4.	Summary of Whole Scene AOD Calculations	91
C.	DSM RESOLUTION ADJUSTMENT	91
1.	Resolution Reduction for Solar Village Scene.....	92
2.	Resolution Reduction for GSFC Scene	95
V.	CONCLUSIONS	99
A.	SUMMARY	99
B.	FUTURE RESEARCH.....	100
APPENDIX A:	FORTTRAN CONFIGURATION VARIABLES.....	103
A.	GENERAL USE VARIABLES (CITY_VARS)	103
B.	SHADOW REGION VARIABLES (SHADOW_VARS)	103
C.	SUNLIT REGION VARIABLES (SUNLIT_VARS).....	103
D.	SHADOW/SUNLIT REGION VARIABLES (SHADNON_VARS)	104
E.	MISCELLANEOUS VARIABLES (MISC_VARS)	104
F.	VARIABLES FOR DOME BLOCKAGE CALCULATION (DOME_VARS).....	105

G.	AOD CALCULATION VARIABLES	105
APPENDIX B:	LIST OF BASELINE USER-DEFINED VARIABLES FOR SHADOW CHARACTERIZATION TESTS (SOLAR VILLAGE).....	107
APPENDIX C:	LIST OF BASELINE USER-DEFINED VARIABLES FOR SHADOW CHARACTERIZATION TESTS (GSFC BUILDING)	109
APPENDIX D:	LIST OF USER-DEFINED VARIABLES FOR SOLAR VILLAGE AOD CALCULATIONS	111
APPENDIX E:	LIST OF USER-DEFINED VARIABLES FOR BUCKEYE FILE AOD CALCULATIONS	113
LIST OF REFERENCES		115
INITIAL DISTRIBUTION LIST		119

THIS PAGE INTENTIONALLY LEFT BLANK

LIST OF FIGURES

Figure 1.	Aerosol optical depth at $0.55\ \mu m$ using the MODIS sensor (from IPCC 2007).	3
Figure 2.	Depiction of the difference between the shadow and sunlit signal received by a high-resolution satellite. Subtracting the two signals isolates the direct transmission component of the signal, which can be used to calculate total optical depth (from Vincent 2006).	6
Figure 3.	Example of pixel rejections from FASTEC. Orange represents the building, black is the shadow, and gray is rejected shadow. Panel 1 is the full shadow, 2 is after edge rejection, and 3 is after building proximity rejection.....	12
Figure 4.	Trigonometric approach employed by FASTEC to find shadow pixels based on elevation. Red arrows indicate shadow pixels whose path to the sun is blocked by a higher elevation pixel. The green arrow indicates an unblocked sunlit pixel. Black pixels are obstructed from view of the satellite by the building.....	15
Figure 5.	Top-level flowchart of FASTEC.	16
Figure 6.	Relative spectral response for the QuickBird satellite derived from data provided by DigitalGlobe.	18
Figure 7.	Calculation of in-shadow pixel $h(r_{tar}, c_{tar})$. The height of the beam (h_b) between the target pixel and the sun is less than the height of pixel $h(r_{los}, c_{los})$. Diff is the difference between $h(r_{los}, c_{los})$ and h_b	19
Figure 8.	Four-panel plot of offset between satellite and DSM files for Goddard Space Flight Center on October 26, 2006. In Panels A and B, green is shadow and yellow is partial shadow pixels. Panel A displays the results from FASTEC and B displays the results from a by-hand analysis of the satellite file. Panels C displays overlap between A and B without offset correction (162 pixels). Panel D displays overlap with offset correction (218 pixels).	22
Figure 9.	Identifying pixels by proximity to shadow generator. h_{bldg} is the height of the building, h_b is the height of the line-of-sight between the target pixel and sun, $dist_{pix}$ is the distance from the shadow generator to the target pixel, $dist_{max}$ is the farthest extent of shadow, and p_{user} is the percentage of pixels to mark <i>invalid</i>	24
Figure 10.	Celestial dome blockage. The dark line depicts the angle representing dome blockage along that azimuth.	25
Figure 11.	Example of shadow radiances from FASTEC. Spectral radiance values are units of $W\ m^{-2}\ sr^{-1}\ nm^{-1}$ (RU). Building location is estimated.	27
Figure 12.	Histogram of radiance values with extreme radiance rejection. The actual distribution is not necessarily normal as depicted in this graphic.	28
Figure 13.	Region for sunlit pixel search.	29

Figure 14.	Examples of input data used in this research. Both images are over the Goddard Space Flight Center (GSFC) near Washington D.C. The QuickBird satellite image is from October 26, 2006.	30
Figure 15.	Nearest neighbor method. In this example, radiance is assigned to a 1 m resolution DSM pixel (solid box) using the radiances of four surrounding 2.4m satellite pixels (hatched boxes).	32
Figure 16.	Third order polynomial best fit curve with raw AERONET data points.	36
Figure 17.	Satellite image of area used for hand-generated DSM (image captured from Google maps). The labeled objects were the only structures built into the DSM.	37
Figure 18.	Plot of computation time vs. number of processors. Test case found more than 50,000 shadows in 25 km ² DSM file with AOD calculations on 3015 shadows.	38
Figure 19.	Number of tree/building shadows vs. minimum shadow generator height from October 26, 2006 GSFC QuickBird image.	40
Figure 20.	Minimum shadow generator height vs. 50th percentile of AOD. Computed for all shadow generators from the October 26, 2006 GSFC image. Error bars are the 25th and 75th percentile, plus symbols are the minimum and maximum AOD (maximum exceeds 0.35 in some cases), and the dotted line is ground truth.	41
Figure 21.	Example of edge rejection algorithm on Solar Village north satellite dish (for April 12, 2006 image) and GSFC building (for January 16, 2009 image). Dark grey pixels are full shadow pixels, light grey are rejected due to proximity to shadow edge, and yellow approximate the shadow generator.	42
Figure 22.	Average pixel radiance versus proximity to shadow edge for the north satellite dish with the April 12, 2006 Solar Village image. The x-axis is the distance from the shadow edge (in pixels) with zero marking the shadow edge, error bars are one standard deviation, and plus symbols are the max and min radiance.	43
Figure 23.	Average pixel radiance vs. proximity to shadow edge for the GSFC building on January 16, 2009. The x-axis is the distance from the shadow edge (in pixels) with zero marking the shadow edge, error bars are one standard deviation, and plus symbols are the max and min radiance.	45
Figure 24.	Aerosol optical depth vs. edge pixel rejection setting for October 26, 2006 GSFC image. The black box is the 50th percentile, the error bars are the 25th and 75th percentile, the plus symbols are the max and min, and the dashed line is ground truth.	47
Figure 25.	Example of target pixel rejection based on proximity to the shadow generator. Yellow indicates building pixels, dark grey indicates shadow pixels, and light grey indicates eliminated shadow pixels. Created using north satellite dish in Solar Village on April 12, 2006 (top panels) and the GSFC building on January 16, 2009 (bottom panels).	48
Figure 26.	Spectral radiance vs. distance from the shadow generator (binned) for the Solar Village north satellite dish on April 12, 2006. For each bin, the box	

	marks the 50th percentile, error bars are the 25th and 75th percentile, and plus signs are the maximum and minimum.	49
Figure 27.	Spectral radiance vs. distance from the shadow generator (binned) for GSFC building on January 16, 2009. For each bin, the box marks the 50th percentile, error bars are the 25th and 75th percentile, and plus signs are the maximum and minimum.	51
Figure 28.	Plot of spectral radiance by pixel for the GSFC building from January 16, 2009. The GSFC building surrounds all sides except the southwest. The sun is located to the southeast.	52
Figure 29.	AOD vs. percent of building shadow used for the October 26, 2006 GSFC image. The black box is the 50th percentile, the error bars are the 25th and 75th percentile, the plus symbols are the max and min, and the dashed line is ground truth.	54
Figure 30.	Example of sky dome blockage for the January 16, 2009 image of the GSFC building. Yellow is building pixels, dark grey is valid shadow pixels, and light grey is invalid shadow pixels from 30% or greater sky dome blockage.	55
Figure 31.	Sky dome blockage test using April 12, 2006 Solar Village image. Grey region is shadow pixels identified by the automated method. Numbers mark geometrically relevant information for the calculation on the highlighted pixel.	56
Figure 32.	Spectral radiance of sky dome blockage bins for the April 12, 2006 Solar Village image. For each bin, the box (shadow) or diamond (sunlit) is the 50th percentile, error bars are the 25th and 75th percentile, plus symbols are the maximum, and “x” symbols are minimum radiances.	57
Figure 33.	Shadow used for sky dome blockage testing for Goddard Space Flight Center building, January 16, 2009 image.	58
Figure 34.	Spectral radiance of sky dome blockage bins for the GSFC building on January 16, 2009. For each bin, the box (shadow) or diamond (sunlit) is the 50th percentile, error bars are the 25th and 75th percentile, plus symbols are the maximum, and minus symbols are the minimum radiances.	59
Figure 35.	AOD vs. sunlit pixel sky dome blockage maximum thresholds for the GSFC DSM file from January 16, 2009. For each threshold, the box is the 50th percentile, the error bars are the 25th and 75th percentile, and plus symbols mark the maximum and minimum AOD.	62
Figure 36.	AOD vs. shadow pixel sky dome blockage maximum thresholds for the GSFC DSM file from January 16, 2009. Boxes are the 50th percentile, the error bars are the 25th and 75th percentile, and + symbols mark the max and min AOD.	63
Figure 37.	Spectral radiance of usable pixels for shadow and sunlit regions for Solar Village north satellite dish and the April 12, 2006 satellite image.	65
Figure 38.	Spectral radiance of usable pixels for shadow and sunlit regions for GSFC building and the January 16, 2009 image.	67

Figure 39.	Aerosol optical depth using different extreme radiance rejection percentages on the GSFC DSM file and the October 26, 2006 image. For each threshold, the box is the 50th percentile, the error bars are the 25th and 75th percentile, plus symbols mark the maximum and minimum, and the dotted line marks ground truth AOD.	68
Figure 40.	Manually created DSM for Solar Village. The (1) north and (2) south satellite dishes were estimated to be 13 meters tall and the building was estimated to be 4 meters tall.....	69
Figure 41.	Multi-spectral imagery for Solar Village testing on (A) October 19, 2005, (B) April 12, 2006, (C) April 30, 2006, (D) May 26, 2007, and (E) November 30, 2007 with 2.4 meter resolution QuickBird data.....	70
Figure 42.	Blue channel AOD results for Solar Village satellite dishes.....	72
Figure 43.	Green channel AOD results for Solar Village satellite dishes.....	72
Figure 44.	Red channel AOD results for Solar Village satellite dishes.....	73
Figure 45.	Near-Infrared channel AOD results for Solar Village satellite dishes.....	73
Figure 46.	Panchromatic imagery for Solar Village testing on (A) October 19, 2005, (B) April 12, 2006, (C) April 30, 2006, (D) May 26, 2007, (E) November 30, 2007, (F) June 26, 2008, (G) October 11, 2008, (H) October 14, 2008, (I) December 14, 2008.....	75
Figure 47.	Panchromatic channel AOD results for Solar Village satellite dishes.....	77
Figure 48.	Panchromatic channel bias-adjusted AOD results for Solar Village satellite dishes.....	77
Figure 49.	BuckEye DSM tile over the Goddard Space Flight Center with zoomed in view of three buildings identified as shadow generators by FASTEC. Green dots are shadow regions with sun to SE. Red dot marks location of AERONET site.	78
Figure 50.	Examples of multispectral imagery for GSFC BuckEye file testing from October 26, 2006 (left) and February 8, 2009 (right). Images are approximately equivalent to the zoomed in region in Figure 49.	79
Figure 51.	50th percentile value of AOD vs. AERONET value for GSFC multispectral channels from October 26, 2006 QuickBird image. Error bars on the y-axis reflect the reported accuracy of AERONET data (0.02) and error bars on x-axis are one standard deviation of the values reported on that day and scene. n=8.....	80
Figure 52.	Plot of blue channel AOD vs. the other channels for the October 26, 2006 GSFC image.....	82
Figure 53.	Examples of panchromatic imagery for GSFC BuckEye file testing from (A) October 26, 2006, (B) March 5, 2008, (C) May 25, 2008, and (D) January 16, 2009. Images are approximately equivalent to the zoomed in region in Figure 49.....	83
Figure 54.	50th percentile value of AOD vs. AERONET value for GSFC panchromatic images. Error bars on the y-axis reflect the reported accuracy of AERONET data (0.02) and error bars on x-axis are one standard deviation of the values reported for that day and scene.	84

Figure 55.	DSM file for Tucson testing. The inset is the area around the AERONET station, the bright area in the southwest corner is caused by mountains.	85
Figure 56.	November 1, 2005 1815Z imagery for Tucson. Image (A) is the four-meter resolution blue channel and (B) is the one-meter resolution panchromatic channel. The area in each image roughly matches the zoomed in area in Figure 55.....	86
Figure 57.	Histogram of blue channel AOD computation error for November 1, 2005 image. Ground truth AOD was 0.046.	87
Figure 58.	Baltimore DSM. The zoomed in region shows good shadow generators near the Maryland Science Center AERONET station.....	88
Figure 59.	Houston DSM. The zoomed in region shows good shadow generators near the University of Houston AERONET station.....	88
Figure 60.	Multispectral QuickBird image of Houston downtown area from January 25, 2004 at 1647Z. Note the complexity of shadows cast by the tall buildings.....	89
Figure 61.	Panchromatic QuickBird image of Baltimore from January 1, 2004 at 1540Z. Note the complexity of shadows cast by the tall buildings and the optically dark Chesapeake Bay.....	90
Figure 62.	Example of resolution adjustment methods. Box A represents a full resolution DSM, box B and C halve the horizontal resolution using method one (sampling) and two (smoothing) respectively. Gray shading is by elevation.....	92
Figure 63.	Examples of top left 30 x 30 pixel region in Solar Village DSM after resolution adjustment methods applied.....	93
Figure 64.	Examples of top left 201 x 201 pixel region in GSFC DSM after resolution adjustment methods applied.....	96

THIS PAGE INTENTIONALLY LEFT BLANK

LIST OF TABLES

Table 1.	List of Molecular Rayleigh Optical Depth and Spectral irradiance constants by satellite and channel.	18
Table 2.	List of contents of DSM array output files.	35
Table 3.	AOD with varying edge pixel rejection setting for the north satellite dish in the April 12, 2006 Solar Village image. Ground truth AOD was 0.243. ...	44
Table 4.	AOD with varying edge pixel rejection setting for the GSFC building using January 16, 2009 image. Ground truth was 0.036.	46
Table 5.	Results of varying proximity to building threshold percentage for north satellite dish from April 12, 2006 Solar Village image. Ground truth is 0.246.	50
Table 6.	Results of varying proximity to building threshold percentage for GSFC building wing from January 16, 2009 GSFC image. Ground truth is 0.036. ...	53
Table 7.	Results of varying shadow sky dome blockage maximum threshold for January 16, 2009 image of GSFC building wing. Ground truth is 0.036.	60
Table 8.	Results of varying the sunlit sky dome blockage maximum threshold for January 16, 2009 image of GSFC building wing. Ground truth is 0.036.	61
Table 9.	Offset correction values for different shadow sky dome blockage thresholds for January 16, 2009 image over the GSFC DSM. Baseline offset correction determined by disabling the sky dome blockage maximum threshold.	63
Table 10.	Results of varying extreme radiance thresholds for Solar Village north satellite dish shadow region and the April 12, 2006 satellite image.	65
Table 11.	Results of varying extreme radiance thresholds for Solar Village north satellite dish sunlit region and the April 12, 2006 satellite image.	66
Table 12.	Date, time, sun azimuth, offset correction, and pixel counts for the satellite dish shadows in the Solar Village multispectral imagery.	71
Table 13.	Multispectral channel-specific error bias and error standard deviation Solar Village shadows.	74
Table 14.	Date, satellite, time, sun azimuth and elevation, offset correction, and pixel counts for the satellite dish shadows in the Solar Village panchromatic imagery.	76
Table 15.	Multispectral channel-specific error bias and standard deviation for October 26, 2006 GSFC shadows.	81
Table 16.	Date, time, sun azimuth and elevation, offset correction, shadow count, and average pixel counts for the satellite dish shadows in the Solar Village panchromatic imagery.	83
Table 17.	Results of Solar Village resolution reduction using sampling approach and the multispectral channels. x=insufficient pixels for calculation.	94
Table 18.	Results of Solar Village resolution reduction testing using sampling approach and the panchromatic channel. x=insufficient pixels for calculation.	95
Table 19.	Results of October 26, 2006 GSFC multispectral resolution reduction testing.	97

THIS PAGE INTENTIONALLY LEFT BLANK

LIST OF ACRONYMS AND ABBREVIATIONS

AERONET	Aerosol Robotic Network
AOD	Aerosol Optical Depth
ATSR-2	Along Track Scanning Radiometer 2
AVHRR	Advanced Very High Resolution Radiometer
BL	Bottom Left
BR	Bottom Right
CE90	Circular Error of 90%
DN	Digital Number
DSM	Digital Surface Model
FASTEC	Fully Automated Shadow TEChnique
FORTAN	FORmula TRANslation
GCP	Ground Control Point
GSFC	Goddard Space Flight Center
IDL	Interactive Data Language
IPCC	Intergovernmental Panel on Climate Change
LE90	Linear Error of 90%
LIDAR	LIght Detection And Ranging
LINUX	Linus Torvald's UNIX
MAR	Mean Aerosol Reflectance
MISR	Multi-angle Imaging Spectro-Radiometer
MODIS	MODerate resolution Imaging Spectrometer
MROD	Molecular Rayleigh Optical Depth
NIR	Near-Infrared
POI	Principals-of-Invariance
POLDER	Polarization and Directionality of the Earth's Reflectances
RGB	Red, Green, Blue
RU	Radiance Units ($\text{W m}^{-2} \text{sr}^{-1} \text{nm}^{-1}$)
TEC	Topographic Engineering Center
TL	Top Left
TOA	Top-of-Atmosphere
TOD	Total Optical Depth
TOMS	Total Ozone Mapping Spectrometer
TR	Top Right
RU	Spectral Radiance Units ($\text{W m}^{-2} \text{sr}^{-1} \text{nm}^{-1}$)

THIS PAGE INTENTIONALLY LEFT BLANK

LIST OF SYMBOLS

δ_0	Total optical depth
μ	Cosine of sensor zenith angle
μ_0	Cosine of solar zenith angle
r_s	Surface reflectance
\bar{r}	Mean aerosol reflectance
F_0	Spectral solar irradiance
L_d	Radiance difference
$\tilde{\omega}$	Single scatter albedo
P	Scattering phase function
Θ	Scattering angle
g	Asymmetry parameter
(μ', ϕ')	Cosine of incident zenith and azimuth angles
(μ'', ϕ'')	Cosine of resultant zenith and azimuth angles
δ_R	Rayleigh optical depth
H	Height above sea level
λ	Wavelength
p	Atmospheric pressure
p_0	Sea-level reference pressure (1013.25 hPa)
C_1, C_2, C_3	Color space indices
L_λ	Spectral radiance
$\phi(\lambda)$	Channel-specific spectral response
r_{tar}, c_{tar}	Row and column of target pixel
r_{los}, c_{los}	Row and column of line-of-sight pixel
$h(r, c)$	Height of pixel at row and column (r, c)
θ	Angle
r_s, c_s	Row and column of satellite pixel
r, c	Row and column of elevation file pixel
ϕ, λ	Latitude and longitude of pixel
w_{TL}	Inverse weight of surrounding pixel to TL, TR, BL, BR
W_{tTL}	Final weight of surrounding pixel to TL, TR, BL, BR

THIS PAGE INTENTIONALLY LEFT BLANK

ACKNOWLEDGMENTS

I would like to thank my Committee Chairman, Prof. Phillip Durkee for his guidance and weekly pep talks particularly during the early, difficult stages of my work. I would like to thank the other members of my committee, Kurt Nielsen, Lt Col Karl Pfeiffer, and Dr. Doug Westphal for suggestions that significantly improved this paper. Finally, I must offer special thanks to Dr. Olsen for planting the seed that blossomed into the foundation of FASTEC.

Many other people assisted me throughout this research. Notably, Steve Sarigianis and a host of others at the Topographic Engineering Center responded to every request for DSM data promptly. I could not have even started this project without them. Mr. Bob Creasey also helped me immensely in the lab. My mentor and friend, Lt Col T.C. Moore edited the early, ugly editions of my dissertation and managed to do so with class. I'd also like to thank my mother, father, and two brothers who also willingly suffered through editing the early versions of my paper and greatly improved the readability of it.

It is hard to quantify how important my fellow PhD students, Majors Mark Allen, Lou Lussier, Cedrick Stubblefield, and Darren Murphy, have been to me during the past three years. With the friendship, help, and regular banter down in PhD corner they've made this much more enjoyable than it is supposed to be. I want to especially thank my office mate and long time friend Major Scott Miller for being there from start to finish. We studied and tested together, bounced ideas off each other, and spent as much time together as we did with our families. I believe he knows my project almost as well as I know it.

Lastly, to my beautiful wife Michelle and our two lovely daughters, Audrey and Brenna, you are the best part of my life and I am grateful to have shared this journey with you.

THIS PAGE INTENTIONALLY LEFT BLANK

I. INTRODUCTION

Aerosols play an important part in the earth's radiation budget directly (through scattering and absorption of incoming solar radiation and outgoing longwave radiation) and indirectly (by affecting cloud properties) (IPCC 2007). The overall impact depends on the aerosol optical properties that vary with wavelength, relative humidity, and the horizontal and vertical distribution, all of these varying with time (Hayward and Boucher 2000, IPCC 2001). Although aerosols can contribute positively to global heating, their overall effect is a net cooling effect. This cooling counteracts 25–50% of the heating from anthropogenic greenhouse gases (IPCC 2007). Similarly, aerosols significantly attenuate transmission of electromagnetic radiation in the visible and near-infrared (NIR) through scattering and absorption, limiting the effectiveness of intelligence collection and weapon systems that operate in those portions of the spectrum by reducing the amount of radiation reaching the sensors. Aerosol optical depth (AOD) is a measure of the opacity of the atmosphere due to aerosols. It is wavelength-dependent and is directly proportional to the size and concentration of the aerosol particles present. Accurately characterizing the radiative forcing due to aerosols is important when running climate models (IPCC 2007). However, the significant spatial and temporal variability makes it difficult to directly measure aerosol properties (size and concentration) in the atmosphere globally. As a result, numerous algorithms using satellite imagery to determine aerosol properties have been developed.

Most satellite techniques for characterizing aerosols with visible and NIR wavelength sensors rely on surfaces with low reflectance in the visible channels or over surfaces where detailed knowledge of the surface reflectance exists. A few satellites (Polarization and Directionality of the Earth's Reflectance – POLDER and Multi-angle Imaging Spectro-Radiometer – MISR) have dedicated sensors for measuring aerosol properties (IPCC 2007). These sensors use multiple look angles to model the atmosphere but are limited to low surface reflectance regions (Veefkind et al. 1998, Martonchik et al. 2004, Deuze et al. 2000). Vincent (2006) developed a technique to characterize aerosols using commercial high-resolution satellite data in the visible and NIR portions of the

spectrum, over any terrain, without prior knowledge of or constraints on surface reflectance. This technique, henceforth referred to as the shadow technique or method, compares the radiance inside the shadow with radiance just outside the shadow (sunlit) to calculate AOD. Although promising, Vincent's method was labor intensive, making large case studies and practical application difficult. Since that time, additional research has refined the technique and sped up the process (Rivenbark 2009, Sweat 2008, Dombrock 2007, Evans 2007). However, those efforts stopped well short of full automation.

This research develops and tests a method called the Fully Automated Shadow Technique, or FASTEC, of fully automating the shadow technique for any sensor or wavelength provided a high resolution surface elevation map is available. In addition to identifying and calculating AOD for specific shadows or every usable shadow in an image, FASTEC enables detailed examination of shadow and sunlit region characteristics for determining pixel selection criteria. Chapter II describes the shadow technique as developed by Vincent (2006). It also lists and briefly describes other methods of measuring AOD. Chapter III outlines the automated approach and its implementation. Chapter IV details the results of testing the automated method. Chapter V discusses conclusions and offers suggestions for future research with the automated method.

II. BACKGROUND

A. OTHER SATELLITE-BASED AOD RETRIEVAL METHODS

Numerous satellite-based techniques for measuring AOD exist. These techniques typically work with specific wavelength bands, minimum horizontal resolutions, and surface reflectance ranges. Figure 1 is a global seasonal average composite of AOD from the Moderate Resolution Imaging Spectrometer (MODIS) sensor, demonstrating the high spatial and seasonal variability of AOD globally. Additionally, Figure 1 shows large areas where AOD is not calculated because existing MODIS techniques do not work over desert or snow-covered regions due to high surface reflectance.

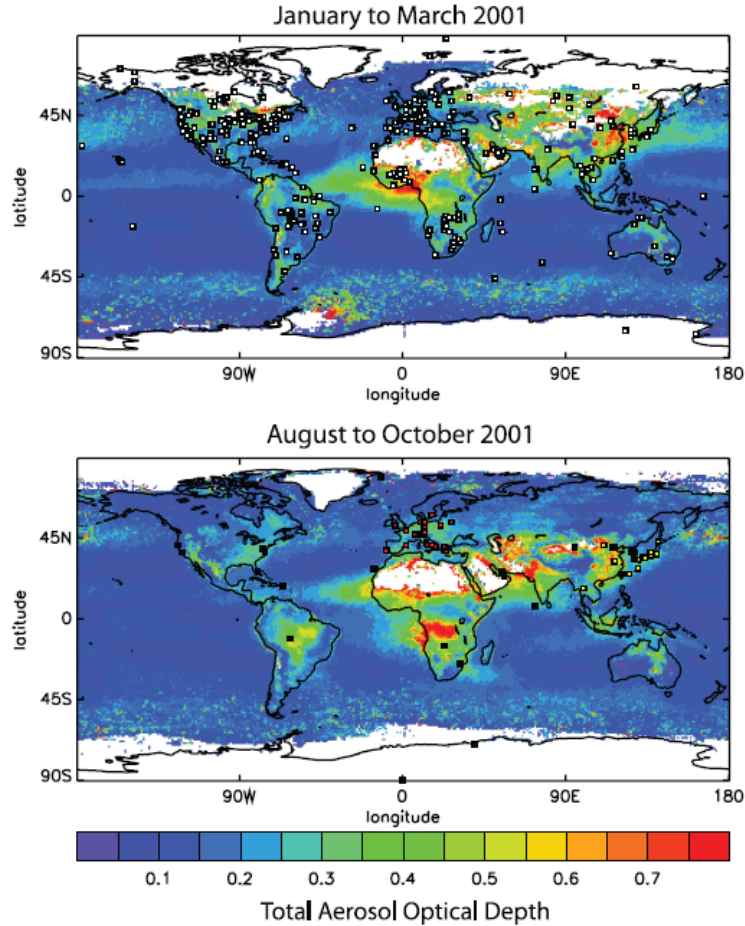


Figure 1. Aerosol optical depth at $0.55 \mu\text{m}$ using the MODIS sensor (from IPCC 2007).

Surface reflectance is negligible over water for near-Infrared (NIR) wavelengths and AOD is calculated using the dark object method, which is described in Chapter II.A.2 (von Hoyningen-Huene 2003). Here total optical depth (TOD) is computed by treating the low surface reflectance as negligible and assuming all radiance received by the satellite is scattered spaceward by aerosol particles and gases. After removing the contribution from Rayleigh scattering (depends on surface pressure), the contribution from aerosol scattering dominates the remaining signal. Over land, determining optical depth is less straightforward since the contribution from surface reflectance is non-zero and varies significantly with surface type and wavelength. To calculate AOD over land, more complex methods like contrast reduction, dark object, and multi-angle were developed, and these are described as follows:

1. Contrast Reduction Method

The contrast reduction method computes optical depth from the measured radiance difference between a distinct surface and its surrounding area (Odell and Weinman 1975). It requires prior knowledge of the two surface albedos, sun and satellite zenith angles, and lookup tables based on the mean surface albedo, the viewing zenith angle, and a contrast transmission function to compute optical depth. As defined by Odell and Weinman (1975), the contrast transmission function is proportional to the difference between the reflected radiance off the surfaces and inversely proportional to the difference between their surface albedos. Odell and Weinman (1975) showed that it is possible to exploit shadows cast by large objects to determine optical depth without prior knowledge of the surface features. This forms the basis of the shadow method developed by Vincent (2006). Later, Kaufman and Joseph (1982) applied a similar approach for regions where the surface reflectance undergoes a step-wise change, such as along a shoreline or forest border, to compute optical depth and surface reflectivity. This eliminates the previous requirement that surface reflectance be known. Additionally, using two different surface regions allows this approach to be independent of satellite calibration and produces more accurate results than earlier contrast reduction methods.

2. Dark Object Method

The dark object method is usable for wavelengths with low surface reflectance. In such locations it is possible to estimate the small portion of the top-of-atmosphere (TOA) signal, which is due to surface reflection. Kaufman and Sendra (1988) detail a rapid, automated algorithm to compute optical thickness, using the dark object method over regions covered by dark vegetation. Their approach assumes the surface reflectance of those regions to estimate optical thickness and was accurate to within 0.20 for band 1 (0.5-0.6 μm) and 0.05 for band 2 (0.6-0.7 μm). The dark object method is ineffective over surfaces with high surface reflectance, such as snow or sand. Other dark object algorithms, such as that described by von Hoyningen-Huene et al. (2003), employ the same fundamental idea.

3. Multi-angle method

Multi-angle methods use special sensors that examine a region from multiple look angles. Sensors such as POLDER, MISR, or Along Track Scanning Radiometer 2 (ATSR-2) characterize aerosols by using the different look angles to measure surface reflectance and use lookup tables to model the atmosphere (Veefkind et al. 1998, Martonchik et al. 2004, Deuze et al. 2000). For example, the dual view algorithm, developed by Veefkind et al. (1998), uses two look angles to separate the atmospheric and surface contributions to the satellite radiance. The multi-angle method, though quite accurate, includes a step in the algorithm to identify and ignore regions with high surface reflectance (Robles Gonzalez et al. 1997).

B. THE SHADOW METHOD

Except where otherwise cited, the information provided in this description of the shadow method was taken from Vincent (2006). The shadow method exploits high-resolution imagery to measure the radiance difference between building shadows and adjacent sunlit regions to calculate total optical depth. Several commercially-available satellites have sufficient horizontal resolution, from 46 cm for the WorldView-1 panchromatic channel to 2.44 m for the QuickBird multispectral channels (DigitalGlobe,

cited June 2010a/b), to use the shadow method. Figure 2 depicts the basic components of radiance received at a satellite, from a shadow and an adjacent sunlit region where both occur over an identical surface. Direct transmission, diffuse transmission, and diffuse reflection components make up the sunlit signal, while the shadow signal lacks the direct transmission component. For a homogeneous surface, where a portion is covered by shadow, subtracting the shadow radiance from the sunlit radiance isolates the direct transmission component of the signal, the portion of the signal that is the key to calculating optical depth.

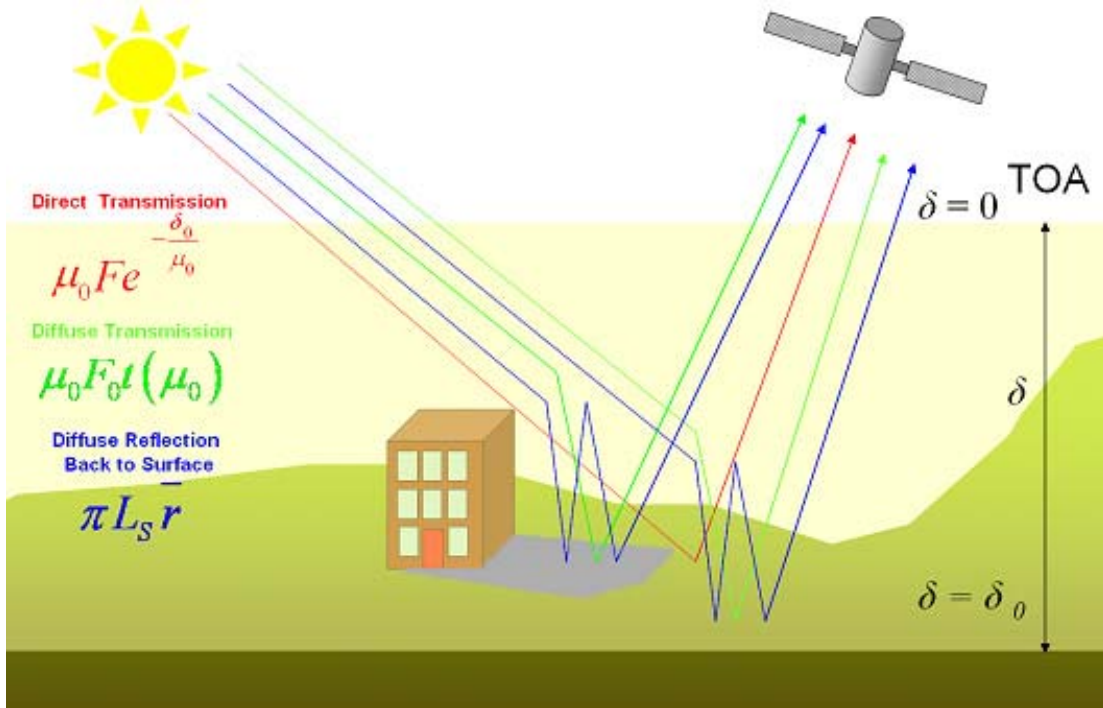


Figure 2. Depiction of the difference between the shadow and sunlit signal received by a high-resolution satellite. Subtracting the two signals isolates the direct transmission component of the signal, which can be used to calculate total optical depth (from Vincent 2006).

1. General Calculation

The equation for calculating TOD is derived from Liou's (2002) development of the principles-of-invariance (POI) method to describe the multi-scattering problem. Vincent (2006) provides a detailed derivation of the governing equation:

$$\delta_0 = \left(\frac{\mu_0 \mu}{\mu + \mu_0} \right) \ln \left[\left(\frac{r_s}{1 - r_s \bar{r}} \right) \left(\frac{\mu_0 F_0}{\pi L_d} \right) \right] \quad (1)$$

where δ_0 is total optical depth, μ_0 is the cosine of the solar zenith angle, μ is the cosine of the sensor zenith angle, r_s is the surface reflectance, \bar{r} is the mean aerosol reflectance (MAR), F_0 is the spectral solar irradiance for the specific channel, and L_d is the difference between the sunlit and shadow radiance. As the radiance difference increases, TOD decreases. Every term except L_d in Equation (1) is either included with the image (in a metadata file) or can be estimated. \bar{r} and r_s were estimated using the following equations:

$$\bar{r} = \frac{1}{\pi} \int_0^{2\pi} \int_0^1 \int_0^{2\pi} \int_0^1 \frac{\tilde{\omega} \mu' \mu''}{\mu' + \mu''} \left(\frac{P(\Theta)}{4\pi} \right) \left(1 - e^{-\delta \left(\frac{1}{\mu'} + \frac{1}{\mu''} \right)} \right) d\mu' d\phi' d\mu'' d\phi'' \quad (2)$$

$$P(\Theta) = \frac{1 - g^2}{(1 + g^2 - 2g \cos \Theta)^{3/2}} \quad (3)$$

$$r_s = \frac{\pi L_{\text{unshaded}}}{\mu_0 F_0} \quad (4)$$

where $\tilde{\omega}$ is the single scatter albedo, P is the scattering phase function (represented by the Henyey-Greenstein phase function), g is the asymmetry parameter (0.65), Θ is the scattering angle, and (μ', ϕ') and (μ'', ϕ'') are the cosine of the incident and resultant zenith and azimuth angles (Henyey and Greenstein 1941). The single scatter albedo value varies regionally, but Vincent used values of 0.88 for Beijing, China and 0.95 for other locations. Additionally, Vincent set the asymmetry parameter value to 0.65 to account for both aerosol (0.6-0.7) and Rayleigh particles (~ 0).

\bar{r} approximates the diffuse sky radiance. Although the diffuse field consists of aerosol and molecular affects, the molecular affects were ignored when establishing the asymmetry parameter in Equation (3) because aerosol affects dominate at all but the lowest optical depths. Had the asymmetry parameter included the molecular affects, its value would decrease. Vincent concluded this would cause the scattering phase function

and MAR to increase, thereby lowering the AOD and increasing the low bias of the shadow method. Therefore, molecular affects were only accounted for during the final partitioning of the total optical depth.

To estimate AOD, the contribution from Rayleigh scattering, or molecular Rayleigh optical depth (δ_R), must be calculated and subtracted from the TOD. The effect of molecular absorption is considered negligible since most satellite sensor wavelength bands operate in atmospheric transmission windows. The molecules responsible for Rayleigh scattering are standard atmospheric constituents and may be calculated globally for a given wavelength using equations defined by Russell et al. (1993):

$$\delta_R(\lambda) = (0.00864 + 6.5 \times 10^{-6} H) \lambda^{-b(\lambda)} (p / p_0) \quad (5)$$

$$b(\lambda) = 3.916 + 0.074\lambda + 0.050 / \lambda \quad (6)$$

where H is the height above sea level of the radiometer in kilometers, p is the atmospheric pressure at H in hPa, and p_0 is the sea-level reference pressure (1013.25 hPa). The depolarization factor (0.00864) was chosen based on the best fit data (Frolich and Shaw 1980, Young 1980). Using Equations (5) and (6), δ_R was approximated using the center effective wavelength of the satellite channel.

2. Sensitivities

Vincent's sensitivity analysis of key terms in Equation (1) demonstrated the shadow method is most sensitive to the radiance difference between sunlit and shadow regions and surface reflectance and much less sensitive to $\bar{\tau}$, solar zenith angle, and sensor zenith angle. Additionally, Vincent detailed the expected impact on the shadow method when cumuliform, stratiform, or cirrus clouds were present. In the case of cumuliform or stratiform clouds, images with cloud coverage of more than 20% were avoided. Thin cirrus was more difficult to detect using visible channels and resulted in retrieved radiances at the sensor being higher, causing an overall high bias to the calculated AOD.

3. Limitations and Target Selection Criteria

Vincent also found several limitations to the shadow technique. First, the minimum allowed radiance difference was $10 \text{ W m}^{-2} \text{ sr}^{-1} \text{ nm}^{-1}$ (RU) and the minimum allowed surface reflectance was 0.15. These thresholds were set because of the high sensitivity to changes in radiance difference and surface reflectance below those values. Such sensitivity leads to large errors in AOD calculations with small errors in radiance difference or surface reflectance. The range of calculable AOD was set from 0.1 to 2.0. The minimum value was established to avoid negative AOD after subtracting δ_R (Rivenbark 2009). The maximum was determined by calculating TOD using the combination of allowable values that gave the maximum result. Furthermore, when optical depth is above 2.0 the surface is obscured and shadows are indistinguishable.

The method also required careful target selection in urban environments and only blue and NIR channels provided reliable results over grass backgrounds. This resulted in several recommended target selection criteria. These criteria included using large shadows over a homogeneous surface with a minimum shadow size of 4 pixels wide and 4 pixels deep (from about 1 to 32 square meters, depending on satellite resolution), using shadows that are at least 1 km away from other structures, and avoiding highly reflective shadowing structures and the subsequent adjacency effects. Vincent suggested two approaches to automating the technique, dynamic and fixed. The dynamic approach relied on isolating shadows of opportunity while the fixed approach required the preidentification of buildings meeting specified criteria for analysis.

4. Other Observations

Regardless of channel or background, the shadow technique was a manually intensive procedure with more time being spent identifying good shadows than performing the actual calculation. Process streamlining performed by Rivenbark (2009) and Dombrock (2007) took steps to improve the calculation time while exploring aspects of shadows that contributed to error in optical depth. In each study, errors in the code written in Interactive Data Language (IDL) impacted their findings. For example, when calculating the scattering phase function as part of the $\bar{\tau}$ calculation in Equation (3), a

syntax error in code raised the denominator to the power of 1 instead of 1.5. The overall impact of this mistake is difficult to determine mathematically, since the error can cause either an increase or a decrease in the value of the scattering phase function, depending on the scattering angle. Also, additional iterations in the azimuth angle loop nests in Equation (2) contributed to the low bias by causing higher values of $\bar{\tau}$ and lower values of optical depth.

C. SHADOW DETECTION IN SATELLITE IMAGERY

The key step in developing a fully automated approach to the shadow method is finding suitable shadows within the image. One satellite-based method of finding shadows uses color space indices (Sarabandi et al. 2004, Gevers and Smeulders 1999). The color space indices are defined as follows:

$$\begin{aligned} C_1 &= \arctan\left(\frac{R}{\max(G, B)}\right) \\ C_2 &= \arctan\left(\frac{G}{\max(R, B)}\right) \\ C_3 &= \arctan\left(\frac{B}{\max(R, G)}\right) \end{aligned} \tag{7}$$

where R, G, and B represent the radiance from the red, green and blue color bands, respectively. Coupling the output from these indices with a 3x3 texture filter clearly outlines the boundary between a shadow and sunlit region. Sarabandi et al. (2004) determined that C_3 worked best for locating shadows. Due to more Rayleigh scattering of blue light than red or green light, C_3 is larger in shadow regions than sunlit regions.

Although capable of identifying shadows, this satellite-based approach is poorly suited for automating the shadow method for two reasons. First, C_3 may be less effective in regions with large aerosol concentrations since the amount of scattered red and green light will increase. Second, this technique lacks necessary information to select sunlit pixels with the same surface reflectance as shadow pixels, particularly when using panchromatic channels, where surface reflectance estimation techniques are not available. Similar problems would likely arise with other satellite-based approaches. The next section describes the FASTEC procedures for identifying usable shadows and calculating AOD.

III. METHODOLOGY

An automated approach, based on trigonometry, is created using the shadow technique and overcoming the shortfalls of satellite-based shadow identification techniques mentioned in Chapter II, Section C. Knowing pixel elevations and the azimuth and elevation of the sun and satellite, the process for identifying shadow and sunlit pixels is relatively straightforward. If the line-of-sight between the sun and a pixel (called the target pixel) is blocked by a higher elevation pixel, a target pixel is in shadow. If not, a target pixel is sunlit (see Figure 4). Similarly, the new approach ensures the satellite does not collect radiance off an obstruction, instead of the target by ensuring the line-of-sight between the satellite and the target pixel is not blocked.

A. TARGET SELECTION CRITERIA TESTING

Past research identified several target selection criteria for identifying good shadow candidates for the shadow method (Vincent 2006, Dombrock 2007, Rivenbark 2009). Criteria include avoiding partial shadow pixels along the shadow edge and avoiding pixels where surrounding objects limit diffuse sky radiance. Detailed descriptions of how the automated approach addresses these concerns are described in Chapter III, Section C. The hypotheses listed below describe key target selection criteria.

Before these criteria were tested, variables used to discriminate between shadow generators were tested to eliminate tree shadows from the sample. Tree shadows may allow some sunlight to penetrate through the leaf canopy into the shadow, increasing the shadow radiance, invalidating the theory behind the shadow technique (see Figure 2). The first of these variables sets the minimum height of the shadow generator and the second sets the minimum number of pixels required for AOD calculation. To determine the combination of these variables that limits the sample to buildings, different values of the minimum shadow generator height were applied to the GSFC tile and the output examined to find the value that leaves only building shadows. Furthermore, plots of AOD for the entire DSM were created to show how it varies as tree shadows are introduced to the sample.

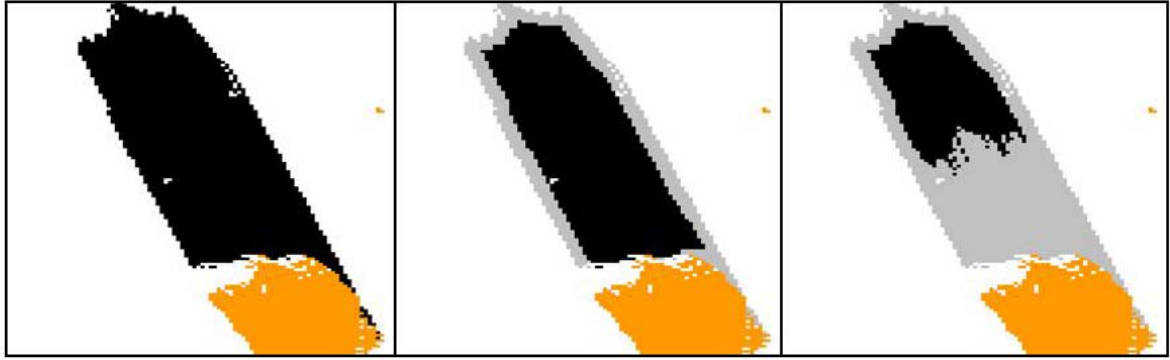


Figure 3. Example of pixel rejections from FASTEC. Orange represents the building, black is the shadow, and gray is rejected shadow. Panel 1 is the full shadow, 2 is after edge rejection, and 3 is after building proximity rejection.

1. Hypothesis I: It Is Important to Avoid Partial Shadow Pixels Along the Shadow Edge

Subjective examination of satellite imagery shows that radiance values transition across several pixels along the shadow edge. In the transition region, shadow radiance is slightly higher and sunlit radiance is slightly lower than pixels that are fully in shadow or sunlit. Including these pixels in the optical depth calculation, lowers the radiance difference and increases AOD. The edge pixel rejection variable enables the automated technique to eliminate partial shadow pixels along the shadow edge (see Figure 3). To test this hypothesis, plots of radiance based on distance from shadow edge were reviewed to determine the extent of the influence of the shadow edge on the shadow region. Additionally, the edge pixel rejection threshold was varied and the resulting AOD values compared for individual shadows and an entire DSM file. Chapter III, Section B.5.c. describes the algorithm FASTEC employs to eliminate partial shadow edge pixels.

2. Hypothesis II: It Is Important to Choose Shadow Pixels Far from the Shadow Generator to Calculate Optical Depth

Based on the past research, it is suggested the shadow region should only include pixels far from the shadow generator. In theory, reflection off surrounding objects may increase pixel radiance while blocking by surrounding objects may decrease pixel radiance. Regardless of which modification dominates, the total signal is no longer

composed of the basic components listed in Figure 2. By rejecting a percentage of the shadow pixels near the shadow generator based on the size of the overall shadow (see Figure 3) this adjacency affect is reduced. To test this hypothesis, the correlation between the pixel radiance and distance from the shadow generator was calculated for several shadows. Also, the building percentage rejection threshold was varied on individual shadows and on an entire DSM file to examine the impact on AOD. Chapter III, Section B.5.a. describes the algorithm FASTEC employs to eliminate pixels too close to the shadow generator.

3. Hypothesis III: Sky Dome Blockage Is Important When Choosing Valid Shadow and Sunlit Pixels for Calculating Optical Depth

Based on the same reasons as described for Hypothesis II, selecting pixels based on sky dome blockage may be important to the shadow technique. In order to determine the influence of sky dome blockage on the radiance of a pixel, the correlation between them was calculated for several shadows. Additionally, AOD was calculated for different maximum sky dome blockage thresholds for individual shadows and an entire DSM file. Chapter III, Section B.5.b. describes the algorithm FASTEC employs to eliminate pixels based on sky dome blockage.

4. Hypothesis IV: Eliminating the Extreme Radiance Values from the Sample Improves AOD Calculations

Radiance variation exists in the shadow and sunlit regions due to variations in surface reflectance and position differences between the satellite and DSM files. Surface reflectance variations may be caused by different surfaces or different objects such as trees, sidewalks, or cars. Position differences between the satellite and DSM files are partially corrected by the offset correction algorithm, but some error in position, rotation, or distortion may still exist. Therefore, FASTEC eliminates percentages of the extreme radiance values within shadow and sunlit regions to try and ensure the sampled regions are representative of the true shadow/sunlit radiances. Assuming FASTEC correctly identifies the shadow, the bulk of the pixels within the samples are representative of the true shadow/sunlit radiances. Sorted values of pixel radiance were plotted to demonstrate

this problem. Also, thresholds for eliminating extreme values of radiance from both the shadow and sunlit region were varied with resulting AOD values plotted for both individual shadows and across an entire DSM. Chapter III, Section B.5.d. describes the method used to eliminate extreme radiance pixels.

5. Hypothesis V: It Is Possible to Get an Idea of Uncertainty When Calculating AOD on Entire Scenes.

After setting target selection criteria based on the tests described by Hypotheses I-IV, calculations on an entire scene will provide a number of shadow/sunlit pairs and computed AOD values. The range of AOD values in the scene will give an idea of the uncertainty of the automated technique. To test, AOD values were calculated for all available imagery using entire DSM files. In cases where ground truth data is also available, AOD values for each shadow were plotted against ground truth and bias was calculated. The data is analyzed by region (for each DSM file) as well as across all regions (all DSM files). In the case of multispectral imagery, plots of AOD between channels were examined. Since the overlap between most of the available imagery and the DSM files contains several qualified shadow generators, a range of AOD values was available for most test cases.

6. Hypothesis VI: The DSM Can Have Significantly Lower Resolution Than the Satellite Data and Still Work Effectively

The computational expense of the automated algorithm is most influenced by the size of the DSM file, limiting the size of the region over which the automated method can be run operationally. Using lower resolution imagery allows calculations over a larger area without increasing computation time. For example, increasing the horizontal resolution of the DSM file from one meter to two meters, quadruples the areal coverage of the DSM with the same computational cost. As long as the resolution is sufficient to identify shadow regions with several pixels, it is believed the resulting AOD values will be comparable to the full resolution DSM. To test this hypothesis, results with varying horizontal resolution DSM files were compared to the full resolution results.

B. TRIGONOMETRIC SHADOW DETECTION METHOD

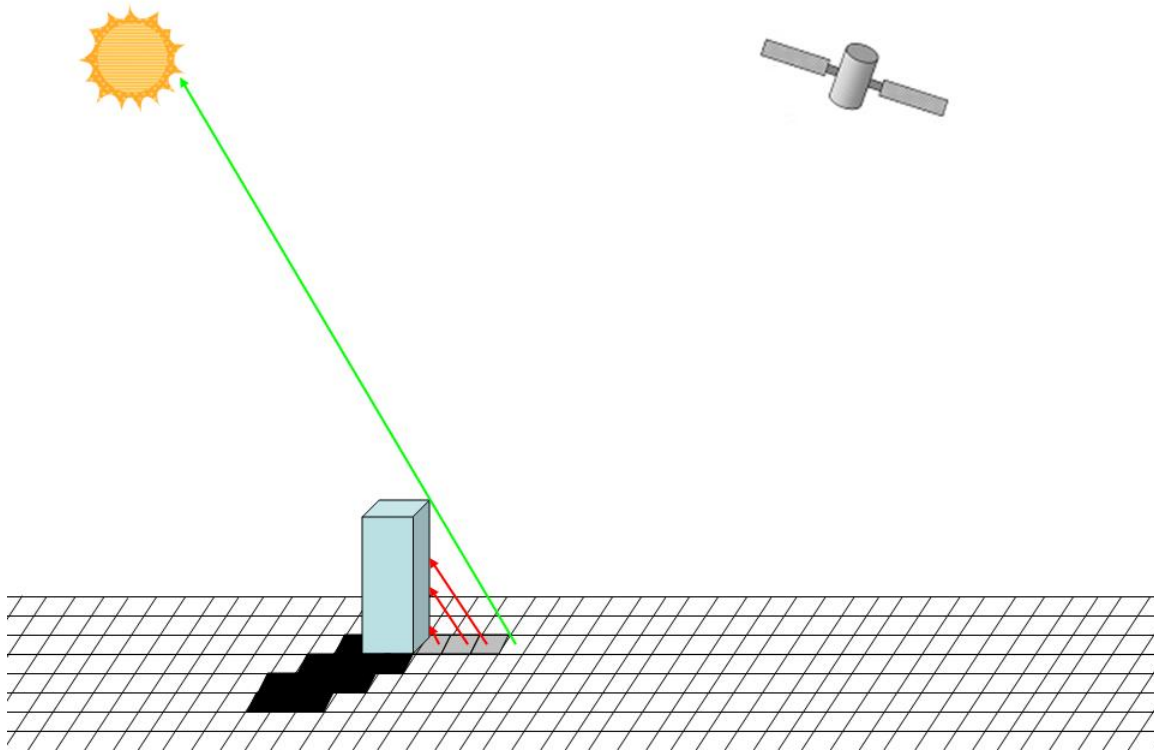


Figure 4. Trigonometric approach employed by FASTEC to find shadow pixels based on elevation. Red arrows indicate shadow pixels whose path to the sun is blocked by a higher elevation pixel. The green arrow indicates an unblocked sunlit pixel. Black pixels are obstructed from view of the satellite by the building.

A high-resolution surface elevation map, known as a Digital Surface Model (DSM), provides the critical data for FASTEC. Using this data instead of satellite data, ensures that the automated approach works in the presence of obscurations such as clouds and aerosols. To execute, FASTEC requires overlapping DSM and satellite files as inputs. Output includes a list of shadows with total optical depth (TOD) and AOD values for each qualifying shadow in the DSM file and general details of shadow/sunlit selection criteria. Figure 5 depicts a top-level flowchart of the automation program. Subroutines for each block in this flowchart are described in detail in the rest of this section.

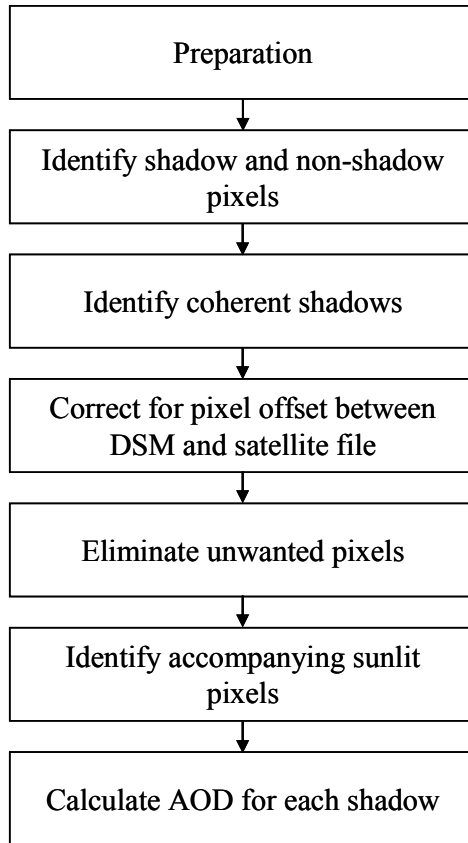


Figure 5. Top-level flowchart of FASTEC.

1. Preparation

The preparation stage is made up of two steps with step one being performed by the user prior to running the program and step two being performed by the automation program during execution. Before the automated method can begin, the DSM and satellite files are converted into flat file format, composed of a header file and a data file. This makes it easy to retrieve key header information. The details of this step as well as a description of the input files are detailed in Chapter III, Section C.1 and 2.

The automated portion of the preparation stage begins by reading in a host of variables from a configuration file. The configuration file allows the user to quickly change variable values and eliminates the need to recompile the program whenever these variable values are changed. For this program, the configuration file variables include the input and output file names, shadow and sunlit modification variables, offset correction

and dome blockage criteria, and AOD calculation variables (see Appendix A for a description of each variable). Next, key information from the DSM and satellite flat file headers are read into the program including: the number of rows and columns of data, the number of channels of data, the data storage format, the latitude and longitude of the top left pixel, and pixel size in both the north-south and west-east directions. Additionally, necessary information from the image metadata file is read including: the absolute calibration factor and effective bandwidth of each channel, the date and time of the image, the satellite name, and the sun and satellite azimuths and elevations. Equation (8) converts Digital Numbers (DN) into spectral radiance using absolute calibration factor and effective bandwidth:

$$L_{\lambda}(i) = DN_i \frac{\text{absCalFact}_i}{\text{effBandwidth}_i} \quad (8)$$

where $L_{\lambda}(i)$ is the spectral radiance, i is the channel number, and absCalFact_i and effBandwidth_i are the absolute calibration factor and effective bandwidth, respectively. DN is essentially the relative spectral radiance and is based on the amount of energy detected by the sensor. Additionally, the values for δ_R and spectral solar irradiance are chosen from Table 1 during this step. δ_R values were calculated by taking a response-weighted average using Equations (5), (6), and (9):

$$\delta_{RT} = \frac{\int \delta_R(\lambda) \phi(\lambda) d\lambda}{\int \phi(\lambda) d\lambda} \approx \sum_{\lambda} \delta_R(\lambda) \frac{\phi(\lambda)}{\sum_{\lambda} \phi(\lambda)} \quad (9)$$

where δ_{RT} is the total MROD across the channel and $\phi(\lambda)$ is the specific spectral response for that wavelength and satellite channel. An example of the spectral response curve for the QuickBird satellite is provided in Figure 6. The summation in Equation (9) was performed using a 50 nm wavelength interval across the channel. Spectral solar irradiance was calculated using the same approach where the wavelength-specific spectral solar irradiances were taken from Wehrli (1985).

Sat	Band	Wavelength Range (nm)	Center Effective Wavelength (nm)	Molecular Rayleigh Optical Depth	Spectral Solar Irradiance ($\text{W m}^{-2} \text{nm}^{-1}$)
Quickbird	Blue	450-520	486	0.172	1940
	Green	520-600	547	0.105	1851
	Red	630-690	652	0.051	1593
	Near-Infrared	760-900	804	0.026	1127
	Panchromatic	445-900	689	0.061	1558
Ikonos	Blue	445-516	497	0.165	1916
	Green	506-595	560	0.097	1835
	Red	632-698	666	0.047	1539
	Near-Infrared	757-853	792	0.027	1170
	Panchromatic	526-929	727	0.048	1468
WV1	Panchromatic	400-900	667	0.070	1587

Table 1. List of Molecular Rayleigh Optical Depth and Spectral irradiance constants by satellite and channel.

The last steps in the preparation stage expand the row and column sub-region (if a sub-region was defined) and reads in the entire DSM file. Expanding the sub-region enables FASTEC to identify usable sunlit pixels outside the user-defined area to pair with shadows inside the sub-region. The entire DSM file data is stored in an array for the step described in the next section.

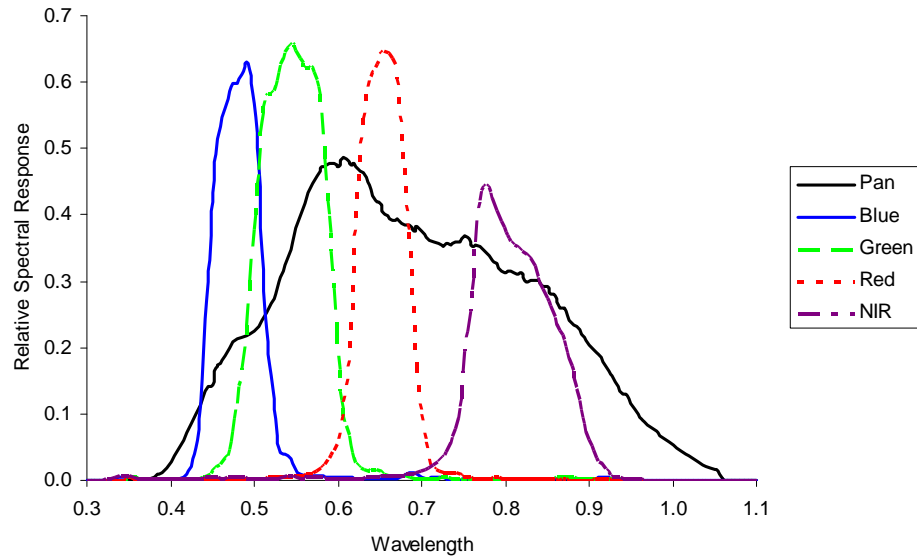


Figure 6. Relative spectral response for the QuickBird satellite derived from data provided by DigitalGlobe.

2. Identify Shadow and Sunlit Pixels

This step identifies shadow and sunlit pixels and determines which pixels are blocked from the view of the satellite. The results are stored in an array and used by subsequent steps in the program. The results array contains one of three possible values: distance from the shadow generator for in-shadow pixels, zero for sunlit pixels, or *invalid* for pixels blocked from view by the satellite.

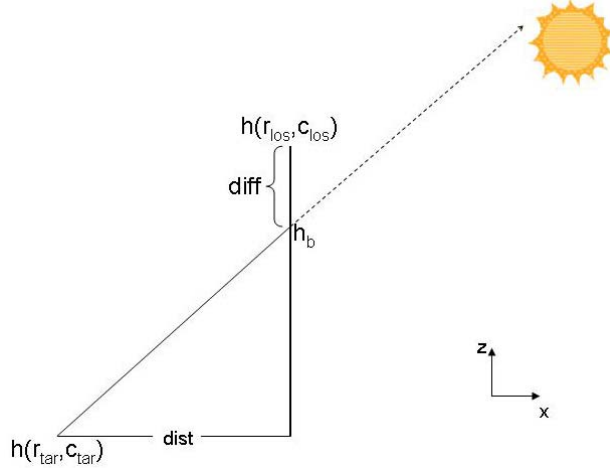


Figure 7. Calculation of in-shadow pixel $h(r_{tar}, c_{tar})$. The height of the beam (h_b) between the target pixel and the sun is less than the height of pixel $h(r_{los}, c_{los})$. Diff is the difference between $h(r_{los}, c_{los})$ and h_b .

Pixels are considered shadow whenever the line-of-sight between the target pixel and the sun is blocked by a higher elevation pixel (see Figure 7). The elevation of the line-of-sight between the sun and target pixel is computed using the below equations:

$$\text{dist} = \sqrt{\left[dy(r_{los} - r_{tar})\right]^2 + \left[dx(c_{los} - c_{tar})\right]^2} \quad (10)$$

$$h_b = h(r_{tar}, c_{tar}) + \text{dist} \times \tan(\text{elev}_{sun}) \quad (11)$$

where h_b is the elevation at pixel (r_{los}, c_{los}) of the line-of-sight between the sun and the target pixel (r_{tar}, c_{tar}) , dx (dy) is the pixel size in meters in the east/west (north/south) direction, $h(r_{tar}, c_{tar})$ is the height of the target pixel, and elev_{sun} is the elevation angle of the sun in radians. This calculation is repeated for every pixel on the azimuth between the target pixel and the sun until h_b exceeds the elevation of the tallest pixel in the DSM.

Shadow pixels store the distance from the target to the shadow generator in the result array. Some shadow pixels, such as those having two tall buildings between them and the sun, may have multiple shadow generators. In that situation, the result array value is determined by the pixel with the largest difference (diff) between the shadow generator height $h(r_{los}, c_{los})$ and h_b (see Figure 7). This ensures the stored value coincides with the shadow generator that places the target pixel deepest in shadow. This approach will cause an occasional good shadow pixel to be marked *invalid* when eliminating unwanted pixels (see Chapter III, Section B.5.a). Any pixel whose line-of-sight is unblocked is considered sunlit and is labeled with a zero in the result array.

After identifying each pixel in the DSM as shadow or sunlit, the view between the satellite and the ground is considered. This ensures that pixels representing objects obstructing the surface when viewed from the satellite are identified and labeled *invalid* in the result array. The procedure for performing this test uses a similar approach as described above with the satellite location substituted for that of the sun. Aside from that, the only difference is that any obstructed surface region is immediately marked *invalid* in the result array. When this step completes, the result array contains pixels identified by distance from shadow generator for shadow pixels, zero for sunlit pixels, or *invalid* for pixels obstructed from view of the satellite.

3. Identify Coherent Shadows

Once shadow and sunlit pixels are identified, FASTEC groups adjacent shadow pixels as one shadow and assigns that shadow a number, sequentially from one, for identification. The procedure begins by examining the result array from the previous section (any pixel whose value is greater than zero). Once a shadow pixel is found a recursive subroutine is called to find neighboring shadow pixels. Any neighboring shadow pixel that is found is identified as belonging to the same shadow and the same recursive subroutine is repeated for that shadow pixel. This process is repeated until every shadow pixel has been assigned a shadow number. To improve performance in

later steps, the range of rows and columns and the pixel count for each coherent shadow are also stored. The coherent shadow array contains positive integers for shadow pixels, zero for sunlit pixels, and *invalid* for other pixels.

4. Correct for Pixel Offset Between DSM and Satellite File

The latitude and longitude of each point in the DSM and satellite file must match precisely for FASTEC to properly measure shadow and sunlit radiance and calculate AOD. Due to the poor geolocation of the satellite imagery used in this study, pixel locations within these files rarely match and correction is required. To demonstrate the impact of this problem, shadow pixels identified by the automated method were compared to those identified by hand in a satellite file (see Figure 8). In Figure 8, panel A represents the results from FASTEC, where green identifies shadow pixels and yellow identifies partial shadow pixels. Due to resolution differences between the DSM file (one meter) and the satellite file (2.4 meters), the resolution from the automated results in Panel A was matched to the satellite resolution in Panel B. This led to between four and nine DSM pixels comprising each pixel in Panel A. In cases where every DSM pixel within a satellite pixel was identified as shadow by FASTEC, the comparison identified the pixel as fully in shadow. In cases with a mixture of shadow and sunlit pixels existed, the comparison identified them as partial shadow. Panel B represents the results of a by-hand analysis of the satellite image. Panel C shows the shadow pixel overlap (162 pixels) between Panels A and B without performing offset correction. By shifting the latitude and longitude of every pixel in the DSM file equally, the overlap increased to 218 pixels, as shown in Panel D. Without offset correction, 38% of the FASTEC shadow pixels were actually sunlit, resulting in higher shadow radiance and higher values of optical depth. This case required an eight meter shift, performed by hand, to maximize the overlap. Other cases required shifts of 100 meters or more, most likely due to the imprecise orthorectification applied to the satellite files.

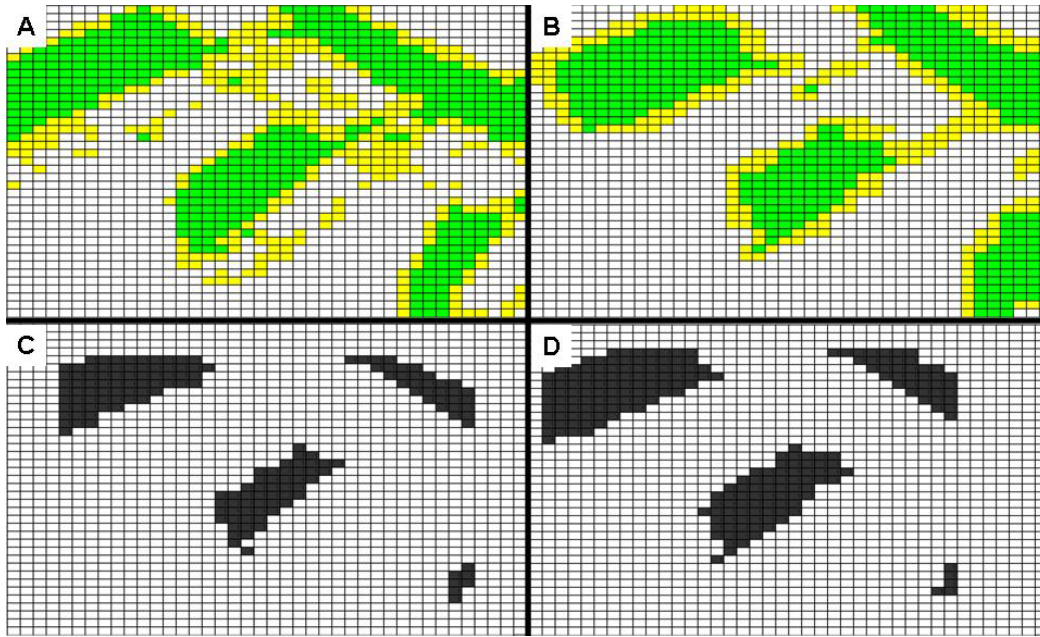


Figure 8. Four-panel plot of offset between satellite and DSM files for Goddard Space Flight Center on October 26, 2006. In Panels A and B, green is shadow and yellow is partial shadow pixels. Panel A displays the results from FASTEC and B displays the results from a by-hand analysis of the satellite file. Panels C displays overlap between A and B without offset correction (162 pixels). Panel D displays overlap with offset correction (218 pixels).

Regardless of the amount of shift required, correcting for the offset between the input files is critical to FASTEC. An automated offset correction procedure that adjusts the latitude and longitude of the upper left corner in the DSM file to find the lowest average shadow pixel radiance was developed. The range over which the average radiances are computed is set in the configuration file. Shadow pixels are identified using the coherent shadow array, with correction for edge contamination (see Chapter III, Section B.5.b.). This procedure corrects for translation error between the DSM and satellite file. It does not correct for rotation error or distortion error. To improve computation time, the correction is performed with a coarse and fine stage. During coarse correction, the coordinates of the upper left corner of the DSM are shifted by an increment in the configuration file, nominally 4 pixels in both the north/south and east/west directions. After each shift, the average coherent shadow radiance of one satellite channel is calculated for each valid target shadow. The offset that provided the lowest average radiance is the starting point for fine correction. During fine correction,

the process is repeated for every possible shift between the coarse increment and the coarse correction best fit. After the lowest average shadow radiance is found, the latitude and longitude of the DSM file is adjusted by that offset interval.

5. Eliminate Unwanted Pixels

Several procedures were developed to eliminate pixels whose radiances are not representative of the radiance in shadow or sunlit regions because of reduced diffuse radiance, combined shadow/sunlit radiance, and differing surface reflectance. Each procedure is geared toward testing target selection theories as outlined in Vincent (2006), Rivenbark (2009), and Dombrock (2007). Figure 3 displayed examples of output from FASTEC for two of these criteria. Each of the rejection methods are described in more detail in the remainder of this section. Different variables in the configuration file control execution of these procedures, thereby making them easily adjustable.

a. Pixels That Are Too Close to the Building

As portions of the sky are blocked by taller structures, the amount of diffuse sky radiance reflecting off a pixel is reduced, thereby lowering radiance values and increasing error in AOD measurements. Rivenbark (2009) and Dombrock (2007) suggested selecting shadow pixels far from the shadow generator in order to mitigate the impact of this effect. FASTEC includes two methods of eliminating pixels based on their proximity to the shadow generator; the first eliminates pixels using their physical distance from the shadow generator while the second eliminates a percentage of the pixels within the overall shadow (see Figure 9).

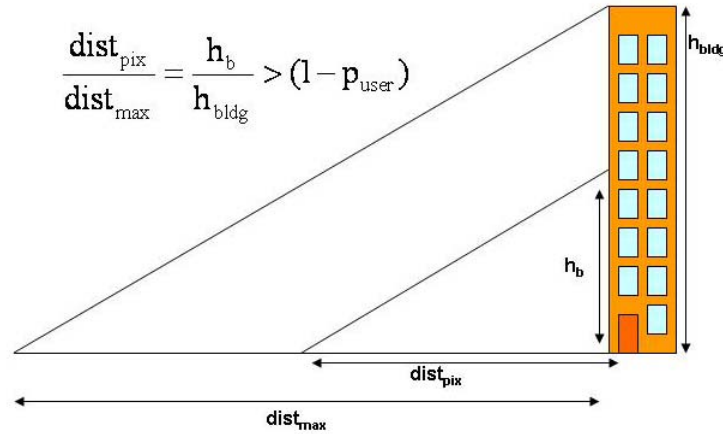


Figure 9. Identifying pixels by proximity to shadow generator. h_{bldg} is the height of the building, h_b is the height of the line-of-sight between the target pixel and sun, dist_{pix} is the distance from the shadow generator to the target pixel, dist_{max} is the farthest extent of shadow, and p_{user} is the percentage of pixels to mark *invalid*.

In the interest of computational efficiency, these calculations are actually performed when identifying shadow and sunlit pixels (see Chapter III, Section B.2) but are stored in a separate array. These adjustments are separated to prevent error in the offset correction algorithm. Additionally, it allows the output from this step to be stored in a file and examined separately during testing. Assuming the radiance is lowest near the building where diffuse sky radiance is blocked by the building, performing the offset correction after this step would choose offset values that place the shadow region too close to the building, the exact location this step is trying to avoid. This would cause the alignment between the DSM and satellite file to be incorrect, likely resulting in significantly lower sunlit radiance values as many pixels identified as sunlit in the DSM would fall over shadow in the satellite file.

When selecting pixels based on the physical distance from the shadow generator, the distance from the target pixel to the shadow generator is compared to a threshold as defined in the configuration file. If the distance is less than the threshold, the shadow pixel is marked *invalid*. To select pixels based on their proximity by percentage of the overall shadow, the ratio displayed in Figure 9 is compared against the building percentage rejection threshold in the configuration file. If the ratio is less than the

threshold, the pixel is marked *invalid*. The results from this step are integrated into the coherent shadow array immediately after offset correction is performed.

b. Pixels Whose Sky Dome Is Blocked by Adjacent Pixels

As described in the preceding section, diffuse sky radiance is blocked by any tall objects near a pixel. The test based on distance from the building addressed the problem between shadow pixels and the shadow generator. To fully address the impact of diffuse sky radiance, the automated approach must examine other surrounding objects. A procedure was developed to examine the sky dome blockage of shadow and sunlit pixels before allowing them to be used in the AOD calculation. The sky dome is considered the region of the sky that is visible to the target pixel.

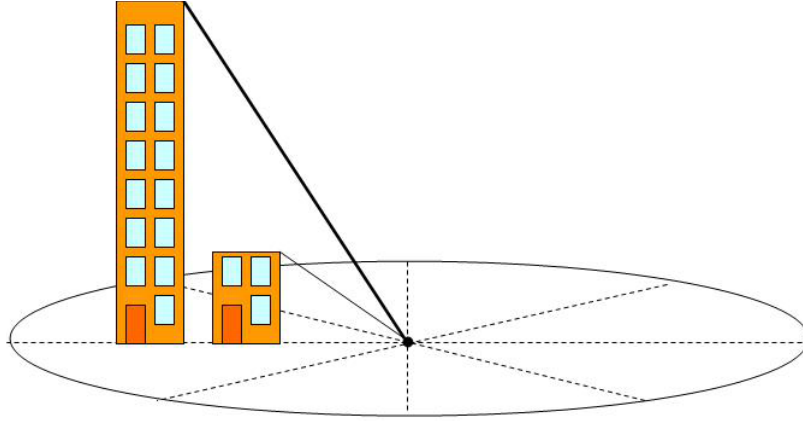


Figure 10. Celestial dome blockage. The dark line depicts the angle representing dome blockage along that azimuth.

The procedure determines the percentage of sky dome blockage by averaging the blockage along equally-spaced azimuths (see Figure 10). The angle between every pixel within the search range and the target pixel is computed along each azimuth in a circle around the target pixel. The azimuth interval, distance interval, and search range are assigned using the configuration file. The angle (θ) between the pixels is computed using the following equation:

$$\theta = \tan^{-1} \left(\frac{h(r_2, c_2) - h(r_{tar}, c_{tar})}{\sqrt{dy(r_2 - r_{tar})^2 + dx(c_2 - c_{tar})^2}} \right) \frac{180}{\pi} \quad (12)$$

where (r_2, c_2) and (r_{tar}, c_{tar}) are the along-azimuth pixel and target pixel respectively, $h(r, c)$ is the height of that point, and dx and dy are the pixel resolution in the north/south and east/west directions. The average maximum blockage angle along each azimuth is divided by 90 to get the overall blocked percentage of the sky dome. If the average blockage exceeds the threshold in the configuration file, the pixel in the coherent shadow array is labeled *invalid*. The output from this procedure is integrated into the coherent shadow array prior to offset correction. Additionally, the average blockage calculation results are stored in an “average blockage” array.

c. Pixels That Are Too Close to the Shadow Edge

Pixels along shadow edges are partially sunlit. This is apparent because the radiance values increase significantly near the edge of the shadow. Figure 11 displays the shadow pixel radiances as determined by FASTEC. In this example, pixels near the center of the shadow have spectral radiance values between 15 and 17 RU while radiances get larger as the shadow edge is neared. This pattern is reversed for sunlit pixels. Including these edge pixels raises shadow radiance and lowers sunlit radiance, causing computed AOD values to increase. In the satellite image, one would expect this contamination to affect only those pixels along the shadow edge. Due to the nearest neighbor method of retrieving radiances for each pixel and issues with offset between the images, this problem may impact more than just those pixels closest to the shadow edge. A procedure was created to eliminate contaminated edge pixels from the computation.

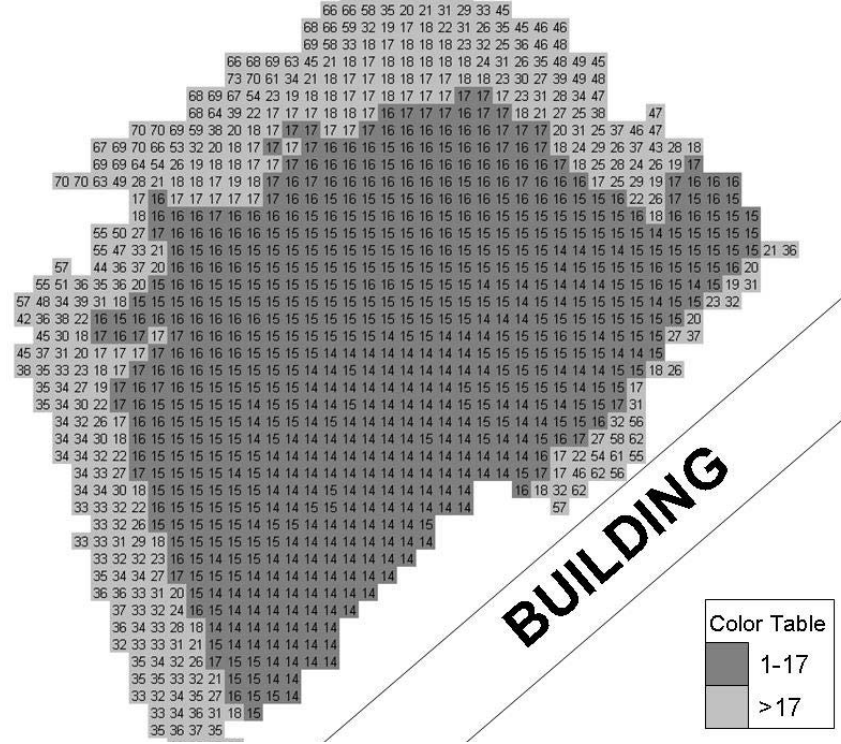


Figure 11. Example of shadow radiances from FASTEC. Spectral radiance values are units of $\text{W m}^{-2} \text{sr}^{-1} \text{nm}^{-1}$ (RU). Building location is estimated.

The procedure to eliminate shadow edge pixels examines every pixel within range (as assigned by the configuration file) of valid shadow pixels. If a sunlit (shadow) pixel is within range of the target shadow (sunlit) pixel, the target pixel is labeled *invalid*. The result from this step is stored in an “interior” array for later use. The interior array is integrated into the coherent shadow array prior to offset correction to reduce the shadows used in offset correction to those most likely to have optical depth calculations performed.

d. *Pixels with Elevation Issues or Extreme Radiances*

The shadow method requires the shadow and sunlit regions to have the same surface reflectance. Without surface reflectance maps of comparable resolution, this requirement is impossible to fully satisfy. In order to improve the likelihood this requirement is met, two final corrections are performed.

The first correction examines the elevation of every point within the shadow region. If the difference between the maximum and minimum elevation exceeds a threshold in the configuration file, the pixel whose elevation falls farthest from the mean elevation of the shadow region is labeled *invalid*. This process is repeated until the difference between the max and min elevation no longer exceeds the threshold. This procedure eliminates trees, small buildings, cars, or other tall objects that most likely have different surface reflectance within the shadow region. It does not account for different surface types, such as asphalt and grass, which change surface reflectance. A similar procedure for sunlit pixels is described in the next section.

The second correction is the only correction that is based on satellite pixel radiance. It assigns radiances to the remaining valid shadow pixels, sorts them by radiance, and then eliminates percentages of the extremes based on thresholds in the configuration file (see Figure 12). The pixels are sorted by radiance as they are read into the array and the extremes are not used to compute the average radiance of the shadow. This procedure eliminates small areas in the shadow region with different surface reflectance and counteracts some offset correction error.

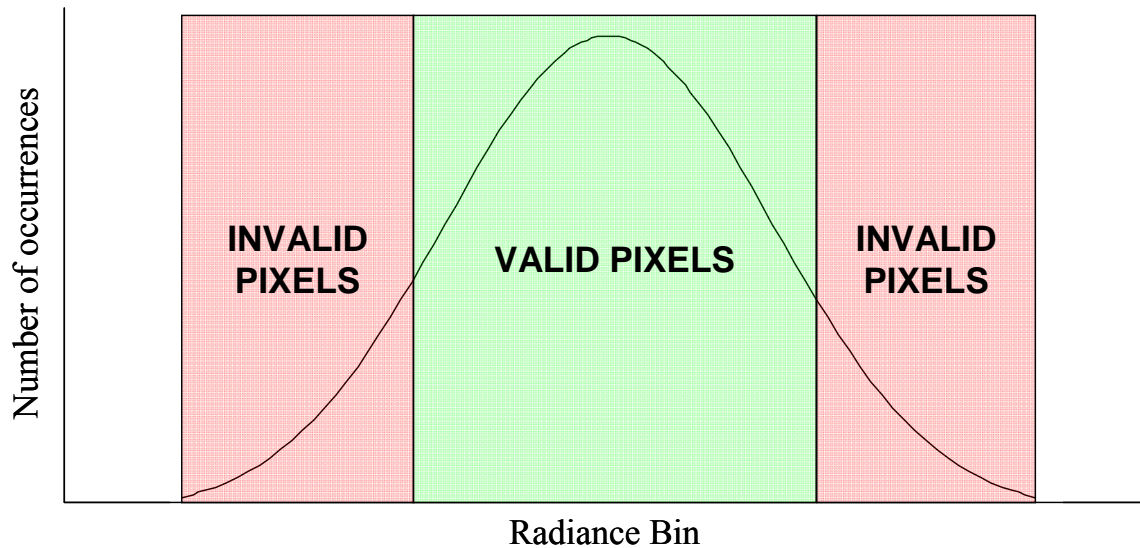


Figure 12. Histogram of radiance values with extreme radiance rejection. The actual distribution is not necessarily normal as depicted in this graphic.

6. Identify Accompanying Sunlit Pixels

For each shadow that is large enough (as defined in the configuration file) for AOD computation, sunlit radiance is required. The procedure to compute sunlit radiance begins by associating a set of candidate sunlit pixels based on their proximity to the shadow. The search region for valid sunlit pixels is limited to a 180 degree region around the shadow, perpendicular to the sun (see Figure 13). Using an azimuth and distance approach similar to the procedure described in the section for sky dome blockage, this procedure searches for candidate sunlit pixels.

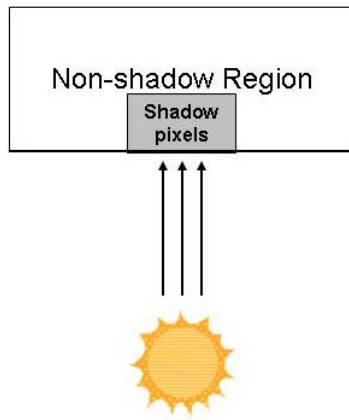


Figure 13. Region for sunlit pixel search.

After identifying the initial sunlit candidates, the procedure eliminates unwanted pixels. First, sunlit pixels are eliminated based on their sky dome blockage, using the same procedure described in Chapter III, Section B.5.b. Next, it eliminates pixels based on elevation using a similar process to the method described in the previous section. Unlike the shadow pixel elevation elimination, this process compares the elevation of each sunlit candidate to the average elevation of the shadow region. Any pixel elevation that falls outside the tolerance, as defined in the configuration file, is eliminated from the sunlit pixels dataset. Since it is possible to associate a sunlit pixel with more than one shadow, this elimination is done for each individual shadow. This approach is done to align the shadow and sunlit regions in an effort to improve confidence that they have the same surface reflectance.

The final elimination step removes the extremes of the sorted radiances using the same approach described in Chapter III, Section B.5.d. Finally, the average sunlit radiance is computed from the remaining sunlit pixels. The automated shadow detection program described above greatly increases the total number of shadow/sunlit pairs for a given time period when compared to manual calculations. The last major section of the program ties in past research to this automated shadow detection algorithm.

7. Calculate AOD for Each Shadow

The AOD calculation is performed for each shadow/sunlit pair that meet the minimum size requirement using a series of subroutines to compute Equations (1) - (4). The subroutines were optimized to improve computation speed but follow the methodology used in past research (Vincent 2006, Dombrock 2007, Rivenbark 2009) with corrections to the issues described in Chapter II, Section B.4. In instances where the shadow radiance is larger than the sunlit radiance (due to poor target selection, offset correction, or cloud cover), the calculation is not performed and dummy TOD and AOD values are passed to the output file to allow for further examination of those shadows. The output from the automated algorithm is described in detail in Chapter III, Section C.3.

C. DATA

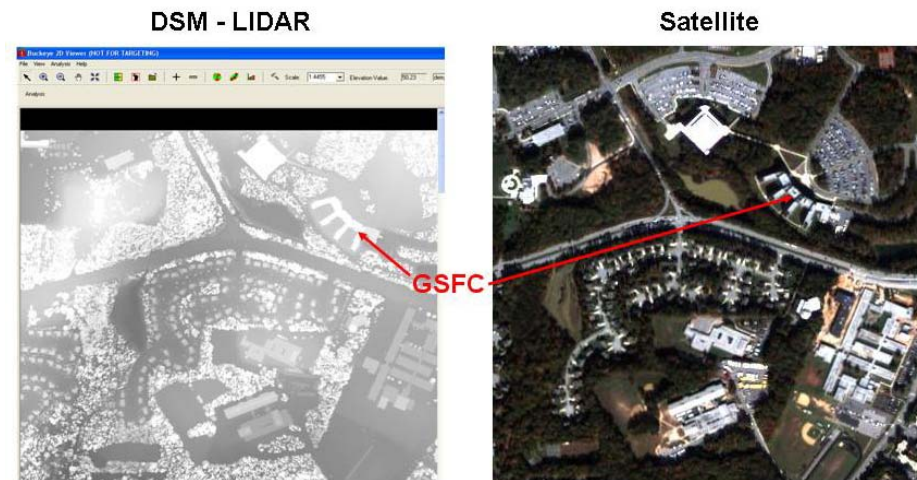


Figure 14. Examples of input data used in this research. Both images are over the Goddard Space Flight Center (GSFC) near Washington D.C. The QuickBird satellite image is from October 26, 2006.

1. Digital Surface Model (DSM)

For the purposes of this study, the term Digital Surface Model (DSM) refers to the one meter resolution elevation maps used as the basis of the automation technique. In these maps, each data point (or pixel) contains the elevation of the first solid object encountered when looking down at the surface from above. Several methods have been developed for creating a DSM. Two measures are commonly employed to describe accuracy; Circular Error of 90% (CE90) for horizontal accuracy and Linear Error of 90% (LE90) for vertical accuracy. CE90 is the minimum diameter of the horizontal circle that can be centered on all photo-identifiable Ground Control Points (GCPs) and also contain 90% of their respective twin counterparts acquired in an independent geodetic survey. LE90 is the linear vertical distance that 90% of control points and their respective twin matching counterparts acquired in an independent geodetic survey should be found from each other (GeoVAR 2009). Two techniques for creating high resolution DSM data are stereo-pairs and light detection and ranging (LIDAR).

Stereo pairs consist of two images of the same scene taken at near simultaneous times with slightly different view angles. Ground control points provide baseline location and elevation information to calibrate the image and improve its accuracy. DigitalGlobe advertises accuracy of 6.5m CE90 and 6.5m LE90 (DigitalGlobe, cited June 2010c) although Low et al. (2006) improved CE90 to 5.0m or better.

Another method of creating a DSM uses LIDAR instruments flown aboard aircraft. The U.S. Army Topographic Engineering Center (TEC) BuckEye system employs a LIDAR sensor to create one meter resolution DSM data of 0.5m CE90 and 0.3m LE90 accuracy (TEC 2009). The high resolution and accuracy of this data makes it a superior choice for the automation technique. For this study, the LIDAR data is distributed as approximately 5km x 5km tiles in GeoTiff file format. ENVI 4.5 is visualization software, capable of displaying and manipulating data in a multitude of formats. This software is used to convert these DSM files into flat files to simplify data ingest.

2. Satellite Data

High-resolution commercial satellite data from the IKONOS, QuickBird and WorldView-1 satellites were used in this study. QuickBird offers panchromatic and multispectral imagery with CE90 of 23m and horizontal resolutions of 60cm and 2.4m, respectively. WorldView-1 offers a panchromatic imagery with CE90 of 6.5m and horizontal resolution of approximately 50cm (DigitalGlobe, cited June 2010a/b). IKONOS offers multispectral and panchromatic imagery with CE90 of about 6m and horizontal resolutions of 1m and 3.28m, respectively (Dial et al. 2003, IKONOS, cited May 2010). All satellite data was ordered via the Internet using the Web-based access and retrieval portal on the National Geospatial-Intelligence Agency Web site in NITF 2.0 format. This study used basic imagery from DigitalGlobe (QuickBird, WorldView-1). This imagery is not orthorectified although a built-in process in ENVI, using rational polynomial coefficients, was used in an effort to remove some distortion. ENVI software was also used to save the imagery as flat files. Although Rivenbark (2009), found that orthorectification was not critical when implementing the shadow technique by-hand, FASTEC needs each pixel to be as accurately mapped to the earth as possible, and orthorectification was performed. Using fully orthorectified imagery may have significantly improved the alignment between files and improved the results (especially in complex urban settings).

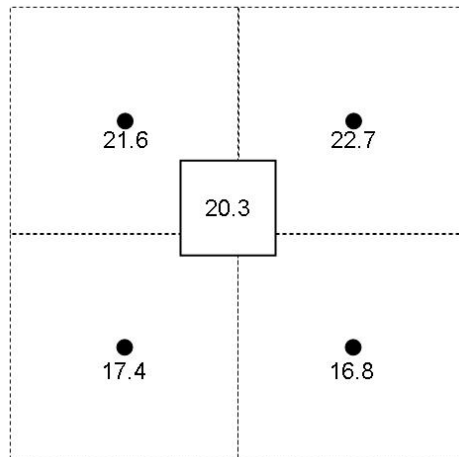


Figure 15. Nearest neighbor method. In this example, radiance is assigned to a 1 m resolution DSM pixel (solid box) using the radiances of four surrounding 2.4m satellite pixels (hatched boxes).

Due to resolution differences between the DSM and satellite file, weighted averaging was used to assign radiances to the DSM pixels (see Figure 15). To begin, the latitude ($\phi_D(r)$) and longitude ($\lambda_D(r)$) of the DSM pixel at row and column (r,c) are determined:

$$\phi_D(r) = \phi_{D_{UL}} - (r-1)d\phi_D \quad (13)$$

$$\lambda_D(c) = \lambda_{D_{UL}} + (c-1)d\lambda_D \quad (14)$$

where the coordinates of the top left corner ($\phi_{D_{UL}}, \lambda_{D_{UL}}$) and change in latitude and longitude ($d\phi_D, d\lambda_D$) of the DSM are read from the DSM flat file header. Next, the latitude and longitude are converted into the matching row and column of the satellite file (r_s, c_s) using the following equations:

$$r_s = \frac{(\phi_{S_{UL}} - \phi_D(r))}{d\phi_S} + 1 \quad (15)$$

$$c_s = \frac{(\lambda_D(c) - \lambda_{S_{UL}})}{d\lambda_S} + 1 \quad (16)$$

where the coordinates of the top left corner ($\phi_{S_{UL}}, \lambda_{S_{UL}}$) and change in latitude and longitude ($d\phi_S, d\lambda_S$) of the satellite file are read from the satellite flat file header. The satellite row and column number are real numbers, although row and column indexing uses integers. The decimal portion of these numbers is used to determine the weight of each of the four satellite pixels that surround the DSM pixel. Following Franke and Nielson (1980), the weights are assigned using inverse weighting based on that decimal portion using variations of the following equations (top left equations shown):

$$w_{TL}(r_s, c_s) = \sqrt{((r_s - \text{int}(r_s))^2 + (c_s - \text{int}(c_s))^2)} \quad (17)$$

$$wt_{TL} = \left(\frac{R - w_{TL}}{R \times w_{TL}} \right)^2 \quad (18)$$

where wt_{TL} is the weight of the top left pixel, R is a constant representing the maximum possible fractional distance between the four satellite pixels. Similar equations are used

to calculate the weights of the top right (TR), bottom left (BL), and bottom right (BR) pixels. The weighted mean of the four satellite pixels relative radiance values (DN_{TL} , DN_{TR} , DN_{BL} , DN_{BR}) is calculated using:

$$DN_D = \frac{(wt_{TL} DN_{TL} + wt_{TR} DN_{TR} + wt_{BL} DN_{BL} + wt_{BR} DN_{BR})}{wt_{TL} + wt_{TR} + wt_{BL} + wt_{BR}} \quad (19)$$

This value was converted to absolute spectral radiance (in RU) using Equation (8).

Each satellite image is shipped with a collection of files, including the satellite file and a metadata file. These files contain critical information about the location of the image, the channel calibration information, and the sun and satellite geometry. A procedure was written to read the key data from these metadata files. The IKONOS metadata files are formatted differently than the files for WorldView-1 and QuickBird. They also lacked the necessary calibration information. To correct these issues, a program was written to reformat the IKONOS metadata file into a suitable form and to provide channel-specific calibration information that was obtained from GeoEye Corporation.

3. Output Data

FASTEC generates two output files to separate general information from the AOD calculations and simplify statistical analysis. The first file, identified by a “geninfo” tag, contains general information about that particular program run. This information includes the satellite name, image date and time, the satellite resolution, number of channels, the sun and satellite azimuth and elevation, and the absolute calibration factor, effective bandwidth, solar irradiance and δ_R for each satellite channel. The “geninfo” file also includes the name and resolution of the DSM file, the range of the DSM over which the program was run, key shadow/sunlit adjustment variables, the number of shadows identified, the DSM offset correction, the number of shadows where AOD calculations were performed, and a line stating “Program ended successfully” if the program completed without errors.

The second output file, identified with “_AOD” contains the AOD calculation data for each shadow where a calculation was performed. This information includes a shadow identification number, a shadow pixel row and column number for the DSM and satellite file, the latitude and longitude of that pixel, and pixel counts for the shadow and sunlit regions. It also includes the channel number, average shadow and sunlit radiances, and the computed TOD and AOD value for each satellite channel.

If a sub-region is less than or equal to 100 by 100 pixels, the user may create additional output files by setting a variable in the configuration file. These additional text files store critical array data used in the automated program. They are identified by “DSM” and a number as described in Table 2. If sky dome blockage is not tested, file number 7 contains zeroes. File numbers 8-11 are updated if the satellite file contains those channels. For example, if the satellite file contains one channel, only file 8 would be updated while a four channel file would update files 8-11. If additional satellite channels were available (not applicable to this study), additional files (numbered beyond 12) would be generated to store the radiance of those channels.

File Number	Contents of file
1	Raw DSM elevation data
2	Building height
3	Distance from shadow generator with satellite geometry correction
4	Same as 3 with pixels that are too close shadow generator invalid
5	Same as 3 with shadow/non-shadow edge pixels invalid
6	Coherent shadow numbers incorporating invalid pixels files 4 and 5
7	Dome block % for each valid shadow/non-shadow pixel
8-11	Absolute spectral radiance for each channel and pixel

Table 2. List of contents of DSM array output files.

4. Validation Data

Aerosol Robotic Network (AERONET) data served as ground truth in this research. AERONET is a worldwide collection of robotic sun photometers that measure AOD and are accurate to within 0.02 (Holben et al. 1998). Three levels of AERONET data are accessible on-line via the Goddard Space Flight Center Web site. Level 1.0 is

unscreened data, level 1.5 is cloud-screened data, and level 2.0 is quality assured and cloud-screened. Except where otherwise noted, level 2.0 data was used for validation.

To correct for wavelength differences between AERONET and satellite sensors, coefficients for the third order polynomial best-fit curves approximating the spectral distribution were determined using Microsoft Excel. The coefficients were determined using calculations based on time-averaged AOD values for each wavelength. Although Excel has a built-in function for generating polynomial best fit curves, an error in the Excel program (determined by comparing the built-in plot of the curve with a manual plot of the curve using the Excel-identified coefficients) produces the wrong coefficients for polynomial curves. Therefore, the coefficients were determined using the Excel LINEST function (Eng-tips, cited May 2010). These curves, along with the channel-specific spectral response curves for each satellite, were used to calculate sensor-specific ground truth AOD using Equation (9). IKONOS spectral response data is available on the GeoEye Web site while QuickBird and WorldView-1 spectral response curves are available from DigitalGlobe upon request. A third order polynomial best fit curve estimated AOD values to within 0.003 of truth (see Figure 16).

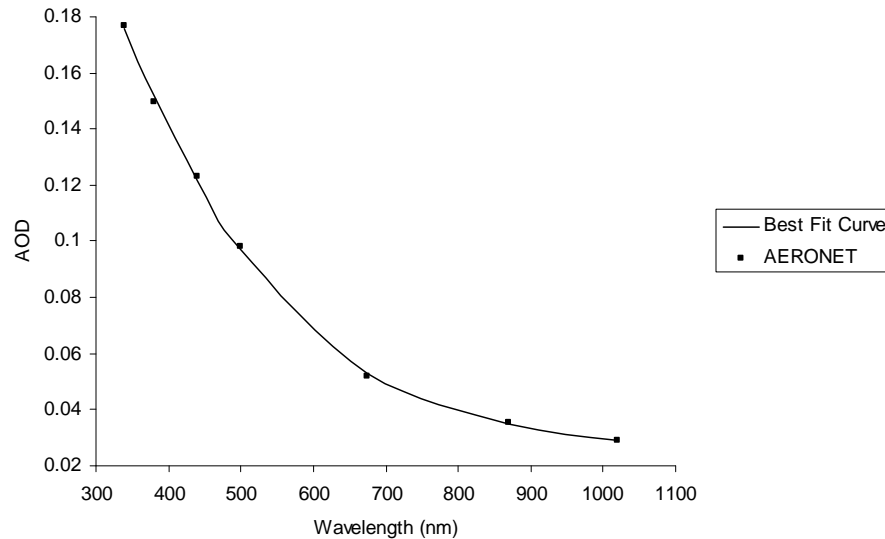


Figure 16. Third order polynomial best fit curve with raw AERONET data points.

Four test locations were chosen based on the availability of overlapping AERONET stations and Buckeye data. The four stations were Tucson (32N, 110W), MD

Science Center (39N, 76W), University of Houston (29N, 95W), and GSFC (38N, 76W). Due to the lack of high AOD cases in the available satellite images for the four test locations, an additional DSM file was created by hand near the Solar Village (24N, 46E) AERONET station (see Figure 17). The heights of the structures were estimated by using the length of a shadow and the elevation angle of the sun using the Solar Village image from April 12, 2006 at 0754Z. The automated program was designed to calculate AOD from the two satellite dish shadows. The building was included to ensure the automated method did not include those pixels as part of the sunlit region. The satellite dishes are movable objects, and orientation changes did occur between images. Orientation differences are noted when observed in testing.

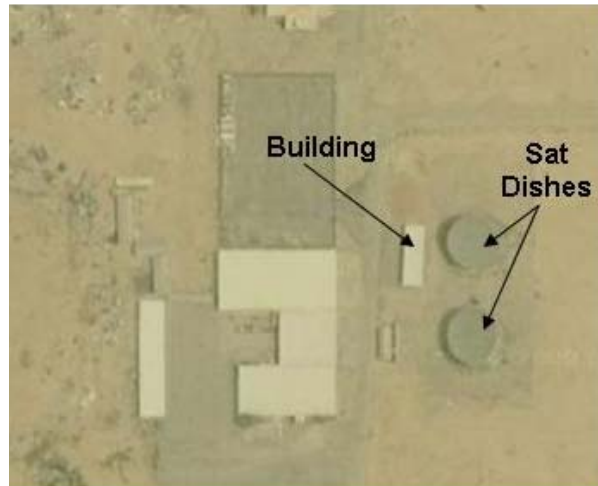


Figure 17. Satellite image of area used for hand-generated DSM (image captured from Google maps). The labeled objects were the only structures built into the DSM.

D. COMPUTATIONAL TECHNIQUES AND TESTING

FASTEC was written in FORTRAN with OpenMP for parallel processing. Using parallel processing improved the computation time from 18.2 minutes to 4.2 minutes for the entire GFSC DSM file using two Intel Xeon 3.2 GHz quad core CPUs running LINUX (see Figure 18). The improvements in calculation speed achieved through parallel programming made it possible to quickly test key variables across ranges of

possible values. Each major step in FASTEC is performed using a different subroutine to allow for easy modification of the overall process. The main program performs a few basic tasks and calls applicable subroutines as needed.

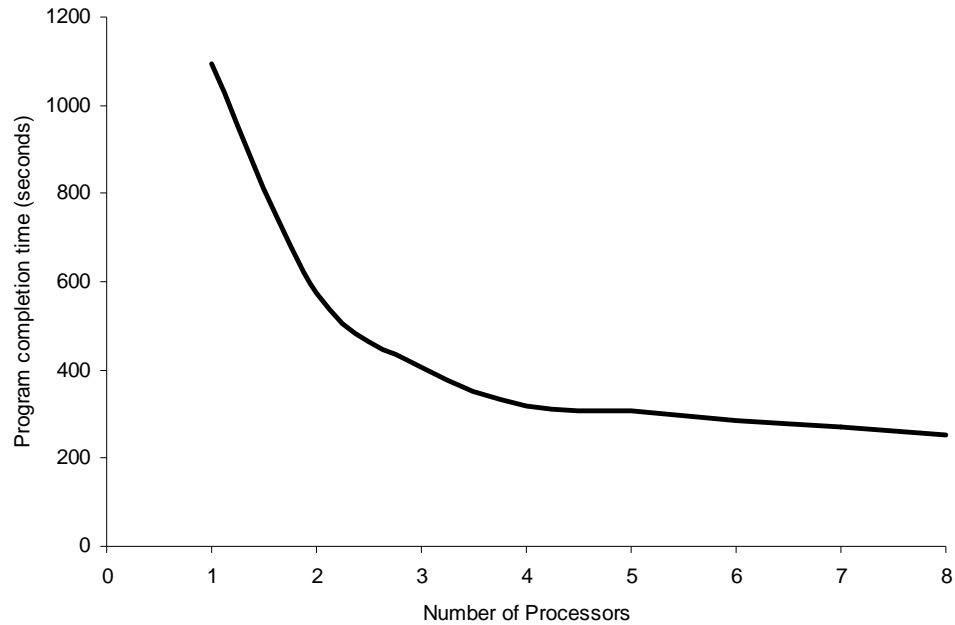


Figure 18. Plot of computation time vs. number of processors. Test case found more than 50,000 shadows in 25 km² DSM file with AOD calculations on 3015 shadows.

The design of the software allowed for pixel-level examination of the automated approach in single shadow scenes. Initial testing used this capability to study the impact of different shadow and sunlit target selection criteria and led to baseline values for AOD computations with every available image and DSM file to test the overall accuracy of FASTEC. A separate variable combination was used for the hand-generated Solar Village DSM since the shadow generators were comparatively small. For example, the satellite dishes in Solar Village were approximately 13 meters tall while nine shadow generators in GSFC were at least 35 meters tall.

IV. RESULTS

FASTEC was tested to ensure that it properly identified building shadows and calculated AOD. Initial testing examined the primary target selection criteria. The results of these tests were used to assign configuration values to perform the next tests comparing FASTEC AOD results with ground truth AERONET data. In the case of multispectral images, different channels were also compared with each other. Finally, the horizontal resolution of the DSM was reduced to examine the coarsest, usable resolution.

A. TARGET SELECTION CRITERIA TESTS

The impact of key target selection criteria was analyzed using three satellite images; a QuickBird image from October 26, 2006 at 1600Z over the GSFC DSM, a WorldView-1 image from January 16, 2009 at 1600Z over the GSFC DSM, and a QuickBird image from April 12, 2006 at 0754Z over the hand-generated Solar Village DSM. First, pixels along the shadow edge were examined to identify partial shadow pixels. After establishing an edge pixel rejection value for the GSFC building, the minimum shadow generator height was chosen to prevent AOD calculations on tree shadows. This was followed by examining the effect that distance from the shadow generator, sky dome blockage, and extreme radiance rejection had on computed values of AOD. Except where otherwise noted, the configuration file variables were assigned the values listed in Appendix B (Solar Village) and C (GSFC).

1. Rejection by Minimum Shadow Generator Height (GSFC)

The minimum shadow generator height was determined for the GSFC scene after the initial single shadow edge pixel test for the GSFC building (see Chapter IV, Section A.2.b) determined the edge pixel rejection variable should be set to 2. For this test, FASTEC was run using the October 26, 2006 GSFC image with different values for the minimum shadow generator height. Whenever the elevation difference between a shadow pixel and the shadow generator was below this threshold, the shadow pixel was marked *invalid*. Next, each shadow in the AOD output file was located in the satellite

image by hand and identified as being caused by either trees or buildings. Figure 19 displays the results of this test with minimum shadow generator height values between 25 and 40. Lower values were not analyzed by hand due to the large number of shadows identified and the fact that 88.2% of the shadows were tree shadows when the minimum shadow generator height was set to 25. With settings of 25 or above, the number of building shadows only varied by two buildings. With settings of 35 or 40, one tree shadow remained.

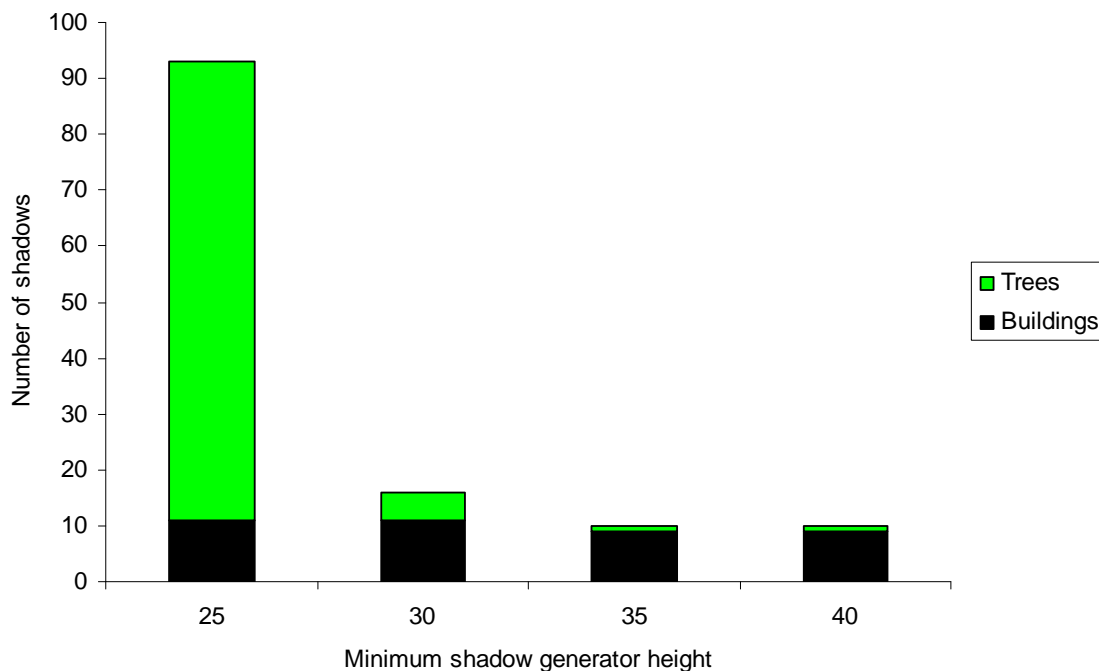


Figure 19. Number of tree/building shadows vs. minimum shadow generator height from October 26, 2006 GSFC QuickBird image.

The variation in AOD values was also examined as the minimum shadow generator height was changed (see Figure 20). In this graph, the 50th percentile of AOD was plotted for different settings of minimum shadow generator height. The error bars represent the 25th and 75th percentile of AOD values, the square marks the 50th percentile, the plus symbols mark the maximum and minimum AOD values, and the dotted line is the ground truth AERONET AOD value. In cases where the minimum shadow generator height is less than 30, the 50th percentile value and range is larger than cases where it is 30 or larger. This is due to the large number of tree shadows in the low

minimum shadow generator height test cases because tree shadows may allow some sunlight to pass through the canopy, increasing the shadow radiance and the computed AOD. The maximum value of AOD (not plotted) in test cases below 30 falls between 0.96 and 2.754. In cases where the number of building shadows exceeds the number of tree shadows, the range of AOD values between the 25th and 75th percentile shrinks from approximately 0.10 to less than 0.02. In each of these high threshold cases, the maximum is due to the one tree shadow remaining in the sample. This tree shadow can be eliminated by increasing the minimum pixel threshold to 70. The minimum pixel threshold sets the required number of pixels in the shadow and sunlit region for AOD calculations to be performed. Removing this tree shadow from the sample shrinks the AOD range between the maximum and minimum to approximately 0.02, similar to the range between the 25th and 75th percentile. Due to these findings, tests involving the entire GSFC DSM file used a minimum shadow generator height of 35 and single shadow tests on the GSFC building used a minimum shadow generator height of 15 to capture the approximately 20 meter tall GSFC building. However, minimum pixel count remained 15 and any tree shadows were eliminated from the results manually.

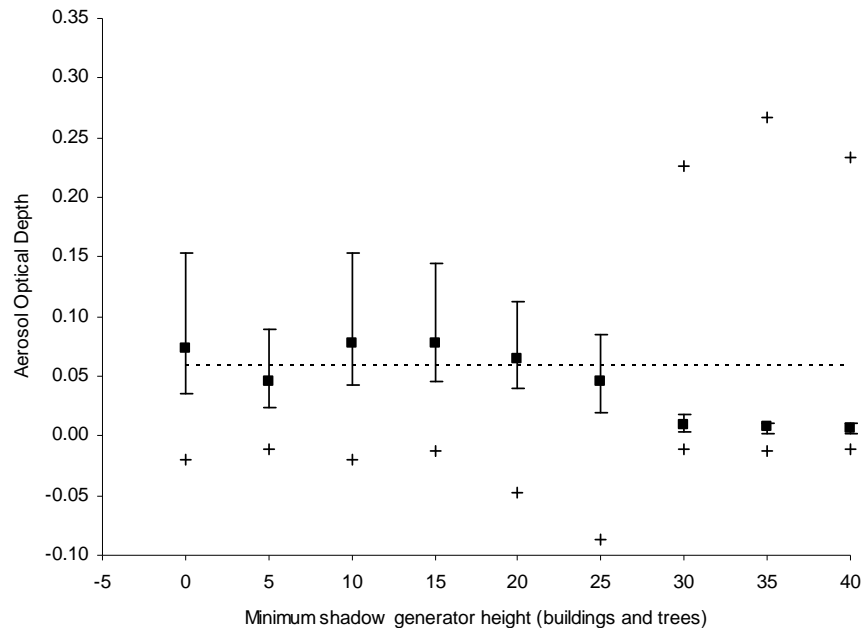


Figure 20. Minimum shadow generator height vs. 50th percentile of AOD. Computed for all shadow generators from the October 26, 2006 GSFC image. Error bars are the 25th and 75th percentile, plus symbols are the minimum and maximum AOD (maximum exceeds 0.35 in some cases), and the dotted line is ground truth.

2. Rejection of Edge Pixels

Hypothesis I states that it is important to avoid partial shadow pixels because they increase shadow radiance and decrease sunlit radiance. The edge pixel rejection variable eliminates pixel along the shadow/sunlit edge. Figure 21 shows how the shadow region for the north satellite dish (left) and the GSFC building (right) change when the edge pixel rejection variable is set to two. In this figure, yellow represents the shadow generator, dark grey represents full shadow pixels and light grey represents shadow pixels that were eliminated due to their proximity to the shadow edge. The white pixels between the shadow and shadow generators are shadow pixels that were eliminated due to excessive elevation difference or because they were blocked from view of the satellite. For example, in the GSFC scene, pixels on the northwest side of the shadow region were eliminated because they were blocked from view of the satellite while some of the pixels to the southeast of the shadow region were eliminated due to elevation difference caused by a one story annex off that wing of the building.

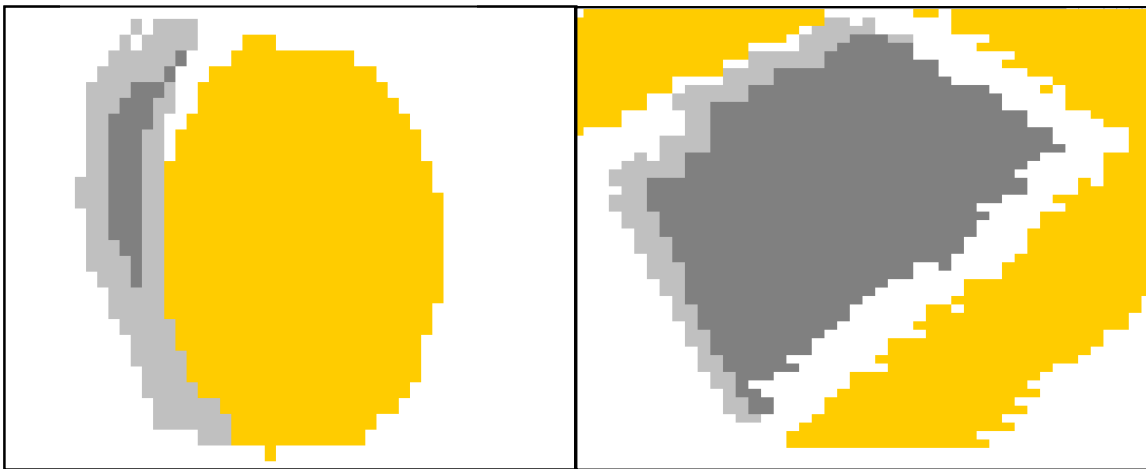


Figure 21. Example of edge rejection algorithm on Solar Village north satellite dish (for April 12, 2006 image) and GSFC building (for January 16, 2009 image). Dark grey pixels are full shadow pixels, light grey are rejected due to proximity to shadow edge, and yellow approximate the shadow generator.

a. North Satellite Dish, Solar Village

Figure 22 displays the average pixel radiance based on their proximity to the shadow edge for the north satellite dish in the April 12, 2006 Solar Village image.

The zero line marks the approximate position of the shadow edge so that every pixel falls on one side of the shadow edge or the other. The average radiances of the pixels closest to the shadow edge fall between more interior pixels. Additionally, the standard deviation of pixels that are fully in shadow is low compared to the standard deviation of the edge shadow pixels. This is partially due to the different percentages of these pixels in direct sunlight but position error between pixels in the DSM and satellite image also contributes. Regardless, including these edge pixels increases the range of radiances in both the shadow and sunlit region, which should increase the uncertainty of the computed AOD from one shadow to the next. For this case, setting the edge pixel rejection variable to one eliminates partial shadow pixels without reducing the number of usable pixels below the arbitrarily set minimum threshold of 15. Setting the interior rejection variable to two offers the lowest uncertainty of the shadow region but it decreases the number of usable shadow pixels 62%.

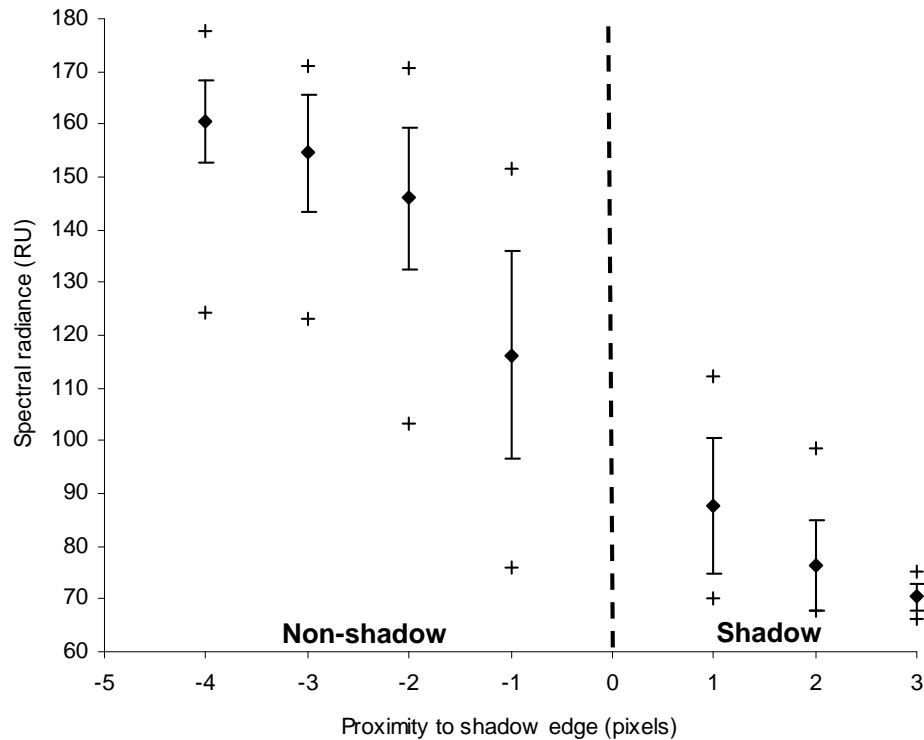


Figure 22. Average pixel radiance versus proximity to shadow edge for the north satellite dish with the April 12, 2006 Solar Village image. The x-axis is the distance from the shadow edge (in pixels) with zero marking the shadow edge, error bars are one standard deviation, and plus symbols are the max and min radiance.

When calculating optical depth for this shadow, the value decreases as the edge pixel rejection variable increases (see Table 3). This decrease is most significant as the edge pixel rejection variable changes from 0 to 1. In this example, the computed AOD value is close to ground truth when the edge pixel rejection variable is set to 0 because the partial shadow pixels decrease the radiance difference by over 11 RU when compared to the setting of 1. As before, in theory these pixels have some direct sunlight reaching them (partial shadow) and the apparent improvement in accuracy is due to misapplying the shadow method. For the remainder of tests involving the Solar Village scene, the edge pixel rejection variable was set to 1 to minimize the uncertainty of the shadow pixel radiance while capturing the most usable shadows across all available imagery. The extreme pixel rejection variables (Chapter IV.A.5.b) are designed, in part, to compensate for the small number of partial shadow pixels that remain in the sample.

Edge Pixel Rejection Setting	Shadow Pixel Count	Non-Shadow Pixel Count	Shadow Radiance	Non-shadow radiance	TOD	AOD	Error
0	168	1380	80.98	152.09	0.303	0.242	-0.001
1	98	1084	75.44	158.49	0.255	0.194	-0.049
2	37	775	70.37	160.89	0.225	0.164	-0.079

Table 3. AOD with varying edge pixel rejection setting for the north satellite dish in the April 12, 2006 Solar Village image. Ground truth AOD was 0.243.

b. Goddard Space Flight Center Building

When the automated method was applied on the GSFC building pictured in Figure 21, errors in image geo-referencing and solar azimuth and elevation cause minor alignment differences between the DSM and satellite file. While offset correction improves translation error between the images, it does not account for rotation or distortion errors. In addition, the presence of trees to the southwest of the building shadow impacts pixel radiance for more pixels in the sunlit region. All these factors make this scene more complex than Solar Village.

Similar to the Solar Village scene, the average shadow radiance does not stabilize until moving three pixels in from the shadow edge (see Figure 23). Additionally, sunlit pixel radiance is comparatively low when within two pixels of the

shadow edge. Beyond two pixels from the shadow edge the average radiance, standard deviation, and difference between the maximum and minimum radiance stabilize in the shadow region. Variation in the sunlit region is quite high due to the significant contribution of the surface reflectance dependent direct radiance signal to the total signal. Based on this examination, it appears the edge pixel rejection variable should be set to 2.

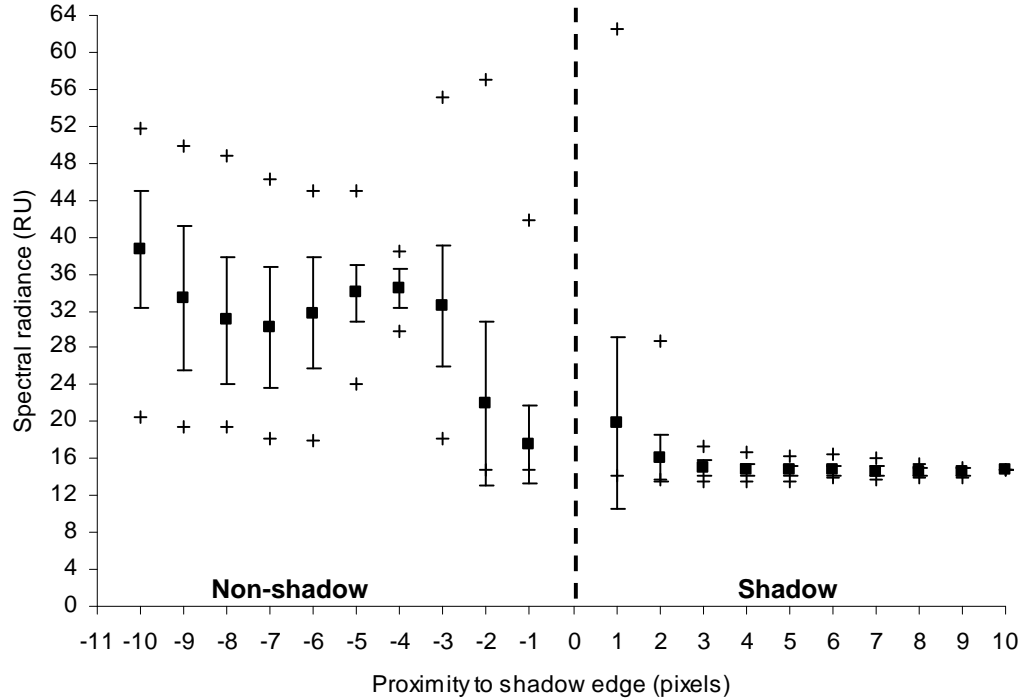


Figure 23. Average pixel radiance vs. proximity to shadow edge for the GSFC building on January 16, 2009. The x-axis is the distance from the shadow edge (in pixels) with zero marking the shadow edge, error bars are one standard deviation, and plus symbols are the max and min radiance.

When computing AOD while varying the edge pixel rejection variable for the same scene, fluctuations are quite small (see Table 4). Most notable is the change in sunlit radiance when transitioning from a setting of one to two. This comparatively large change is due the relatively small sunlit pixel count and the tree line to the southwest. The tree line shadow causes the sunlit region to shrink on several sides as the edge pixel rejection variable is increased, eliminating a large number of low radiance pixels. This supports setting the edge pixel rejection variable to two for the GSFC scene.

Edge Pixel Rejection Setting	Shadow Pixel Count	Non-Shadow Pixel Count	Shadow Radiance	Non-shadow radiance	TOD	AOD	Error
0	924	357	16.45	34.43	0.124	0.054	0.018
1	848	256	16.16	35.75	0.116	0.046	0.010
2	752	180	16.07	36.77	0.112	0.042	0.006
3	668	137	15.85	36.75	0.109	0.039	0.003
4	571	101	15.2	36.81	0.102	0.032	-0.004
5	460	69	14.8	36.83	0.098	0.028	-0.008
6	351	40	14.69	36.57	0.097	0.027	-0.009
7	250	17	14.6	34.99	0.100	0.030	-0.006

Table 4. AOD with varying edge pixel rejection setting for the GSFC building using January 16, 2009 image. Ground truth was 0.036.

Next, AOD values for the whole GSFC DSM file were computed for October 26, 2006 using only building shadows with the settings described in Chapter IV, Section A.1. The October 26, 2006 image was chosen over the January 16, 2009 image because it overlapped the entire GSFC DSM region, providing nine usable shadows instead of the four usable shadows in the January 16 image. For these computations, offset correction was enabled, the minimum shadow generator height was set to 35, the minimum pixel count was set at 15, and tree shadows were manually eliminated from the results. Figure 24 displays the results as the edge pixel rejection variable is changed from zero to nine. As the edge pixel rejection variable increased from 0, the 50th percentile value of AOD decreased. Setting the edge pixel rejection variable to two, as suggested by the previous single shadow test, selects all 9 building shadows while keeping the range of computed AOD values small. Settings beyond 5 eliminated some buildings from the sample.

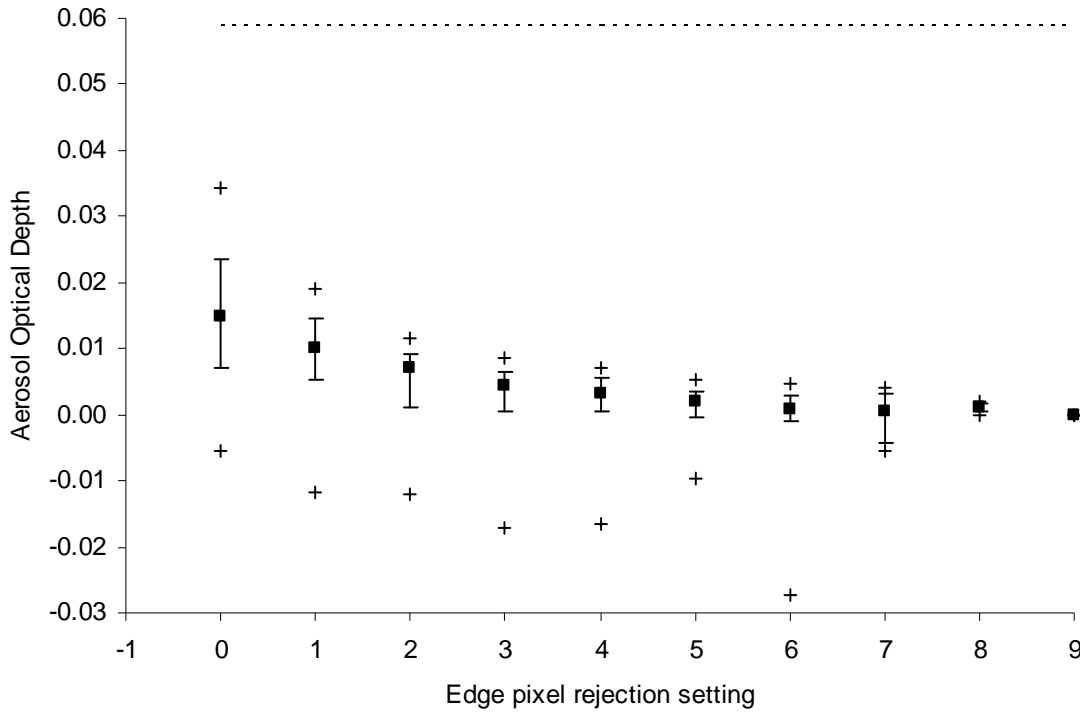


Figure 24. Aerosol optical depth vs. edge pixel rejection setting for October 26, 2006 GSFC image. The black box is the 50th percentile, the error bars are the 25th and 75th percentile, the plus symbols are the max and min, and the dashed line is ground truth.

3. Rejection Due to Distance from Shadow Generator

Hypothesis II states that it is important to choose shadow pixels far from the shadow generator to calculate optical depth. Higher elevation objects that surround a point block portions of the sky, reducing diffuse radiation components of the total radiance signal received at the satellite sensor. Figure 25 shows output from FASTEC when a percentage of pixels near the generator are eliminated from the total shadow region for both the north satellite dish in Solar Village and the GSFC building. The light grey region identifies pixels that are too close the shadow generator. As the percentage increases, more of the total shadow region is kept. Testing of the importance of this parameter was done using these scenes. Additionally, AOD was computed for the GSFC DSM file as the building shadow percentage threshold was varied with 10% increments.

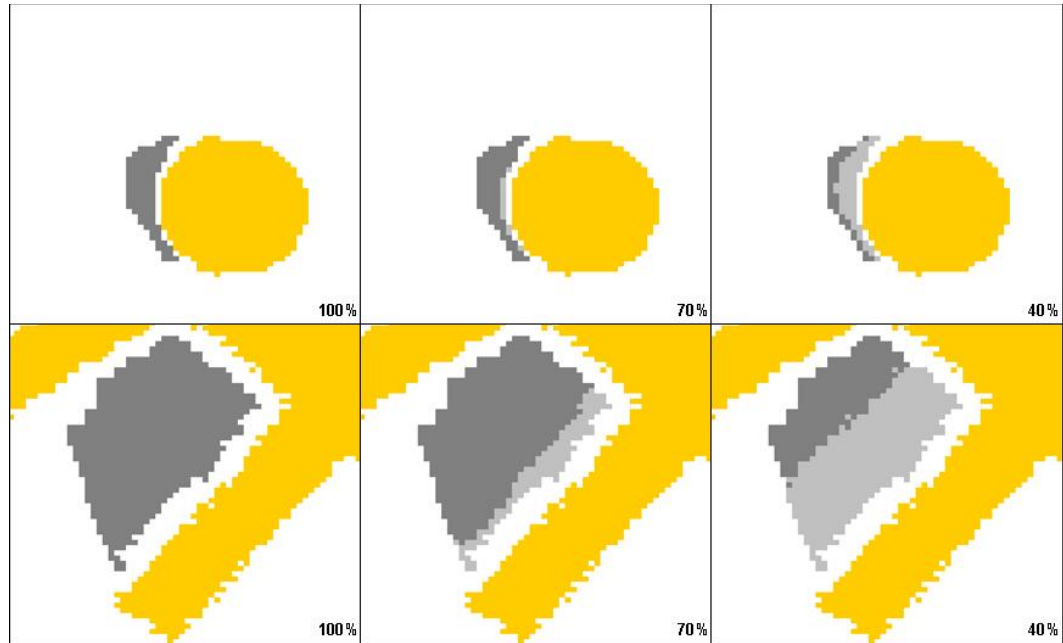


Figure 25. Example of target pixel rejection based on proximity to the shadow generator. Yellow indicates building pixels, dark grey indicates shadow pixels, and light grey indicates eliminated shadow pixels. Created using north satellite dish in Solar Village on April 12, 2006 (top panels) and the GSFC building on January 16, 2009 (bottom panels).

a. North Satellite Dish, Solar Village

Figure 26 depicts the spectral radiance based on distance from the shadow generator for the April 12, 2006 Solar Village image. For this test case, the edge pixel rejection variable was set to 1 to eliminate most of the partial shadow pixels from the sample. In general, spectral radiance increases as the distance from the shadow generator increases. The large radiance of pixels identified as being within 1.3 meters of the satellite dish is heavily influenced by partial shadow pixels in the southeast corner of the shadow. The correlation between the distance from shadow generator and spectral radiance is about 0.45 when including every shadow pixel, while eliminating the closest pixels from the sample increases correlation to 0.77. If the target selection variable that

rejects pixels based on their physical distance from the shadow generator were set to 2 or rejection by percentage were set to 80%, those partial shadow pixels would be marked *invalid* and eliminated from the calculation.

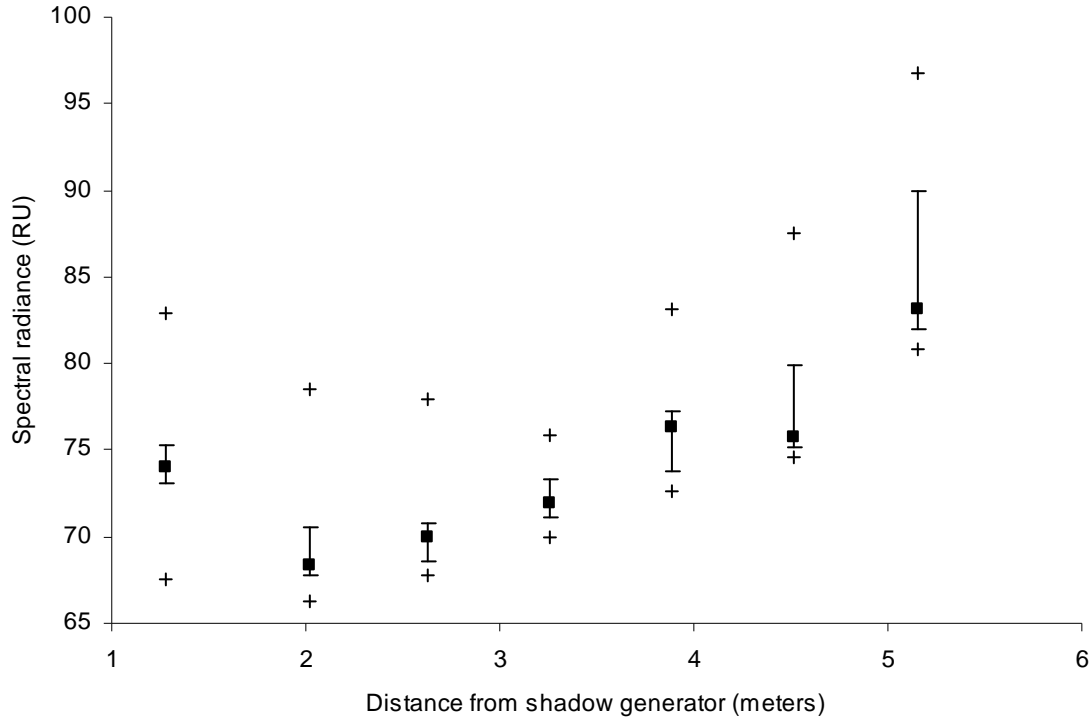


Figure 26. Spectral radiance vs. distance from the shadow generator (binned) for the Solar Village north satellite dish on April 12, 2006. For each bin, the box marks the 50th percentile, error bars are the 25th and 75th percentile, and plus signs are the maximum and minimum.

Table 5 displays the results for AOD calculations on the north satellite dish when varying the proximity to building by percentage threshold for the shadow region. Generally, AOD increases as more pixels close to the shadow generator are removed. The slight AOD decrease between 70% and 80% is due to higher radiance from partial shadow pixels near the satellite dish, which are included with the 80% threshold. The average shadow radiance increases from 73.04 RU to 78.06 RU as the percentage of building shadow is decreased from 80% to 30%. At 80% or greater, the entire shadow is used in the computation. Overall, AOD varies by 0.025 across the range of thresholds. Fifty percent of the change occurs from 30 to 40% when the pixel count

nearly doubles and the average shadow radiance decreases from 78.06 to 75.43 RU. In every case, the computed AOD is at least 0.04 lower than ground truth.

% of shadow used	Shadow pixel count	Non-shadow pixel count	Shadow Radiance	Non-shadow Radiance	AOD	Error
100	98	1084	73.04	159.7	0.179	0.067
90	98	1084	73.04	159.7	0.179	0.067
80	98	1084	73.04	159.36	0.180	0.066
70	86	1084	72.89	159.36	0.179	0.067
60	73	1084	73.14	159.7	0.180	0.066
50	55	1063	74.42	159.48	0.187	0.059
40	38	1021	75.43	160.09	0.191	0.055
30	21	933	78.06	160.47	0.204	0.042

Table 5. Results of varying proximity to building threshold percentage for north satellite dish from April 12, 2006 Solar Village image. Ground truth is 0.246.

b. Goddard Space Flight Center Building

Figure 27 shows the radiance for pixels binned by distance from the shadow generator for the GSFC building on January 16, 2009. In general, the 50th percentile value of the radiance increases slightly with distance from the building. The high radiance pixels near the shadow generator appear to be partial shadow pixels. Part of the variation in spectral radiance across the shadow is due to variations in surface reflectance from trees, cement, and grass surfaces in the scene. Other possible reasons for the variations across the shadow include rotation or distortion error between the DSM and satellite file and reflected direct sunlight off buildings near the shadow. The correlation between distance from the shadow generator and spectral radiance for all shadow pixels is 0.20, with it increasing to 0.31 when pixels less than 20 meters from the building are removed from the sample. This is much lower than the 0.45 and 0.77 correlations for the Solar Village scene.

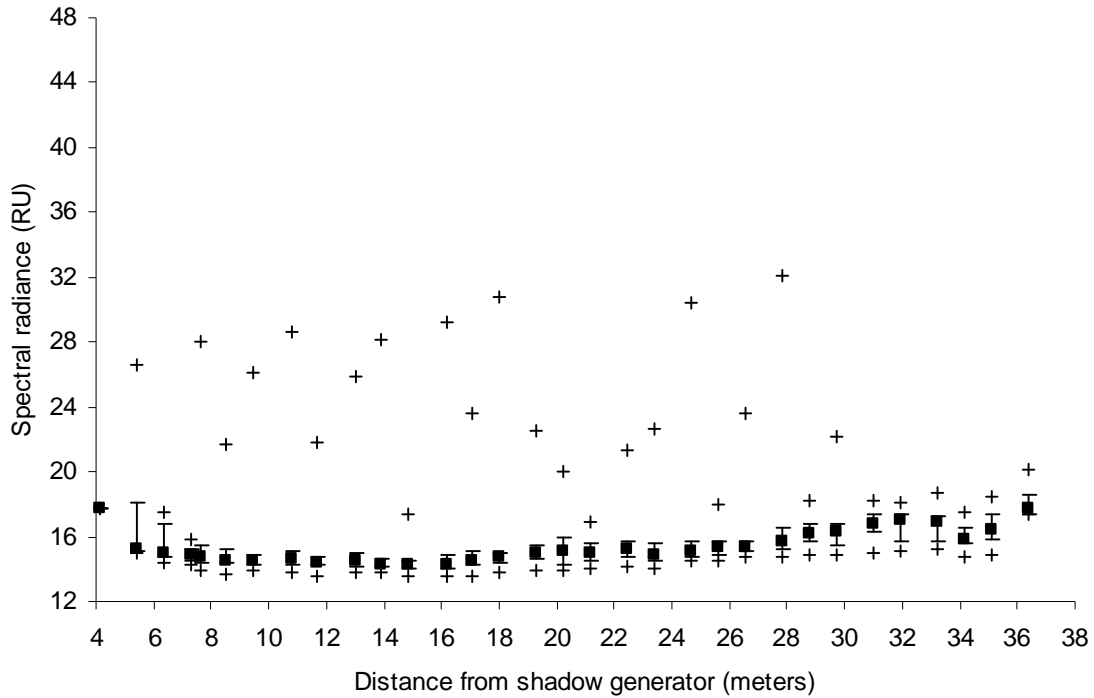


Figure 27. Spectral radiance vs. distance from the shadow generator (binned) for GSFC building on January 16, 2009. For each bin, the box marks the 50th percentile, error bars are the 25th and 75th percentile, and plus signs are the maximum and minimum.

Figure 28 is a plot of pixel radiances in the shadow region from the same scene. The sun is located to the SSE, casting the shadow to the NW. Subjectively, radiance appears to increase with distance from the shadow generator. Additionally, radiance is highest along the shadow edge, particularly along the northern edge of the shadow. This high radiance region to the north may be due to reflection off the wing of the building to the north or west. In both this scene and the Solar Village scene (not pictured), there is a region in the center of the shadow that appears to have the lowest radiance values. To further examine this relationship, another shadow in the GSFC DSM (pictured in Figure 25) was examined. The shadow cast by this tall, isolated building was much longer than wide. In this case, the correlation between distance from the shadow generator and spectral radiance was only 0.09 (results not pictured).

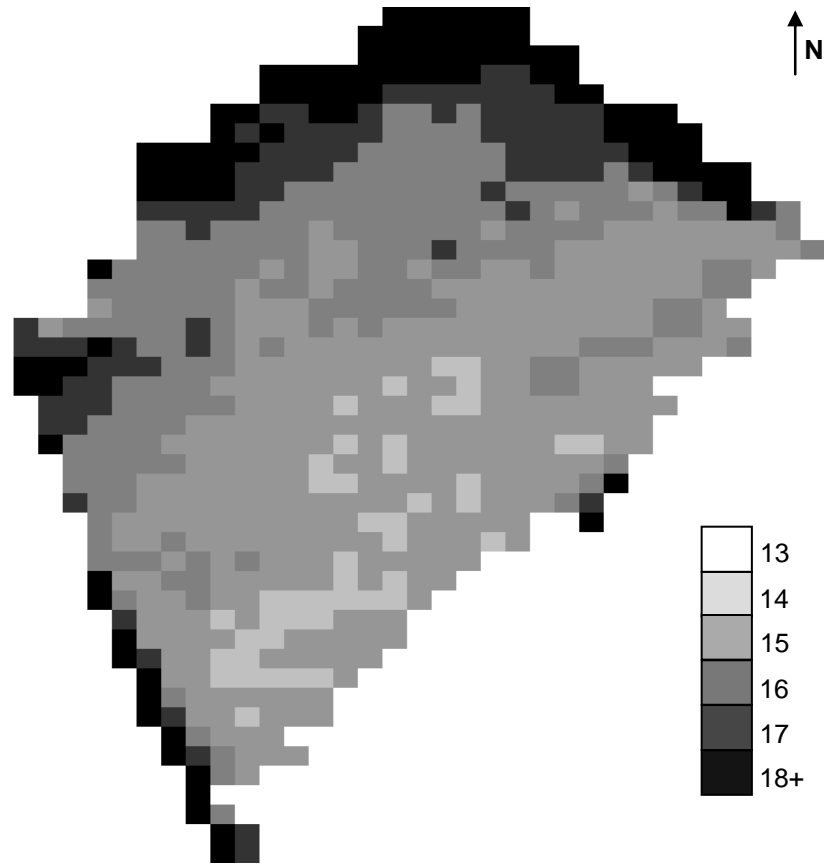


Figure 28. Plot of spectral radiance by pixel for the GSFC building from January 16, 2009. The GSFC building surrounds all sides except the southwest. The sun is located to the southeast.

Table 6 displays computed AOD values for the GSFC building as the building shadow percentage threshold changes from 100 to 20% in 10% increments. For this test, offset correction was enabled and the edge pixel rejection threshold was set to two. Generally, AOD increased as the threshold decreased and limited the shadow region to pixels further from the building. The overall variation in AOD is lower than the Solar Village case partly because of the larger number of shadow pixels associated with this building (667) and the large width of the shadow generator (about 23 pixels) relative to the length (about 15 pixels). Otherwise, the GSFC building and Solar Village scene show increasing AOD due to increased shadow radiance as more of the pixels near the building are rejected.

% of shadow used	Shadow pixel count	Non-shadow pixel count	Shadow Radiance	Non-shadow Radiance	AOD	Error
100	751	179	15.65	37.92	0.034	0.002
90	751	179	15.65	37.92	0.034	0.002
80	733	179	15.64	37.92	0.034	0.002
70	626	179	15.74	37.92	0.035	0.001
60	501	167	15.9	37.82	0.037	-0.001
50	388	143	16.11	37.52	0.040	-0.004
40	276	101	16.41	37.62	0.043	-0.007
30	168	71	16.77	38.84	0.044	-0.008
20	68	28	17.28	44.03	0.035	0.001

Table 6. Results of varying proximity to building threshold percentage for GSFC building wing from January 16, 2009 GSFC image. Ground truth is 0.036.

Figure 29 displays the range of AOD values for the entire GSFC DSM using the October 26, 2006 image. For this test, offset correction was enabled and the building shadow percentage was varied from 10% to 100% with a 10% increment. For thresholds above 50%, a lone tree shadow with high AOD (greater than 0.25) was eliminated manually. For thresholds 50% and below, tree shadows were not present. Otherwise, this graph shows minor variation in both the 50th percentile and range of AOD values for all shadows in the scene. In every case, the result shows a low bias of approximately 0.05 and the spread across all AOD values varied between 0.026 and 0.055. These results do not show the percent of building shadow threshold as particularly important to the shadow method although the low optical depth of the scene may contribute to the lack of change in AOD. For scenes other than Solar Village, the building shadow percentage threshold will be set to 50% to increase the average radiance slightly. To keep the Solar Village shadow pixel counts above the minimum pixel threshold and reduce partial shadow pixels near the shadow generator, the physical distance from the shadow generator threshold will be set to two.

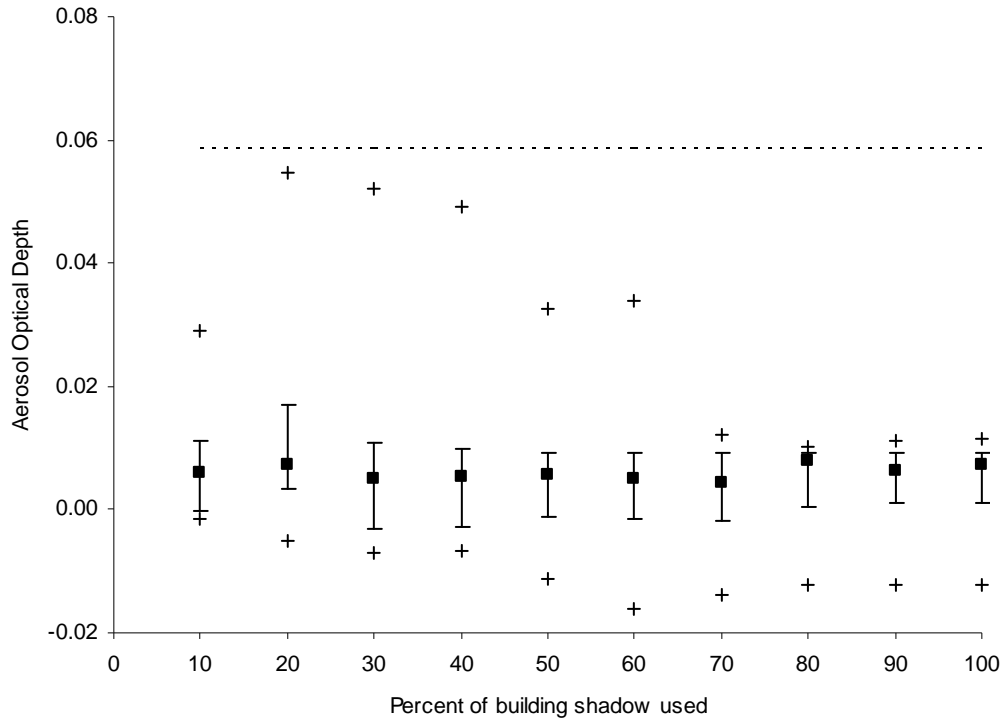


Figure 29. AOD vs. percent of building shadow used for the October 26, 2006 GSFC image. The black box is the 50th percentile, the error bars are the 25th and 75th percentile, the plus symbols are the max and min, and the dashed line is ground truth.

4. Rejection Due to Sky Dome Blockage

Hypothesis III states that sky dome blockage is important when choosing valid shadow and sunlit pixels to calculate AOD. This is due to blocked diffuse sky radiance (negative contribution to pixel radiance) and direct reflection off taller objects (positive contribution to pixel radiance). The sky dome blockage threshold was varied on the January 16, 2009 image over the GSFC building to verify the sky dome blockage procedure worked properly. Figure 30 displays the change to the shadow region with the sky dome blockage threshold set to 30%. In this example, light grey signifies invalid shadow pixels, which exceeded the sky dome blockage threshold, dark grey identifies valid shadow pixels, and yellow approximates the GSFC building. The invalid region is due to higher sky dome blockage from the building wing to the northeast of the shadow and to a lesser extent the wing to the northwest.

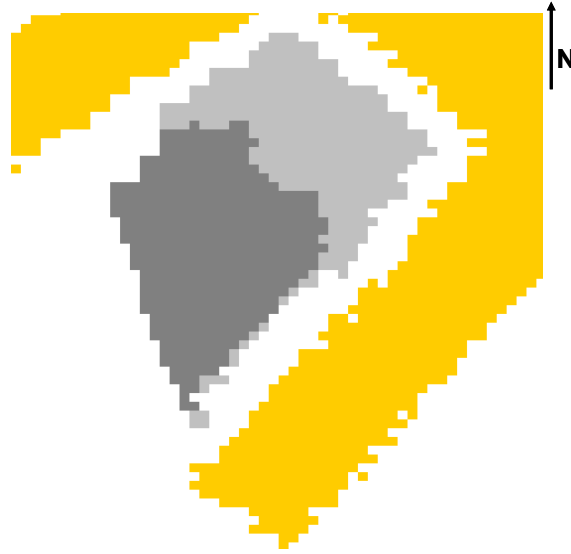


Figure 30. Example of sky dome blockage for the January 16, 2009 image of the GSFC building. Yellow is building pixels, dark grey is valid shadow pixels, and light grey is invalid shadow pixels from 30% or greater sky dome blockage.

a. North Satellite Dish, Solar Village

The north satellite dish in Solar Village provided a simple scene to test the significance of sky dome blockage as it relates to spectral radiance. The presence of the small building to the west of the dish impacts sky dome blockage and provides a way to test the accuracy of the calculation. The maximum vertical blockage of the 4 m tall building is about 42 degrees for the closest shadow pixels. The building affects up to 13 of the 36 azimuths used in the computation with the azimuth interval set to 10 degrees. Therefore, the maximum contribution of this building to sky dome blockage within the shadow is about 0.119 (see Figure 31). By subtracting the sky dome blockage values with the building removed from the blockage with the building included, the maximum difference was 0.119 and decreased as distance from the building increased. Considering the typical sky blockage of shadow pixels within this shadow is about 0.30, the maximum contribution of the building to sky dome blockage is 40%. The correlation between sky dome blockage and distance from the shadow generator is -0.79 with the building and -0.87 without the building. Correlation is not -1.0 because of the presence of the satellite

dish to the south, variation in the north satellite dish pixel elevations, and possible incomplete sampling angles in the sky dome blockage calculation.

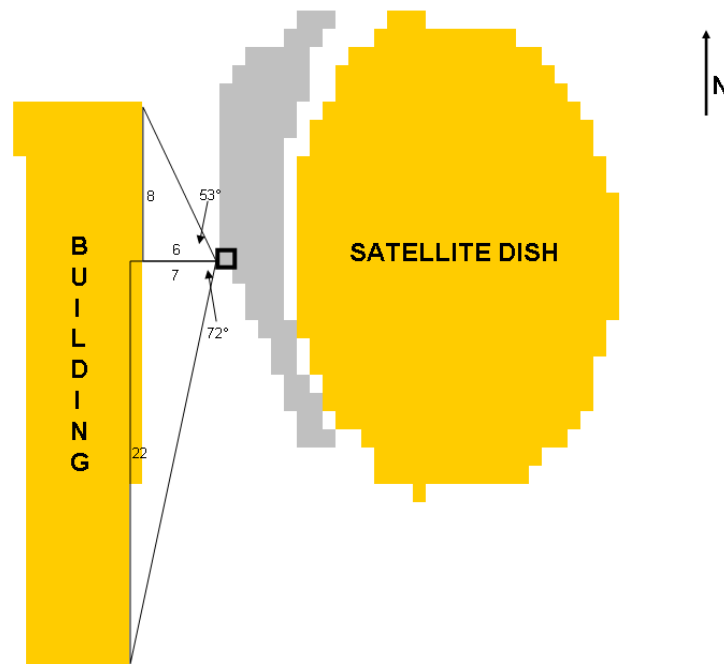


Figure 31. Sky dome blockage test using April 12, 2006 Solar Village image. Grey region is shadow pixels identified by the automated method. Numbers mark geometrically relevant information for the calculation on the highlighted pixel.

Figure 32 is a graph of the spectral radiance versus sky dome blockage, in 2.5% bins, for shadow and sunlit pixels for the north satellite dish. Partial shadow pixels, because of the edge pixel rejection variable being one, explain the large maximum radiance values in some of the shadow bins. Regarding shadow pixels, radiance decreases with increasing dome blockage until the 40% bin where the radiance steadily increases. The increase may be due to diffuse radiance from the 4 m tall building, partial shadow pixels along the shadow/shadow generator edge, or reflection of direct sunlight off the side of the building into the shadow. When the sky dome blockage threshold for the shadow region was varied from 30% to 50%, AOD changed by less than 0.01 (graph not pictured). Dropping the threshold below 30% provided less than the 15 valid shadow pixels necessary to perform the calculation.

The variation in the radiance of the sunlit pixels in Figure 32 appears random with no discernable trends as sky dome blockage increases. This is likely due to the overwhelming influence of the direct portion of the total signal radiance. The relatively low minima between 15 and 25% dome blockage were due to five partial shadow pixels along the edge of the building to the west of the satellite dish. AOD varied by less than 0.003 as the sunlit pixel sky dome blockage maximum threshold increased from 5% to 100%. Based on these results, sky dome blockage does not appear to be very important for either the shadow or sunlit region in this Solar Village image.

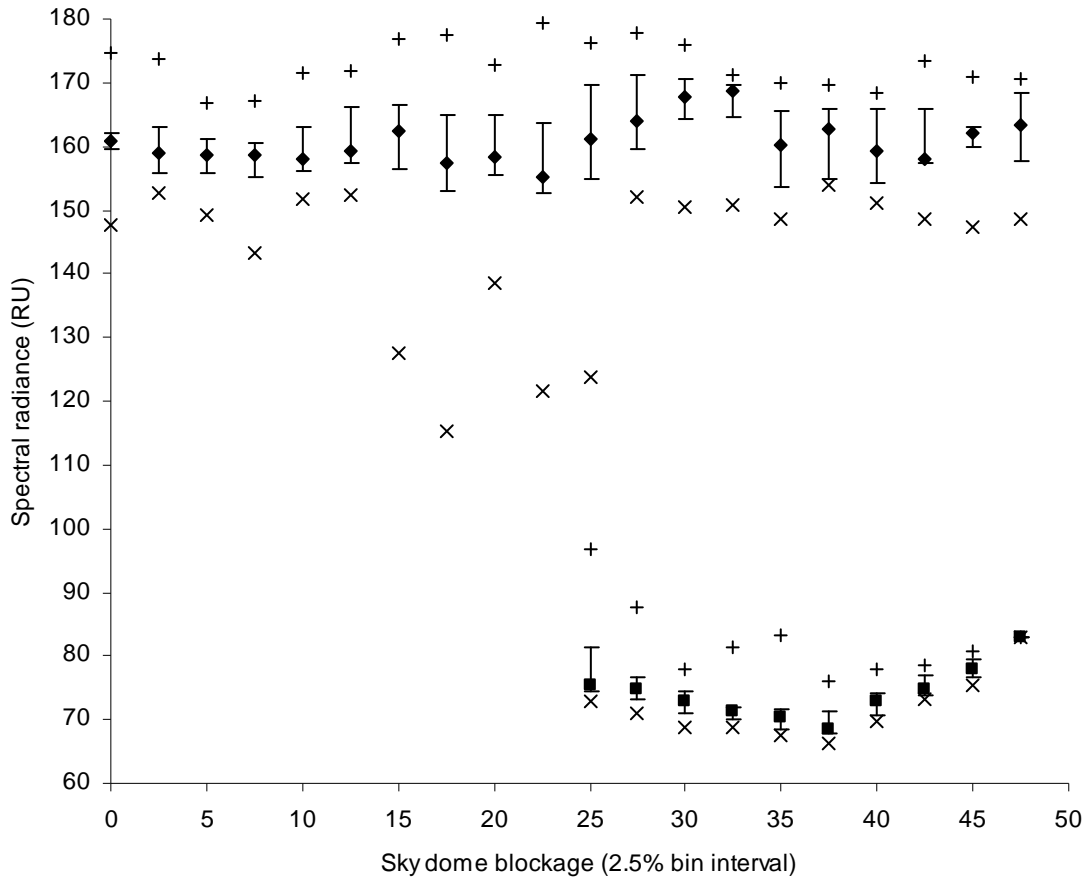


Figure 32. Spectral radiance of sky dome blockage bins for the April 12, 2006 Solar Village image. For each bin, the box (shadow) or diamond (sunlit) is the 50th percentile, error bars are the 25th and 75th percentile, plus symbols are the maximum, and “x” symbols are minimum radiances.

b. Goddard Space Flight Center Building

The Goddard Space Flight Center building scene provided real DSM data to analyze the impact of sky dome blockage on shadow and sunlit regions. The 20 meter tall building is composed of several wings off a curved connecting building (see Figure 33). The shadow region is northwest of the southernmost wing with the sunlit region west of the shadow. The least-blocked shadow pixels are in the southwest portion of the shadow while the most-blocked shadow pixels are along the northeast edge. The least-blocked sunlit pixels are on the southeast side while the most-blocked shadow pixels are along the north side of the sunlit region.

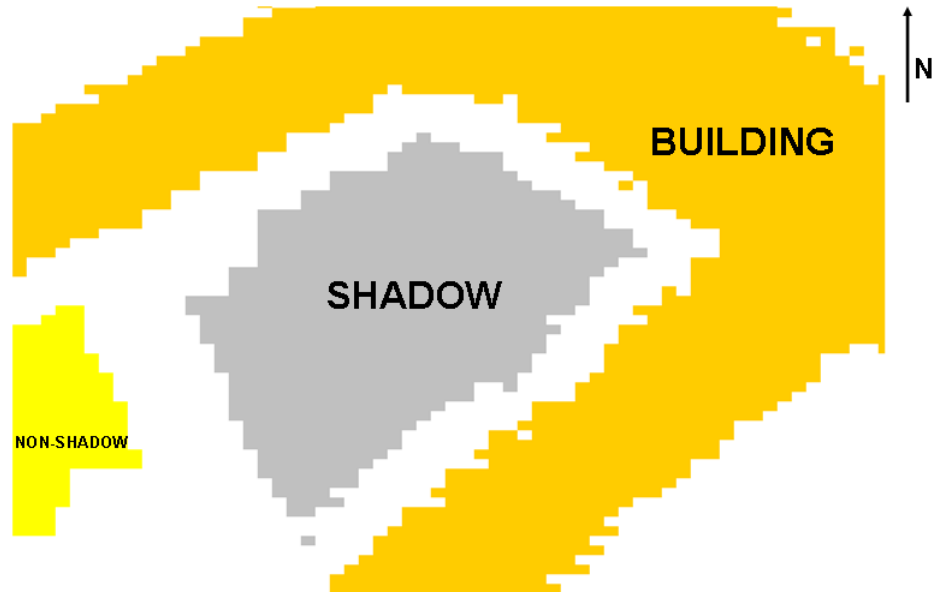


Figure 33. Shadow used for sky dome blockage testing for Goddard Space Flight Center building, January 16, 2009 image.

Figure 34 is a graph of the spectral radiance as sky dome blockage, in 4% bin intervals, varies for shadow and sunlit pixels for the GSFC building using the January 16, 2009 image. For the shadow bins, the maximum radiance pixels fall along the outer edge of the shadow suggesting they may be partial shadow pixels caused by position error, despite offset correction being performed, between the DSM and satellite file. As

sky dome blockage percentage increases, radiance decreases slightly, only to increase above 32%. For shadow pixels, correlation between sky dome blockage percentage and spectral radiance is 0.35.

As blockage increases for sunlit pixels, the spectral radiance also increases but 144 of the 179 sunlit pixels are less than 16% blocked. The lack of blocked pixels above 16% helps explain the large changes in the 50th percentile value of spectral radiance at those blocked percentages. Correlation between sky dome blockage and spectral radiance is 0.41 in the sunlit region. As discussed previously, when examining sunlit pixels, the direct reflection portion of the total signal dominates and it is difficult to determine the impact of sky dome blockage. If it were possible to remove the direct reflectance portion of the signal, a pattern might emerge. Otherwise, radiances in the sunlit region are highest near the building. This is likely due to higher surface reflectance for those pixels although additional radiance from reflection of direct sunlight off the building may contribute.

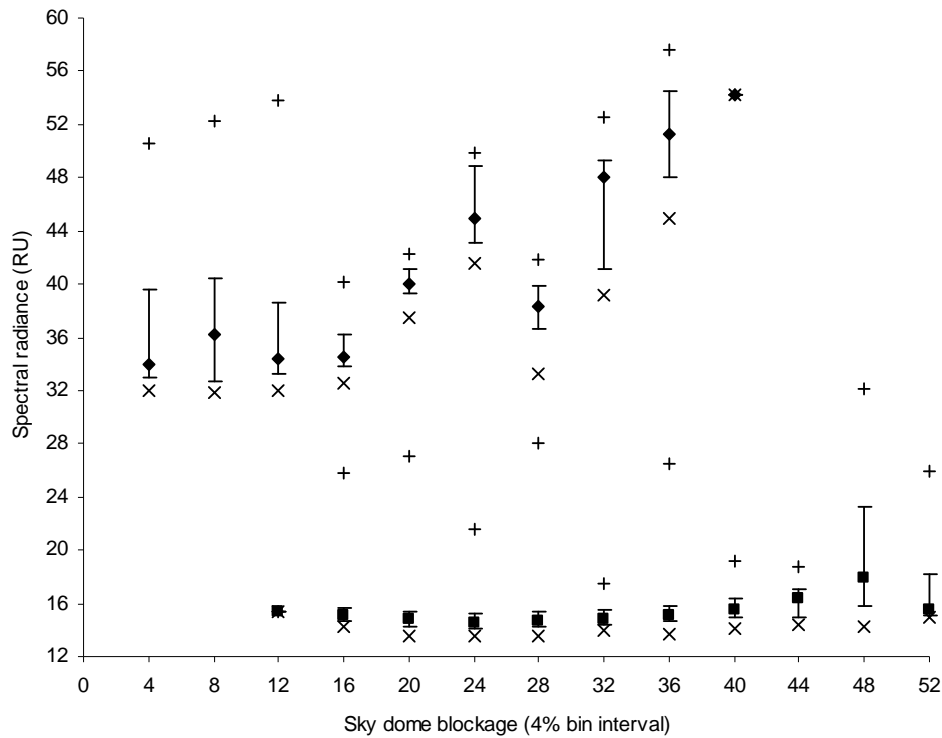


Figure 34. Spectral radiance of sky dome blockage bins for the GSFC building on January 16, 2009. For each bin, the box (shadow) or diamond (sunlit) is the 50th percentile, error bars are the 25th and 75th percentile, plus symbols are the maximum, and minus symbols are the minimum radiances.

Table 7 displays the results of FASTEC as the shadow sky dome blockage maximum threshold is varied. Although the AOD values are quite small in each case, the average shadow radiance and AOD increase as the sky dome blockage threshold increases. Part of the increase is due to the higher radiances associated with high sky dome blockage pixels although this increase is partially countered by variation in offset correction as the threshold changes (see Table 9). The change in offset correction values also contributes to the variation in sunlit radiance. If offset correction perfectly aligned the DSM and satellite files, sunlit radiance would vary much less than it does in this table.

Shadow sky dome blockage threshold	Shadow pixel count	Non-shadow pixel count	Shadow Radiance	Non-shadow Radiance	AOD	Error
0.15	20	152	14.09	34.31	0.026	-0.010
0.20	184	179	14.42	34.66	0.028	-0.008
0.25	324	180	14.75	37.6	0.025	-0.011
0.30	411	180	14.81	37.6	0.026	-0.010
0.35	509	180	15.03	38.39	0.026	-0.009
0.40	614	179	15.06	37.72	0.028	-0.008
0.45	708	179	15.36	37.92	0.031	-0.005
0.50	750	179	15.65	37.92	0.034	-0.002
0.55	751	179	15.65	37.92	0.034	-0.002

Table 7. Results of varying shadow sky dome blockage maximum threshold for January 16, 2009 image of GSFC building wing. Ground truth is 0.036.

Table 8 shows the results from FASTEC as the sunlit sky dome blockage maximum threshold is varied for the GSFC building shadow using the January 16, 2009 image. Generally, sunlit radiance increases as the sunlit sky dome blockage threshold is increased as expected from Figure 34. Since shadow radiance is fixed, AOD decreases but the overall change is quite small. This is due to the majority of sunlit pixels having sky dome blockage below 15%.

Non-shadow sky dome blockage threshold	Shadow pixel count	Non-shadow pixel count	Shadow Radiance	Non-shadow Radiance	AOD	Error
0.05	751	22	15.65	36.87	0.037	0.001
0.10	751	96	15.65	37.37	0.035	-0.001
0.15	751	137	15.65	36.66	0.037	0.001
0.20	751	156	15.65	36.93	0.036	0.001
0.25	751	169	15.65	37.42	0.035	-0.001
0.30	751	173	15.65	37.52	0.035	-0.001
0.35	751	178	15.65	37.83	0.034	-0.002
0.40	751	179	15.65	37.92	0.034	-0.002
0.45	751	179	15.65	37.92	0.034	-0.002

Table 8. Results of varying the sunlit sky dome blockage maximum threshold for January 16, 2009 image of GSFC building wing. Ground truth is 0.036.

Finally, the sky dome blockage thresholds were varied for the entire GSFC DSM file using the October 26, 2006 image. Figure 35 is a plot of the results of running FASTEC while varying the sunlit sky dome blockage maximum threshold. This plot shows little variation in AOD calculations as the threshold changes. This is due to the fact that almost all the pixels in the sunlit regions have sky dome blockage less than 0.05 as evidenced by the average sunlit pixel count increasing from 563 to 677 as the threshold increases from 0.05 to 0.30. At thresholds beyond 0.30, sunlit pixel count does not change.

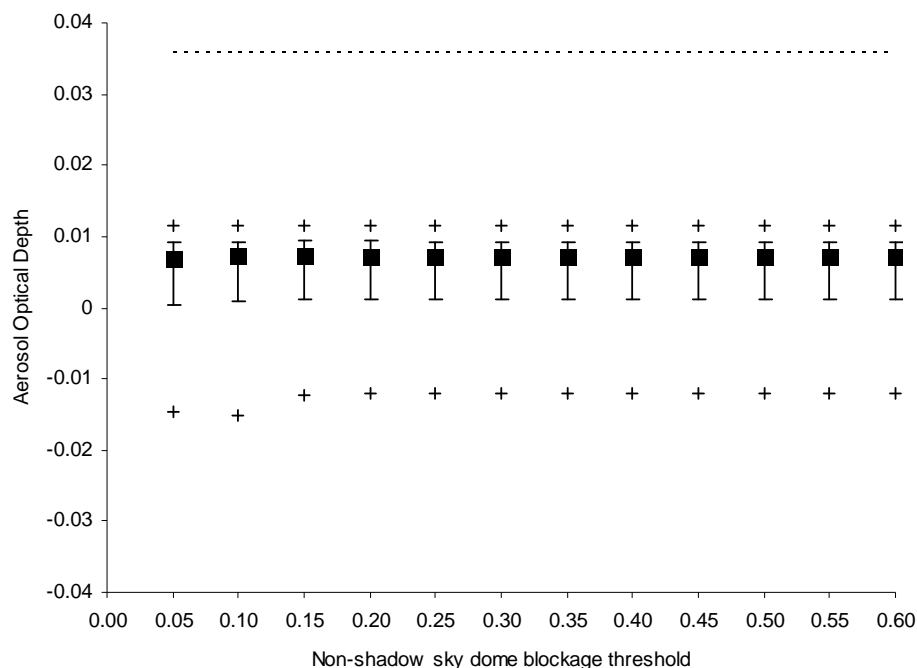


Figure 35. AOD vs. sunlit pixel sky dome blockage maximum thresholds for the GSFC DSM file from January 16, 2009. For each threshold, the box is the 50th percentile, the error bars are the 25th and 75th percentile, and plus symbols mark the maximum and minimum AOD.

Figure 36 is a plot of the results of running FASTEC while varying the shadow sky dome blockage maximum threshold. The minimum AOD (-0.11) is below the y-axis for the 0.05 threshold. Setting shadow sky dome blockage thresholds to more than 0.60 does not eliminate any pixels. As opposed to changing sunlit dome blockage maximum threshold, despite small AOD values, changes in the 50th percentile values are apparent. These changes mirror changes in the row and column offset for the different thresholds (see Table 9). Where the row and column offset values are similar, the results in the figure are similar. For example, when the threshold is 30% or higher, offset correction adjustments are within two pixels of the baseline and the difference between the maximum and minimum AOD is less than 0.002. Based on the inconclusive results of these tests, sky dome blockage thresholds will be disabled for later testing.

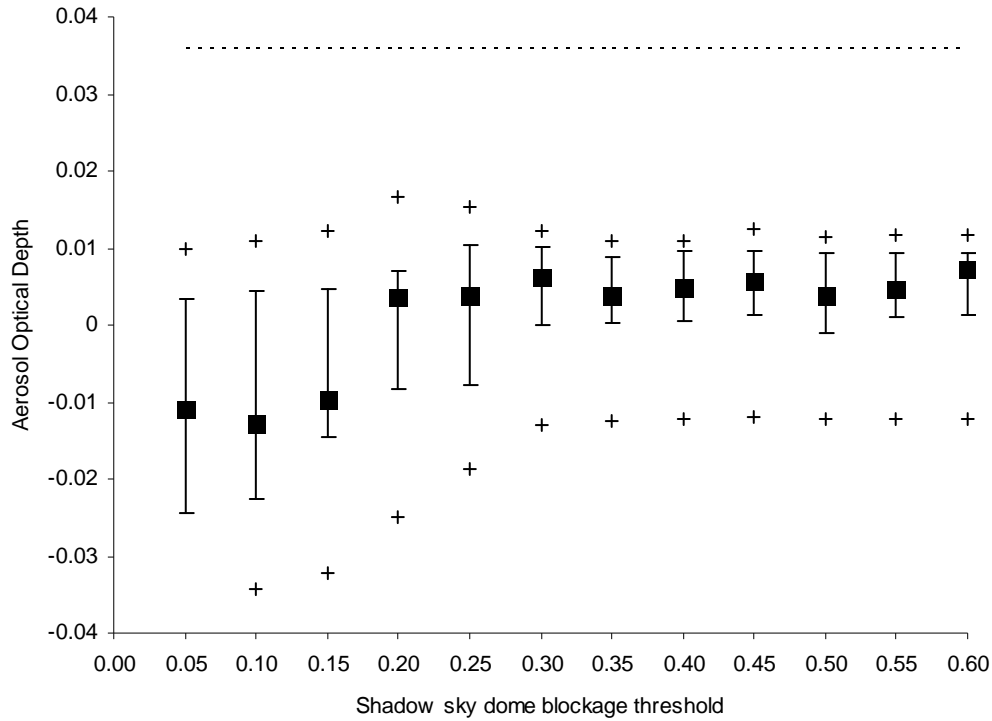


Figure 36. AOD vs. shadow pixel sky dome blockage maximum thresholds for the GSFC DSM file from January 16, 2009. Boxes are the 50th percentile, the error bars are the 25th and 75th percentile, and + symbols mark the max and min AOD.

Shadow sky dome blockage threshold	Row Offset	Col Offset	Distance from baseline (2,9)
0.05	13	11	11.18
0.10	10	9	8.00
0.15	10	9	8.00
0.20	9	9	7.00
0.25	6	8	4.12
0.30	4	9	2.00
0.35	3	8	1.41
0.40	3	8	1.41
0.45	3	9	1.00
0.50	1	8	1.41
0.55	2	9	0.00

Table 9. Offset correction values for different shadow sky dome blockage thresholds for January 16, 2009 image over the GSFC DSM. Baseline offset correction determined by disabling the sky dome blockage maximum threshold.

5. Rejection of Extreme Radiances

a. North Satellite Dish, Solar Village

Hypothesis IV states that eliminating the extreme radiances values from the sample improves AOD calculation. Figure 37 shows the sorted spectral radiances of shadow and sunlit pixels for the north satellite dish in Solar Village from the April 12, 2006 image using FASTEC. The first approximately 100 sunlit pixels increase in radiance steeply due to partial shadow pixels along the northwest side of the small building west of the satellite dish and partial shadow pixels from both satellite dish shadows. Including these pixels in the sunlit region average causes a slight decrease in the average radiance for the region although the large number of sunlit pixels lessens the influence of these darker pixels. When the 105 darkest (lowest 10%) pixels are removed from the sample, the average sunlit radiance increases by 1.4 RU, however, when the darkest and brightest extremes are removed equally across the sunlit region, the change in radiance is quite small (see Table 11).

For shadow pixels, the overall slope of the increasing radiances is steeper and the six brightest pixels have noticeably higher radiances than the rest of the sample. The overall steeper slope of the shadow region when compared with the sunlit region appears to be partly due to the smaller number of pixels in the shadow region (98 vs. 1059 pixels). The significantly brighter pixels are partial shadow pixels along the shadow edges. Removing these six pixels causes average radiance to decrease by almost 1.2 RU. Removing these extreme radiance pixels from both regions results in a 2.6 RU increase in the radiance difference and computed AOD to be .0083 lower. Although this lowering of AOD pushes the results further from ground truth, it eliminates invalid sunlit pixels and properly applies the shadow method.

When the darkest and brightest extremes are removed equally from the shadow region, the largest change in shadow radiance occurs when 10% of the extremes are removed (see Table 10) and radiance difference increases from 86.8 RU to 87.6 RU, decreasing AOD from 0.192 to 0.171. The radiance difference change is less than 0.2

RU as additional percentages of the extremes are eliminated. For sunlit pixels, radiance difference changes by 0.3 or less across all combinations (see Table 11).

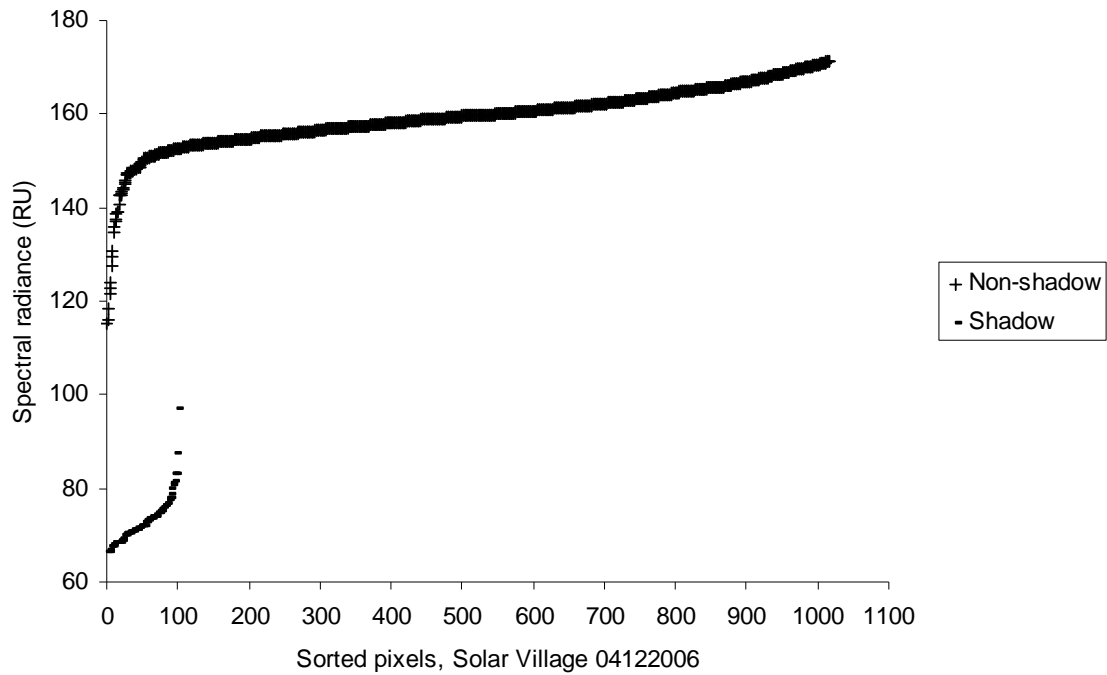


Figure 37. Spectral radiance of usable pixels for shadow and sunlit regions for Solar Village north satellite dish and the April 12, 2006 satellite image.

Lower radiance threshold	Upper radiance threshold	Min pixel position	Max pixel position	Min pixel radiance	Max pixel radiance	Average shadow radiance	Radiance difference
0	100	1	98	66.3	96.8	73.0	86.8
10	90	9	88	67.9	77.9	72.3	87.6
20	80	19	78	68.9	75.7	72.2	87.6
30	70	29	68	70.3	74.0	72.2	87.7
40	60	39	58	71.1	73.4	72.1	87.7
50	50	49	49	72.1	72.1	72.1	87.8

Table 10. Results of varying extreme radiance thresholds for Solar Village north satellite dish shadow region and the April 12, 2006 satellite image.

Lower radiance threshold	Upper radiance threshold	Min pixel position	Max pixel position	Min pixel radiance	Max pixel radiance	Average non-shadow radiance	Radiance difference
0	100	1	1059	115.3	179.3	159.9	86.8
10	90	105	953	152.8	168.8	160.1	87.0
20	80	211	847	155.0	165.6	159.9	86.9
30	70	317	741	156.8	163.0	159.8	86.8
40	60	423	635	158.4	161.2	159.8	86.7
50	50	529	529	159.7	159.7	159.7	86.7

Table 11. Results of varying extreme radiance thresholds for Solar Village north satellite dish sunlit region and the April 12, 2006 satellite image.

b. Goddard Space Flight Center Building

Figure 38 is a plot of the sorted spectral radiance of usable shadow and sunlit pixels for the GSFC building using the January 16, 2009 image. In this case, the shadow region is much larger than the sunlit region and the subsequent slopes are reversed with the smaller sunlit region (179 pixels) being steeper than the shadow region (751 pixels). Otherwise, the shape of the shadow region curve is similar to the shadow region curve from Solar Village with the highest radiance pixels (32 of 748) being significantly brighter than the rest of the dataset. Interestingly, the sunlit region curve has a different shape than Solar Village with the brightest pixels being much brighter than the rest of the sample due to variations in surface reflectance from two distinct surface types; some pavement with a primarily grassy surface. Otherwise, the impact on the radiance difference as larger percentages of the extremes from the total sample are removed is very similar to the Solar Village case where removing 10% of the darkest and brightest pixels has the largest affect on the average radiances (results not pictured).

Although this suggests that 10% is the ideal threshold of the extremes, the small variation as more of the extremes are rejected leaves open the possibility that larger portions of the extremes can be trimmed without significantly changing the resulting AOD values. The benefit to trimming larger percentages of the extreme radiances should be most evident when calculating AOD over heterogeneous surfaces or when overcoming issues with offset correction or partial shadow pixel rejection thresholds. The results

from the GSFC and Solar Village tests both indicate that any threshold over 10% should provide representative samples of the shadow/sunlit regions.

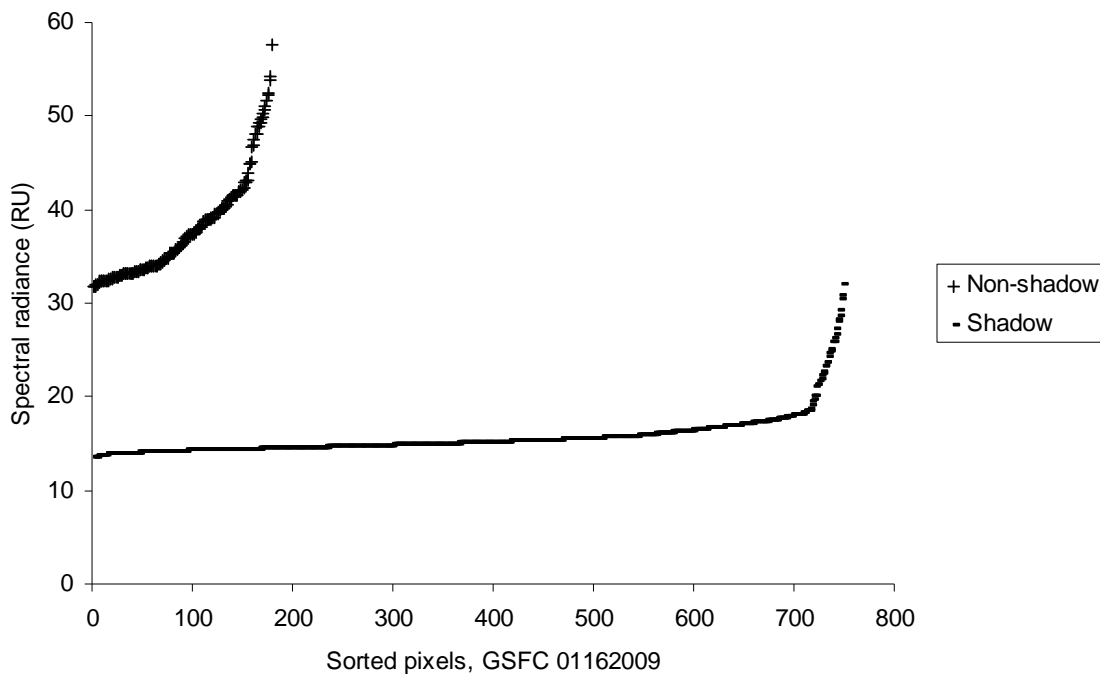


Figure 38. Spectral radiance of usable pixels for shadow and sunlit regions for GSFC building and the January 16, 2009 image.

Figure 39 displays the results from running FASTEC on the GSFC DSM for the October 26, 2006 image with different thresholds of extreme radiance rejections. In each case, both extremes were trimmed an equal percentage for both the shadow and sunlit regions. This graph highlights the fact that computed AOD values are very consistent for each of the nine usable shadows in this image, regardless of the threshold setting. In this scene, 3 of the 9 AOD values are consistently negative regardless of the threshold. These negative values occur when molecular Rayleigh optical depth is subtracted from total optical depth. Otherwise, computed AOD values for each building vary by less than 0.02 as the extreme rejection values change. These facts suggest the threshold has little impact on the results, however, the true AOD for this scene is 0.059, well below the recommended threshold of 0.10 (Vincent 2006). In addition, the minimum building height setting happens to select buildings whose shadows fall on largely homogeneous surfaces, reducing the impact of these variations of the extreme

rejection threshold. Based on the findings from this section, the extreme rejection thresholds will be set to 25% for the whole DSM tile tests in the next section. This ensures the middle 50% of radiances in the shadow/sunlit regions are used to compute optical depth and should minimize variations in AOD, making the results more precise.

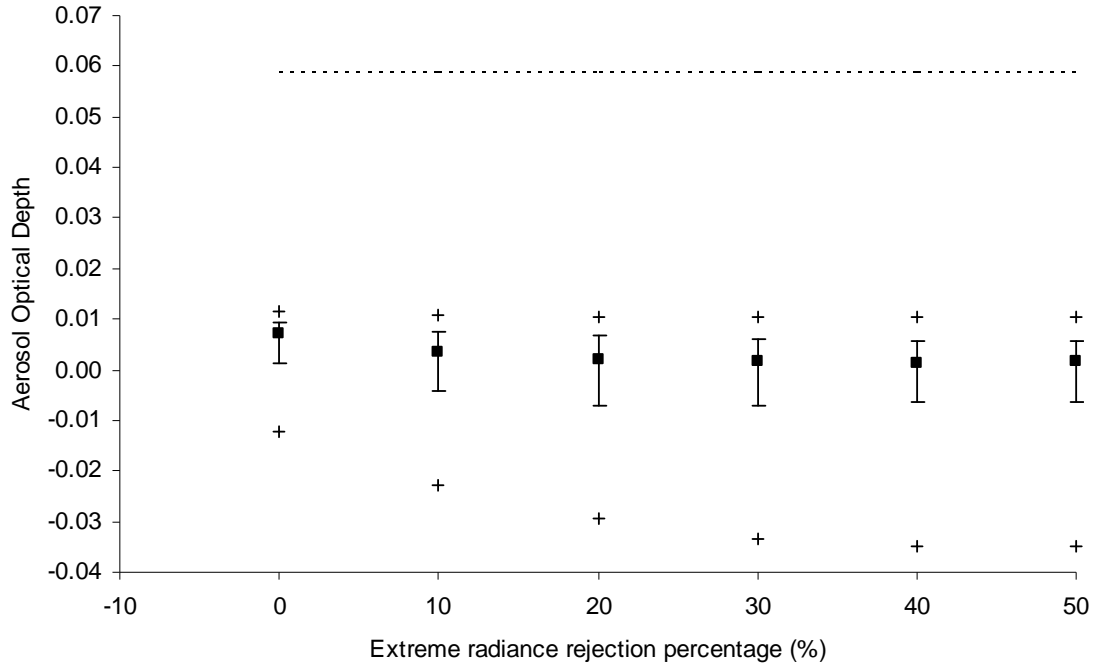


Figure 39. Aerosol optical depth using different extreme radiance rejection percentages on the GSFC DSM file and the October 26, 2006 image. For each threshold, the box is the 50th percentile, the error bars are the 25th and 75th percentile, plus symbols mark the maximum and minimum, and the dotted line marks ground truth AOD.

B. WHOLE SCENE AOD CALCULATION

1. Solar Village

The first full scene investigation of FASTEC was conducted using the manually created Solar Village elevation file and 14 satellite images (5 multispectral, 9 panchromatic) with corresponding ground truth AERONET data. This scene consisted of simple elevation data with high surface reflectance in a desert region. Figure 40 is the manually created 64 cm horizontal resolution elevation file covering an approximately 3600 square meter area about 200 meters northeast of the AERONET station (located at

N 24° 54' 25" N, E 46° 23' 49"). The surface elevation was set to 1 m, the rectangular building elevation was set to 5 m, and the satellite elevations were set to about 14 meters. Appendix D lists the configuration settings with minimum building height set to six to ensure AOD calculations were only performed on the two satellite dishes, not the small rectangular building. The satellite dishes were movable and their orientation was occasionally different than pictured.

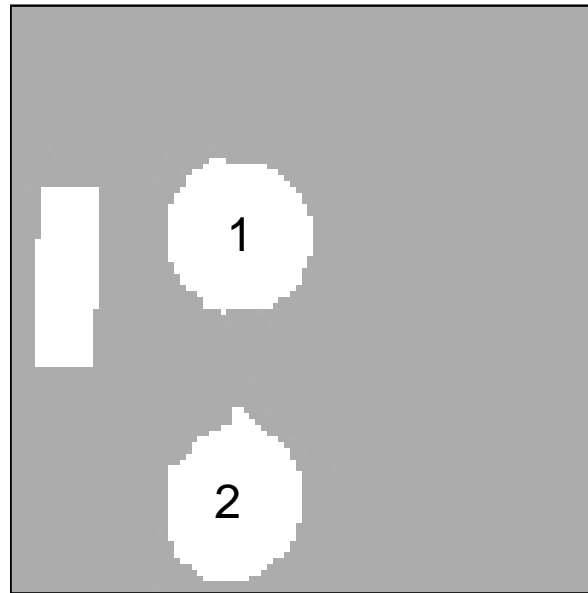


Figure 40. Manually created DSM for Solar Village. The (1) north and (2) south satellite dishes were estimated to be 13 meters tall and the building was estimated to be 4 meters tall.

a. Multispectral Images

Figure 41 displays the red, green, and blue (RGB) channels from the five multispectral QuickBird images that were evaluated using FASTEC. The NIR channel was also evaluated (not pictured). Ground truth best fit curves were determined with level 2.0 AERONET daily average AOD whenever it changed by less than 0.02. In the case of the April 30, 2006 image, level 2.0 AERONET data stopped at 0707 and the image was collected at 0755. Level 1.0 data showed AOD increasing rapidly during the satellite collection time. Surface visibility at Riyadh International Airport, located approximately 15 miles southeast of the test location, decreased from 8 km to 4 km between 0800 and 1000 (the 0900 observation is missing). With a westerly wind of 8-10

knots during that period, it would take between one and two hours for dust to advect over Riyadh from the region where the AERONET site is located. Based on Koschmieder's equation (Horvath 1971), these AOD values are consistent with observed surface visibility (see Equations (20) and (21)):

$$\text{Vis} = \frac{3.912}{\sigma_e} \quad (20)$$

$$\sigma_e = \frac{\delta_a}{H} \quad (21)$$

where δ_a is AOD, σ_e is the extinction coefficient, and H is the height of the planetary boundary layer. For this day, the mean of the two surrounding level 1.0 AERONET samples was used instead of the daily average. In the October 19, 2005 and the November 30, 2007 images, satellite dish orientations were noticeably different from the elevation file.

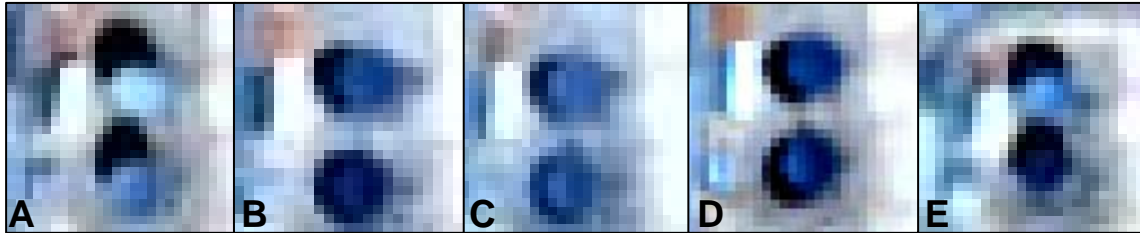


Figure 41. Multi-spectral imagery for Solar Village testing on (A) October 19, 2005, (B) April 12, 2006, (C) April 30, 2006, (D) May 26, 2007, and (E) November 30, 2007 with 2.4 meter resolution QuickBird data.

Basic data for each image test is listed in Table 12. Relatively large shadows (with a pixel count of more than 100) were identified in the October and November images while the April and May images had relatively small shadows. Offset correction shifted the DSM less than 20 meters in any direction for each image. In the May 26 image the mean sun azimuth and elevation information in the metadata file that accompanied the image was incorrect (150.2 and 44.9 respectively) and was adjusted by hand based on historical data from the Naval observatory.

Date	Time	Sun Azimuth	Sun Elevation	Row Offset	Column Offset	Satellite Dish	Shadow Pixel Ct	Non-shadow Pixel Ct
10/19/2005	0752	160.2	53.4	-17	31	1	113	643
						2	101	658
4/12/2006	0754	135.4	68.4	3	-2	1	27	551
						2	33	588
4/30/2006	0755	124.3	73.5	-8	7	1	13	476
						2	11	576
5/26/2007	0801	105.2	77.6	-4	-13	1	6	382
						2	9	553
11/30/2007	0754	164.9	42.2	-2	29	1	107	469
						2	101	560

Table 12. Date, time, sun azimuth, offset correction, and pixel counts for the satellite dish shadows in the Solar Village multispectral imagery.

In general, AOD values using FASTEC were quite accurate with bias less than 0.05 and standard deviation less than 0.08 (see Figures 42-45 and Table 13). Using Equations (20) and (21), this standard deviation equates to a horizontal visibility variation of less than 1.5 km when AOD is 0.5 or greater and the planetary boundary layer height is 1 km. The largest error was found in the two April images. On April 30, 2006, level 1.0 data showed rapidly increasing AOD to over 1.0 around the time the image was collected. It is interesting that FASTEC showed an unusually large decrease in AOD between channels when comparing April 30, 2006 with the other days. This may be due to the size of the aerosols present or due to problems with the shadow method when optical depth is high. Otherwise, the 10 data points showed a slight high bias for the blue channel and a slight low bias for the others with each channel error standard deviation less than 0.08.

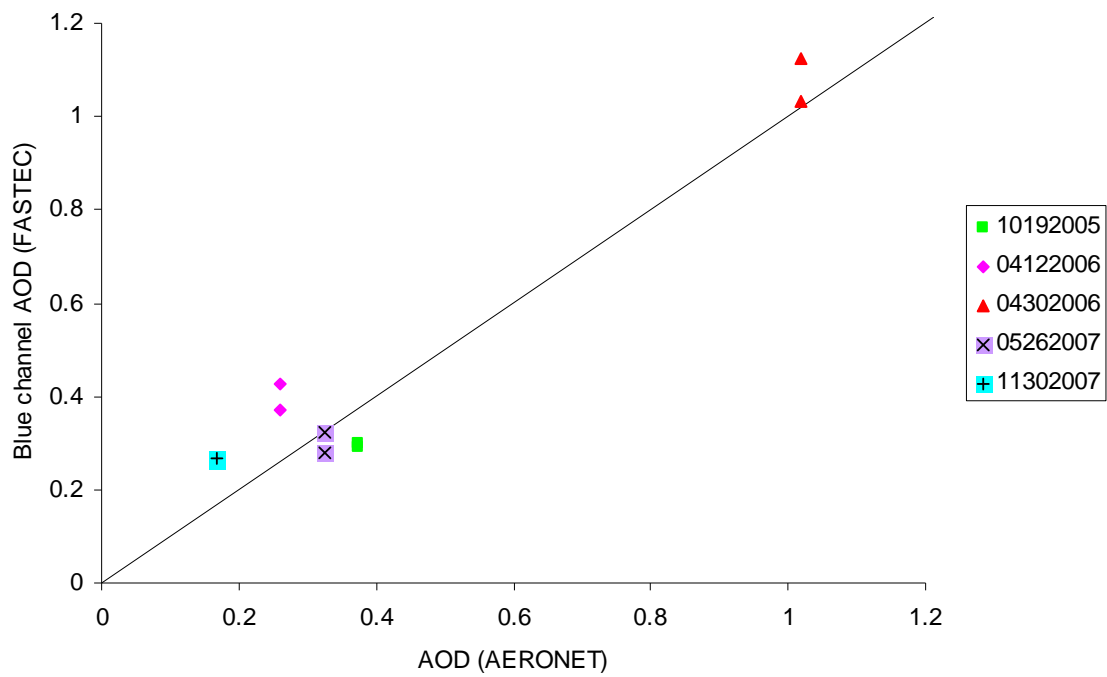


Figure 42. Blue channel AOD results for Solar Village satellite dishes.

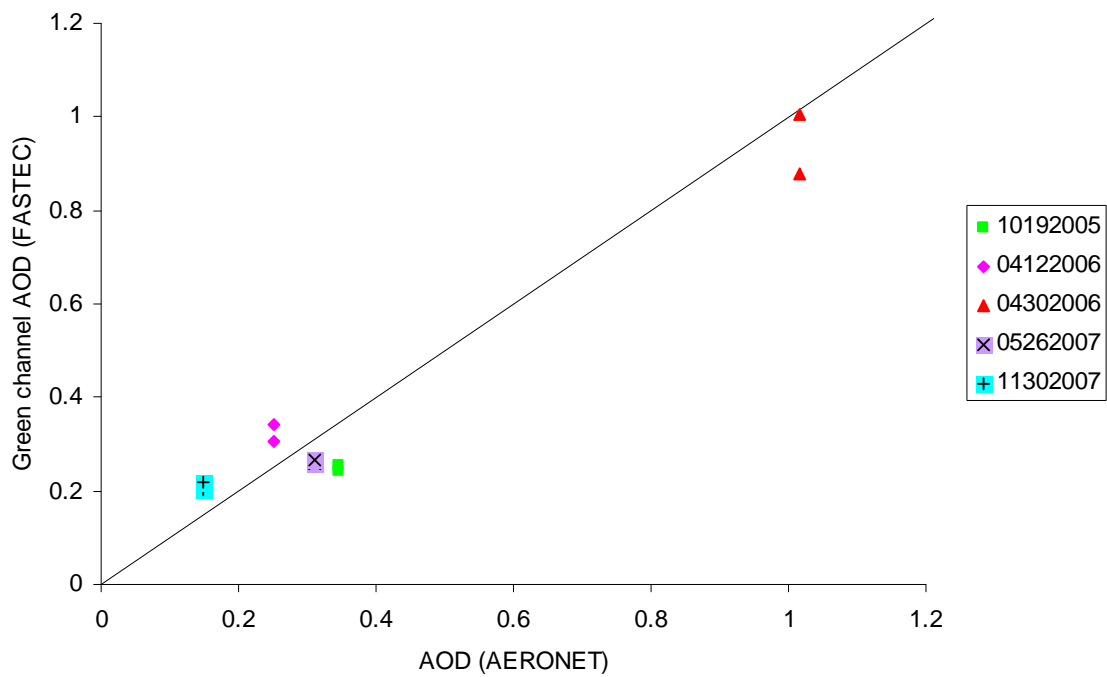


Figure 43. Green channel AOD results for Solar Village satellite dishes.

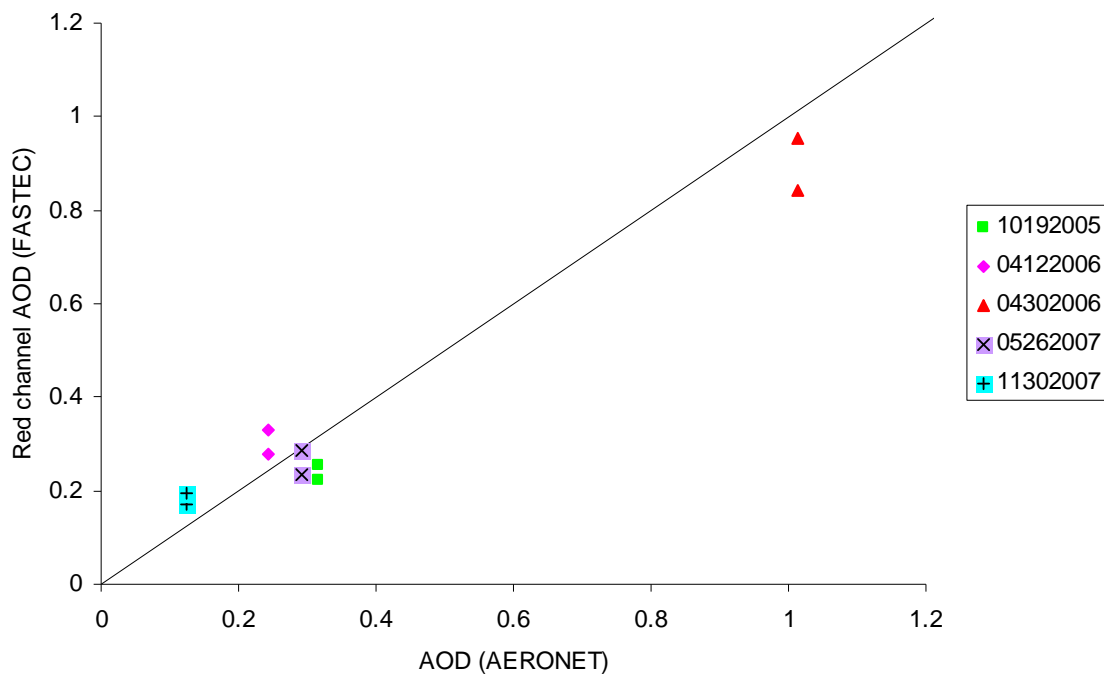


Figure 44. Red channel AOD results for Solar Village satellite dishes.

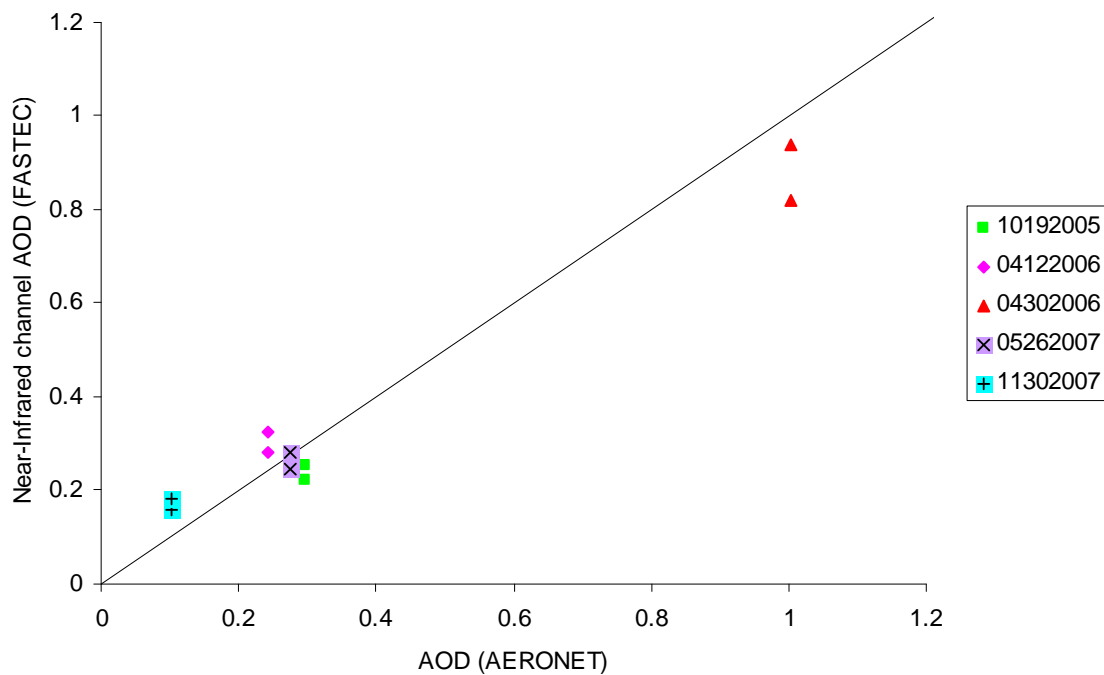


Figure 45. Near-Infrared channel AOD results for Solar Village satellite dishes.

Channel	Bias	Standard Deviation
Blue	0.043	0.078
Green	-0.006	0.078
Red	-0.008	0.079
NIR	-0.003	0.078

Table 13. Multispectral channel-specific error bias and error standard deviation Solar Village shadows.

b. Panchromatic Images

Nine panchromatic images over Solar Village were evaluated with FASTEC (see Figure 46). The satellite dishes are pointing in different directions in several of the images, most notably (F) and (I). This should affect the accuracy of the shadow found using the hand-generated Solar Village DSM with the dish orientation pointing almost straight up. Ground truth best fit curves were based on the daily average AERONET value for each image except for the April 30, 2006 image. As discussed in the previous section, level 1.0 AERONET data showed AOD increasing rapidly from about 0.7 to 1.0 around the time of the satellite image. For every other image, the AOD changed slightly with standard deviations less than 0.02 for the whole day.

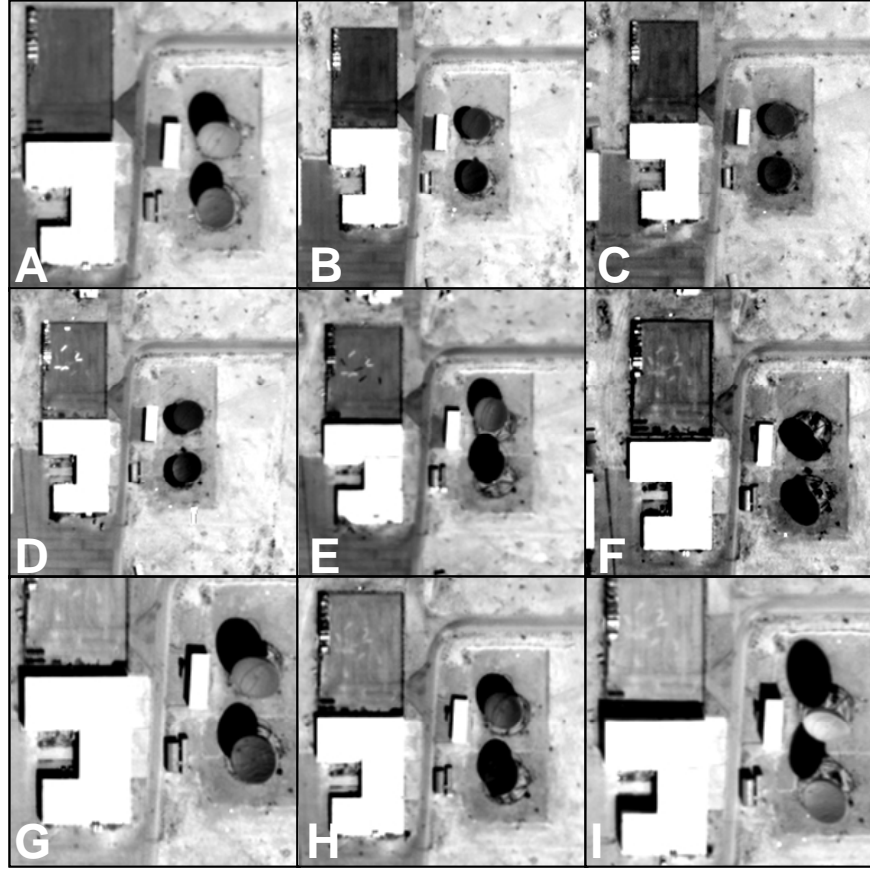


Figure 46. Panchromatic imagery for Solar Village testing on (A) October 19, 2005, (B) April 12, 2006, (C) April 30, 2006, (D) May 26, 2007, (E) November 30, 2007, (F) June 26, 2008, (G) October 11, 2008, (H) October 14, 2008, (I) December 14, 2008.

As in the multispectral images, FASTEC computed AOD for both satellite dishes in each image. Basic data on each of the scenes is provided in Table 14. Four images, collected between April and June, had relatively small shadows with fewer than 33 pixels while the others identified between 80 and 200 pixels. The horizontal resolution of WorldView-1 data (50 cm) was slightly higher than DSM resolution (64 cm) while the QuickBird imagery had the same resolution as the DSM. As in the multispectral case, the May 26, 2007 sun azimuth and elevation was incorrectly identified in the metadata file and was manually corrected to 105.2° and 77.6° respectively.

Date	Sat	Time	Sun Azimuth	Sun Elevation	Row Offset	Column Offset	Satellite Dish	Shadow Pixel Ct	Non-shadow Pixel Ct
10/19/2005	QB	0752	160.2	53.4	-14	31	1	113	643
							2	101	658
4/12/2006	QB	0754	135.4	68.4	4	-1	1	27	551
							2	33	588
4/30/2006	QB	0755	124.6	73.5	-38	14	1	13	477
							2	11	577
5/26/2007	QB	0801	105.2	77.6	-13	-2	1	6	382
							2	9	553
11/30/2007	QB	0754	164.9	42.2	4	30	1	108	469
							2	101	560
6/26/2008	WV1	0736	90.3	71.5	2	10	1	18	446
							2	20	475
10/11/2008	WV1	0743	154.6	55.1	-7	17	1	94	628
							2	82	635
10/14/2008	QB	0750	158.6	54.9	-25	-4	1	93	614
							2	83	646
12/14/2008	WV1	0746	161.3	39.7	4	22	1	199	505
							2	167	488

Table 14. Date, satellite, time, sun azimuth and elevation, offset correction, and pixel counts for the satellite dish shadows in the Solar Village panchromatic imagery.

Figure 46 is a plot comparing the AOD values found using the satellite images with AERONET. The results showed a low bias of 0.136 and an error standard deviation of 0.071 for all 18 AOD calculations. If the suspect April 30, 2006 case is removed from the sample, the low bias becomes 0.115 and the error standard deviation lowers to 0.042. Figure 48 displays the bias corrected results. Although the sample is rather small and the bias and accuracy are found using the one scene, this figure shows good agreement between ground truth and FASTEC.

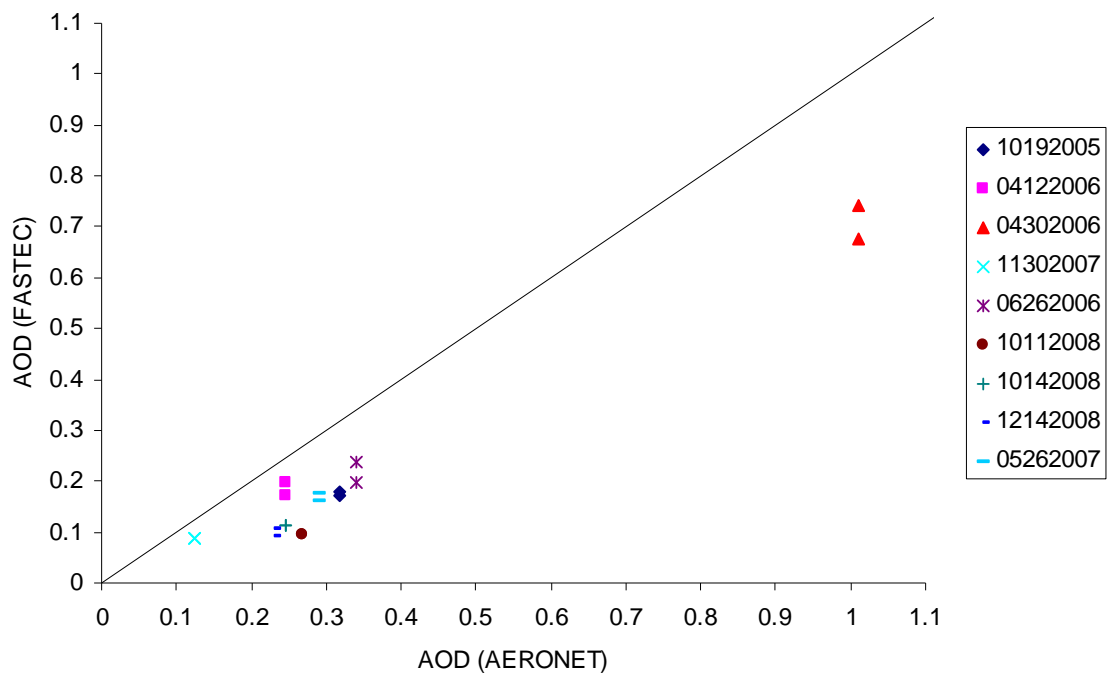


Figure 47. Panchromatic channel AOD results for Solar Village satellite dishes.

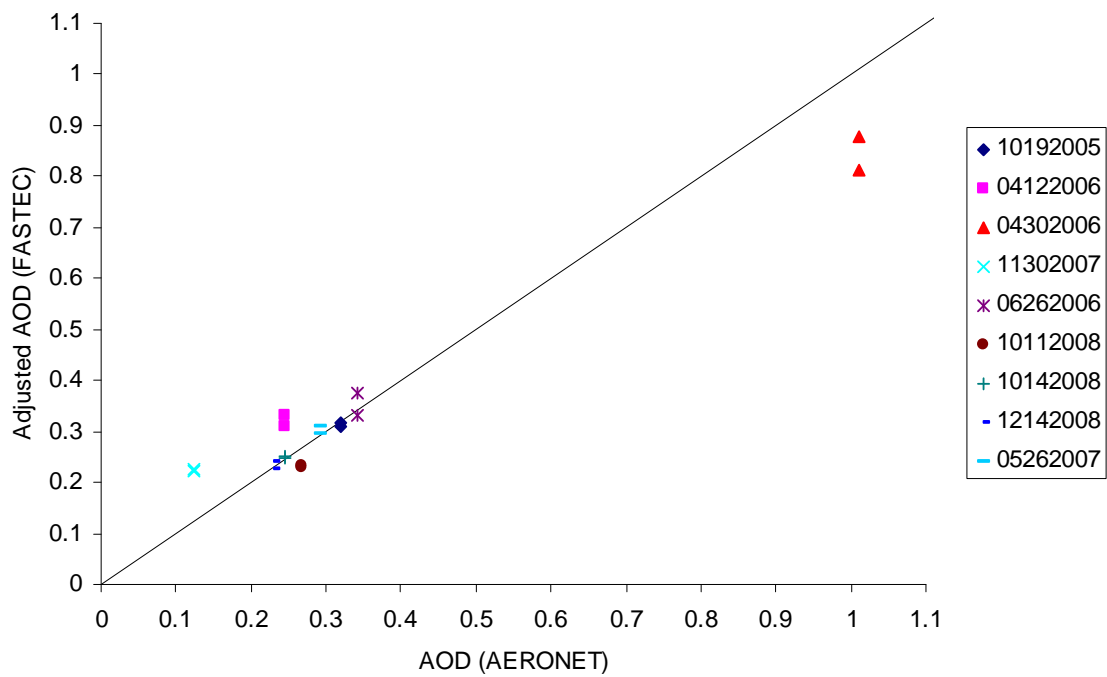


Figure 48. Panchromatic channel bias-adjusted AOD results for Solar Village satellite dishes.

2. Goddard Space Flight Center

The first full scene investigation of FASTEC using a BuckEye DSM was conducted with the approximately 5 km x 5 km Goddard Space Flight Center (GSFC) file. The region provides a mixture of urban and rural terrain with large buildings, asphalt, and forested areas (see Figure 49). Appendix E lists the configuration values where the minimum building height and minimum pixel count were set up to eliminate tree shadows. Using these settings prevented AOD calculations on all but nine buildings from the DSM, including the Goddard Space Flight Center building where the AERONET station was located and where single shadow testing in Chapter IV, Section B was performed (see upper right hand corner of Figure 49).

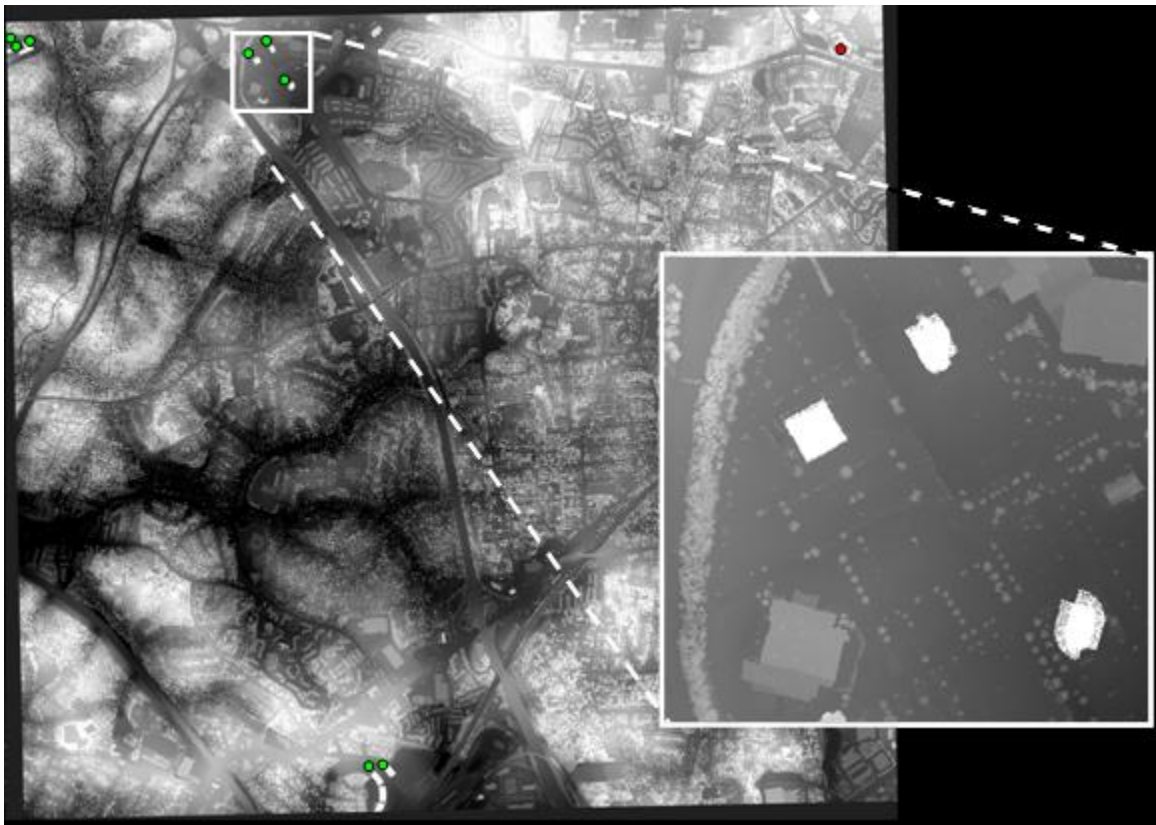


Figure 49. BuckEye DSM tile over the Goddard Space Flight Center with zoomed in view of three buildings identified as shadow generators by FASTEC. Green dots are shadow regions with sun to SE. Red dot marks location of AERONET site.

a. Multispectral Images

Two multispectral images that covered the GSFC region and coincided with AERONET data were evaluated with FASTEC. Figure 50 shows the RGB images for the zoomed in region of Figure 49. The fourth channel, at the NIR wavelength, was also evaluated (not pictured). Ground truth best fit curves were based on the daily average AERONET value for each image because AOD changed less than 0.02. Portions of the AERONET data was missing from the cloud screened data on February 8, 2009. It is easy to identify the building shadows in the October 26, 2006 image on the left while the shadows in the February 8, 2009 image on the right are covered with thick cumulus clouds.



Figure 50. Examples of multispectral imagery for GSFC BuckEye file testing from October 26, 2006 (left) and February 8, 2009 (right). Images are approximately equivalent to the zoomed in region in Figure 49.

On February 8, 2009, every usable target shadow is obscured by cloud. For 4 of the 6 target shadows, FASTEC found shadow radiance exceeded sunlit radiance and AOD was not calculated. The other target shadows calculated unrealistic AOD values, between 0.43 and 1.13 with ground truth of 0.07 for the red channel for instance. For this reason, the February 8, 2009 image was not included in the results.

On October 26, 2006 at 1621Z, the sun azimuth and elevation were 170.7° and 38.2° respectively. Offset correction shifted the DSM file eight meters east to align it with the satellite pixels. For the eight usable shadows, the average shadow region was 273 pixels while the average sunlit region was 296 pixels. The 50th percentile value of

AOD for the blue channel was slightly above ground truth while the 50th percentile value was below ground truth for the other channels (see Figure 51). For the red channel, the calculated AOD was less than zero for each of the eight shadows and the 50th percentile was 0.091 below ground truth (see Table 15). For each channel, the standard deviation was 0.078 or better. For the blue channel, the bias was noticeably above ground truth due to one shadow, which found AOD to be 0.295. Removing that shadow from the dataset brought the bias to within 0.003 of ground truth and reduced the standard deviation to 0.051.

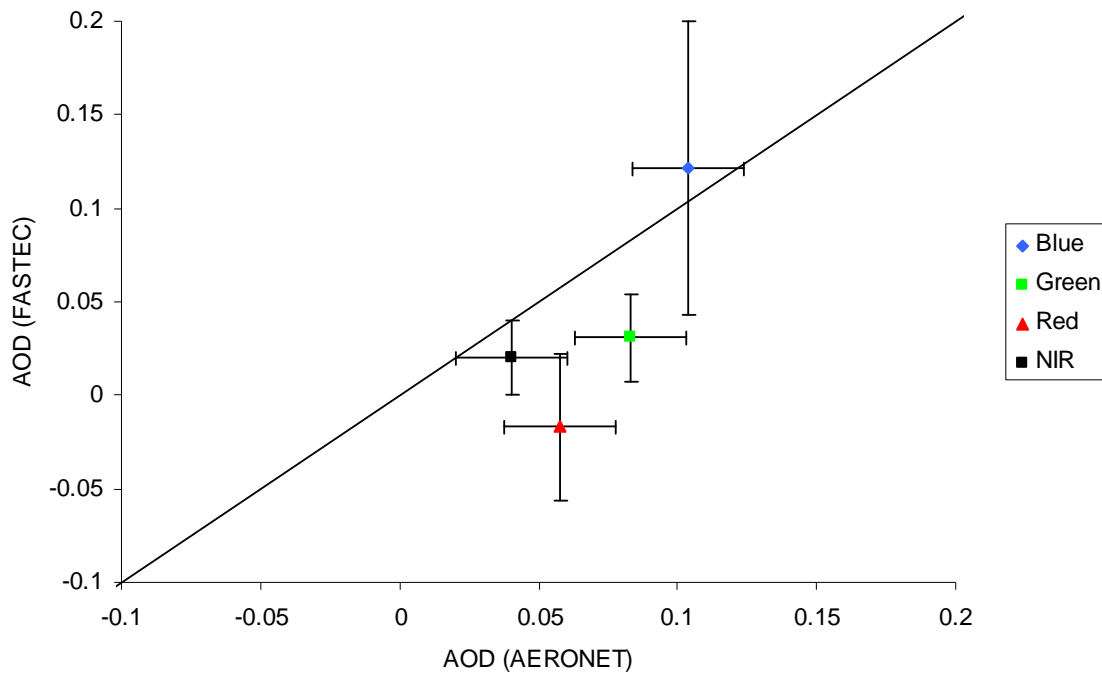


Figure 51. 50th percentile value of AOD vs. AERONET value for GSFC multispectral channels from October 26, 2006 QuickBird image. Error bars on the y-axis reflect the reported accuracy of AERONET data (0.02) and error bars on x-axis are one standard deviation of the values reported on that day and scene. $n=8$.

Channel	Bias	Standard Deviation
Blue	0.027	0.078
Green	-0.055	0.023
Red	-0.091	0.039
NIR	-0.018	0.020

Table 15. Multispectral channel-specific error bias and standard deviation for October 26, 2006 GSFC shadows.

Interesting results appear when plotting all other channels against the blue channel (see Figure 52). It is expected that AOD would decrease with increasing wavelength, however, FASTEC AOD values decreased from blue to green to NIR to red. The two exceptions were the cases where blue channel AOD was lowest. In the case where the green and blue channel had the lowest AOD values, the sunlit region included water. In the other case, green was lower than NIR but higher than red and the sunlit region was composed of pavement, grass, and cars.

The maximum and minimum blue channel AOD cases are also noticeably different than the other six cases. These extremes were primarily due to different surface types dominating the sunlit region. In the maximum blue channel AOD case, the sunlit region surface consisted primarily of grass with two sidewalks and a dirt area present. This resulted in sunlit radiance being significantly lower than the six pavement cases (36.5 RU vs. 44-50 RU). In the minimum blue channel AOD case, the sunlit region surface was primarily composed of sidewalk and water with some grass as well. This resulted in sunlit radiance being significantly higher than the six pavement cases (58 RU vs. 44-50 RU). In both the blue channel extremes, the green and NIR AOD was consistent with the other shadows. For the maximum blue channel AOD, the red channel AOD was much lower than the other shadows because its sunlit radiance was significantly lower (19 RU vs. 25-30 RU). Overall, shadow radiance varied by about 4 RU for each channel except NIR where it varied by 8 RU.

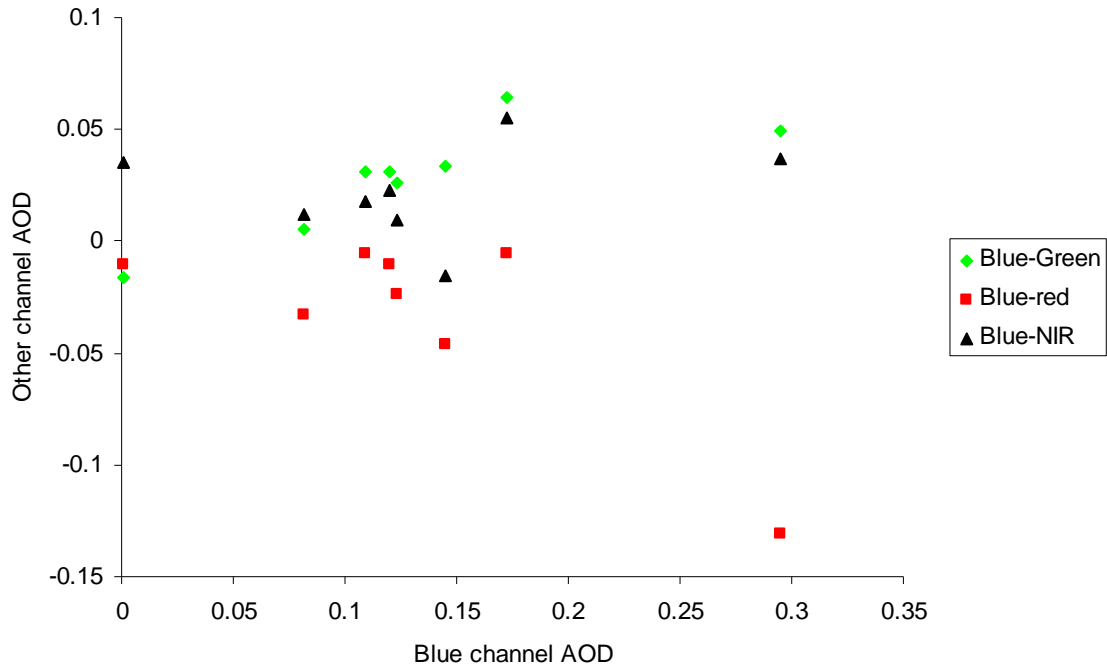


Figure 52. Plot of blue channel AOD vs. the other channels for the October 26, 2006 GSFC image.

b. Panchromatic Images

Figure 53 shows the four panchromatic images that were evaluated with FASTEC. Surface obscuring clouds were not apparent for any of the valid target shadows in the four satellite images although thin cirrus may have been present. Ground truth was determined using best fit curves based on the daily average AERONET value for each image because AOD changed by less than 0.02 for each wavelength. As explained in the multispectral section, cloud coverage over every target shadow in the February 8, 2009 led to unusable results and the image was discarded.

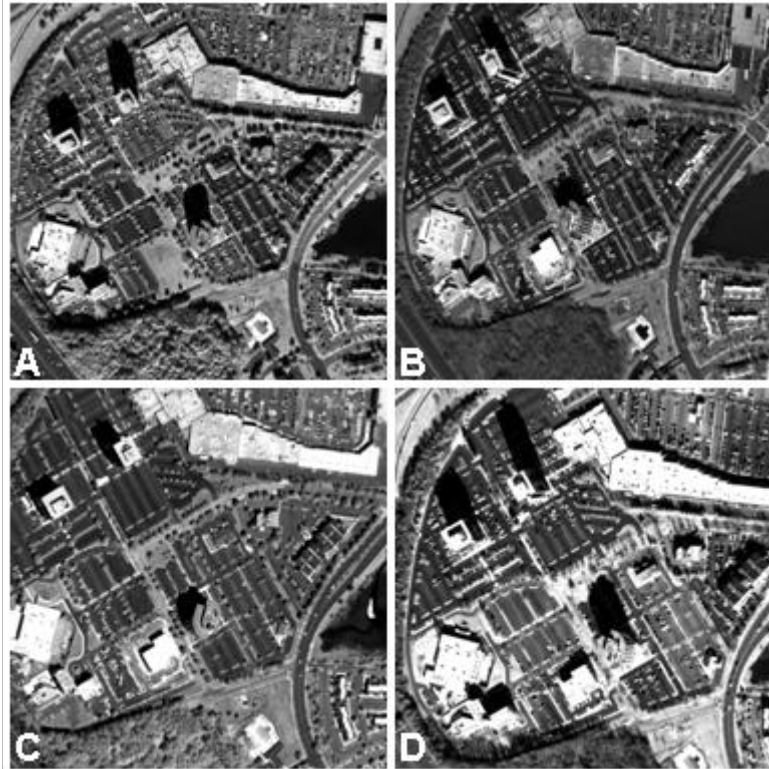


Figure 53. Examples of panchromatic imagery for GSFC BuckEye file testing from (A) October 26, 2006, (B) March 5, 2008, (C) May 25, 2008, and (D) January 16, 2009. Images are approximately equivalent to the zoomed in region in Figure 49.

In each image, FASTEC computed AOD for anywhere from three to eight shadows, depending on the overlap between the DSM file and the satellite image. Basic data is listed in Table 16 where the top image was from QuickBird, the bottom three from WorldView-1. Generally, shadow size was largest for the January 16, 2009 image where the sun elevation was lowest. Offset correction shifted the DSM between about 3 and 14 meters. The sun azimuth and elevation provided in the metadata files appeared accurate when subjectively compared with the satellite images.

Date	Time	Sun Azimuth	Sun Elevation	Row Offset	Column Offset	Shadow Count	Avg. Pixel Count	
							Shadow	Non-shadow
10/26/2006	1621	170.7	38.2	2	9	8	273	296
3/5/2008	1543	148.1	40.4	-2	3	7	215	308
5/25/2008	1606	140.8	68.4	-1	-13	4	79	332
1/16/2009	1600	159.6	27.7	-7	5	3	560	365

Table 16. Date, time, sun azimuth and elevation, offset correction, shadow count, and average pixel counts for the satellite dish shadows in the Solar Village panchromatic imagery.

Figure 54 displays the results for the four test cases. In each case, AOD values were less than 0.1, with FASTEC finding the lowest values for the May 25, 2008 image. The March 5 and January 16 images showed the 50th percentile AOD value slightly above ground truth while the other two images were below ground truth. The standard deviation of the AOD values of the May 25 image was slightly less than 0.03 while the other images were less than 0.02. Overall, the four test cases suggested a low bias of approximately 0.04. In the May 25, 2008 case, the negative AOD values occurred after removing the Rayleigh contribution.

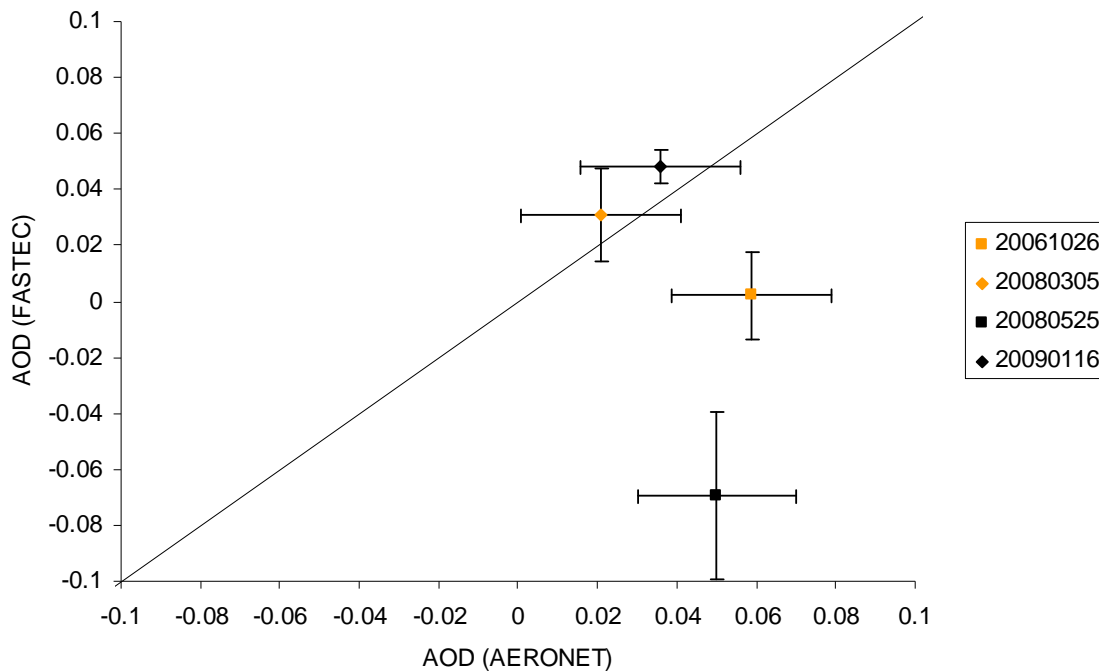


Figure 54. 50th percentile value of AOD vs. AERONET value for GSFC panchromatic images. Error bars on the y-axis reflect the reported accuracy of AERONET data (0.02) and error bars on x-axis are one standard deviation of the values reported for that day and scene.

3. Other Location Tests

a. Tucson

Tucson was chosen to test FASTEC using BuckEye DSM data in a desert region. Figure 55 shows the DSM file used for this location with the zoomed in region

showing the area surrounding the AERONET station. The configuration values were the same as those used for GSFC testing (see Appendix E). The large bright region in the southwest corner of the DSM is caused by mountainous terrain.

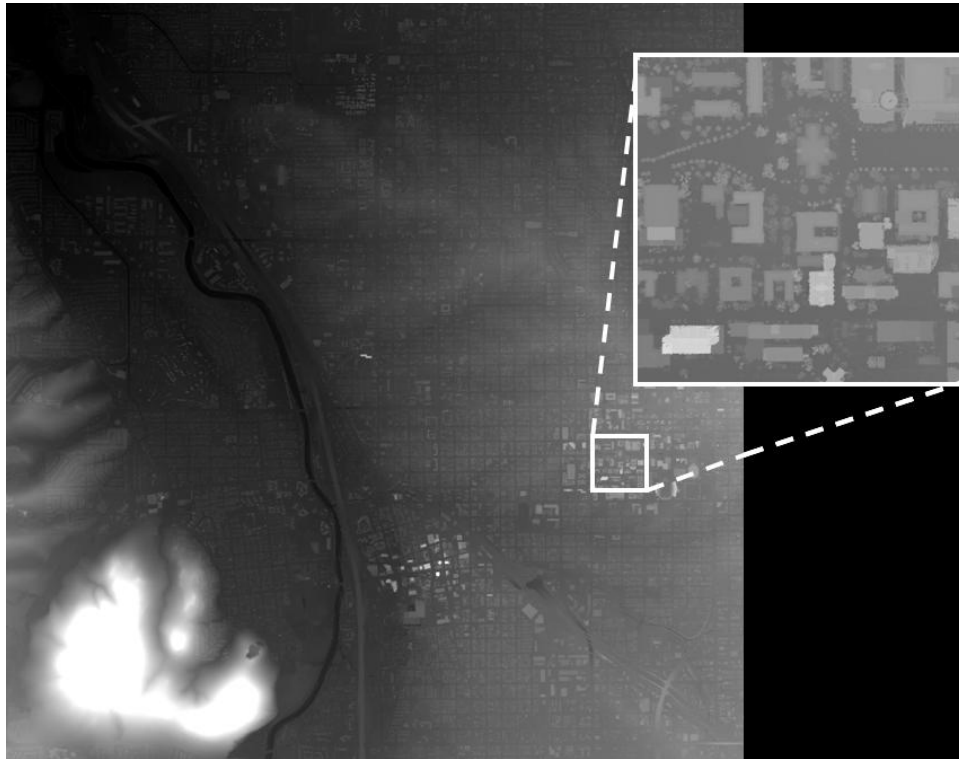


Figure 55. DSM file for Tucson testing. The inset is the area around the AERONET station, the bright area in the southwest corner is caused by mountains.

Only one available Tucson image corresponded with AERONET data. The image for that day, November 1, 2005, was comprised of the panchromatic and blue channels from the IKONOS satellite (see Figure 56). The four meter resolution blue channel is much fuzzier than the one meter resolution panchromatic channel. Ground truth was determined using best fit curves of the daily average AERONET AOD because it varied by less than 0.02 for each wavelength.

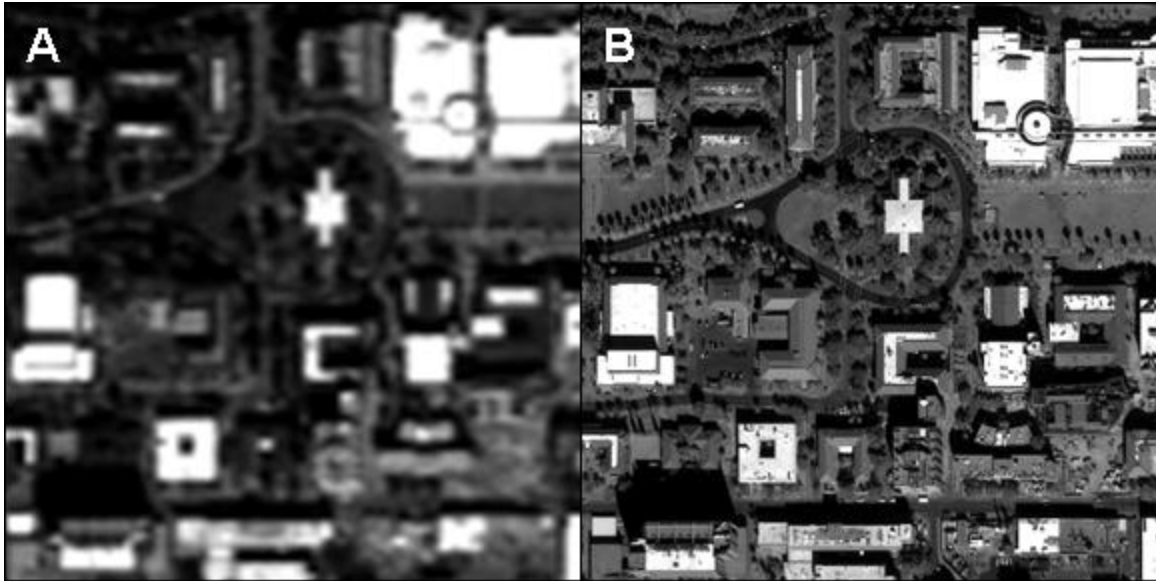


Figure 56. November 1, 2005 1815Z imagery for Tucson. Image (A) is the four-meter resolution blue channel and (B) is the one-meter resolution panchromatic channel. The area in each image roughly matches the zoomed in area in Figure 55.

FASTEC computed AOD for both channels. The sun azimuth and elevation were 163° and 41.6° respectively. Offset correction adjusted the DSM 13 rows and 24 columns for the blue channel and 14 rows and 24 columns for the panchromatic channel. Calculations were performed on 14 shadows in the blue channel with an average shadow region size of 257.3 pixels and average sunlit region size of 256.4 pixels while 3 shadows in the panchromatic channel had an average size of 199.3 shadow pixels and 214.7 sunlit pixels. The disparity in the number of targets between the two channels was because the areal extent of the panchromatic channel was much smaller than the blue channel.

The blue channel AOD values had a significant high bias of over 0.28 (see Figure 57). The standard deviation of AOD values for the blue channel was 0.055, suggesting the method found values in good agreement with each other despite being very high. It appears the high bias was caused by the poor resolution collecting data over a larger area for each pixel in the satellite image. This combined with the weighting method used to assign radiance values to the DSM pixels smoothed the pixel radiances, decreasing the radiance difference between shadow/sunlit regions, and causing AOD to

be too high. The complex city scene may amplify this problem and IKONOS multispectral imagery may work properly in scenes with more homogeneous surfaces.

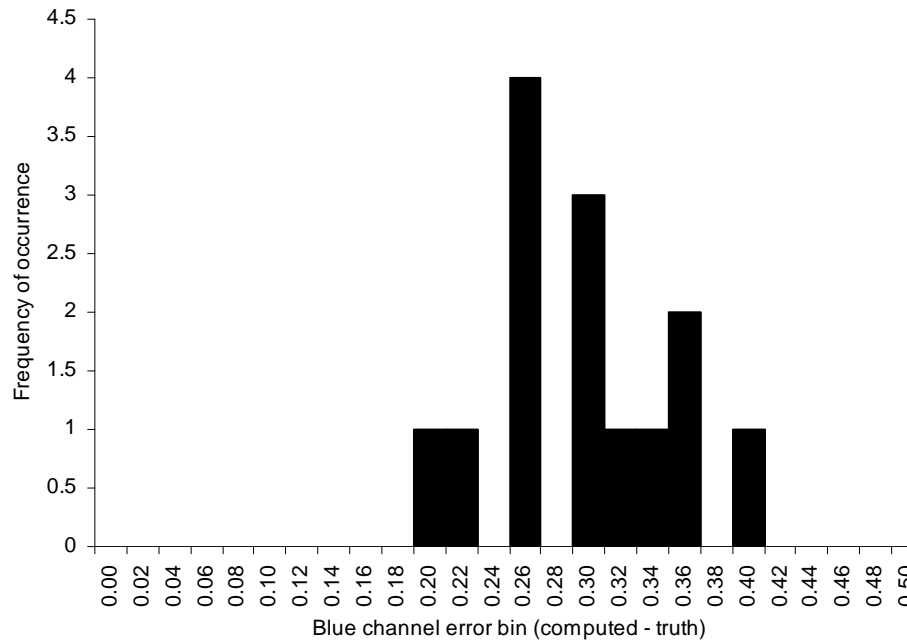


Figure 57. Histogram of blue channel AOD computation error for November 1, 2005 image. Ground truth AOD was 0.046.

The panchromatic channel expected AOD had a slight low bias of 0.029 relative to ground truth of 0.026, with each computed AOD value being slightly less than zero (-0.0045, -0.0021, -0.0008). The standard deviation of AOD values for the panchromatic channel was 0.001, showing strong agreement. The findings for this channel support the belief that the comparatively poor resolution of the IKONOS multispectral sensor may be insufficient for this scene.

b. Baltimore and Houston

Baltimore and Houston were included to test FASTEC in very complex settings with numerous shadow generators located in close proximity to each other (see Figure 58 and 59 respectively). Of the three Houston images tested, none had coinciding ground truth AERONET data while 14 of the 15 Baltimore images coincided with AERONET data. Due to problems with FASTEC in these complex settings, comparisons with ground truth were not performed.

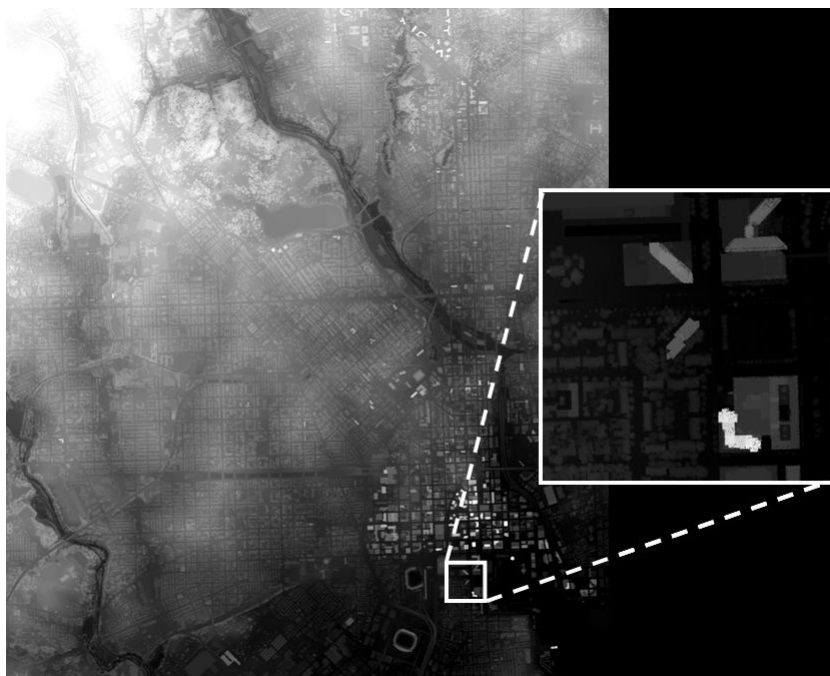


Figure 58. Baltimore DSM. The zoomed in region shows good shadow generators near the Maryland Science Center AERONET station.

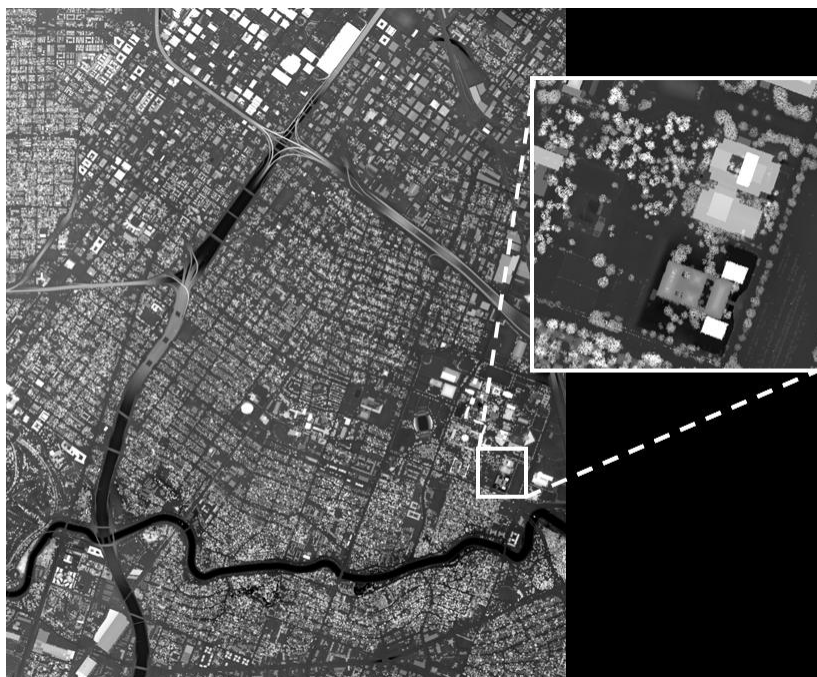


Figure 59. Houston DSM. The zoomed in region shows good shadow generators near the University of Houston AERONET station.

The Houston DSM included the downtown area with a complicated shadow patterns (see Figure 60). Although FASTEC appeared to correctly identify shadow regions, the offset correction algorithm failed to correctly align the DSM and satellite file. This led to widely varying, inaccurate AOD values. For example, the January 25, 2004 image found 24 targets for AOD calculation. 3 of the 24 had shadow radiance greater than sunlit radiance and AOD was not calculated. The other 21 targets had an average AOD in the blue channel of 0.338 and a standard deviation of 0.449. Although ground truth was not available, the comparatively large standard deviation suggested the results were invalid. When the locations of the shadows in the output file were compared with the satellite image, it was obvious offset correction failed to correctly align the satellite and DSM. Attempts to align them by hand were not successful either. The other Houston images suffered from poor offset correction as well.



Figure 60. Multispectral QuickBird image of Houston downtown area from January 25, 2004 at 1647Z. Note the complexity of shadows cast by the tall buildings.

The Baltimore DSM included the downtown area and Chesapeake Bay (see Figure 61). The large body of water further complicated the scene and contributed to the failure of offset correction and AOD values to be wrong. It is theorized that the low radiance over water offered a large area where the difference between shadow and sunlit radiance was quite small, contributing to the failure of the offset correction algorithm to properly adjust the DSM. For the January 1, 2004 panchromatic image, the average AOD was 0.305 and the standard deviation was 0.345 suggesting the results were invalid. When the location of shadows in the output file were compared with the actual shadows in the satellite image, it was apparent that offset correction again failed. In fact, offset correction failed to correctly align the DSM and satellite file in every Baltimore and Houston image although it worked properly in images from Solar Village, GSFC, and Tucson. Several attempts to manually correct for the offset failed to adequately align the images. As a result, the results from complex urban scenes were discarded for this study.



Figure 61. Panchromatic QuickBird image of Baltimore from January 1, 2004 at 1540Z. Note the complexity of shadows cast by the tall buildings and the optically dark Chesapeake Bay.

4. Summary of Whole Scene AOD Calculations

FASTEC showed promise when used in the Solar Village and GSFC scenes. In both scenes, small bias pointed to problems with accuracy but FASTEC calculated AOD values that were consistent with each other, as evidenced by standard deviations less than 0.08. Results from the GSFC scenes suggest that bias correction may work best when the surface type is known. The test of the IKONOS image in Tucson suggested the lower resolution multispectral sensor may be problematic, at least in urban settings, but the panchromatic channel appeared to work properly. The complex scenes in Houston and Baltimore highlighted problems with the offset correction procedure and identified the need to improve upon that procedure or use higher quality orthorectified satellite imagery before testing FASTEC in such complex urban settings.

C. DSM RESOLUTION ADJUSTMENT

The final test of FASTEC was designed to determine the minimum usable resolution of elevation data by reducing the horizontal resolution of the DSM. The horizontal resolution of the DSM was reduced using two methods. Method one sampled a subset of the full resolution DSM data while method two averaged the full resolution DSM data (see Figure 62). The first method is designed to simulate what the DSM might look like if a LIDAR sampled the surface with half the frequency of BuckEye while the second method was designed to simulate what the results might look like using stereo pairs DSM data.

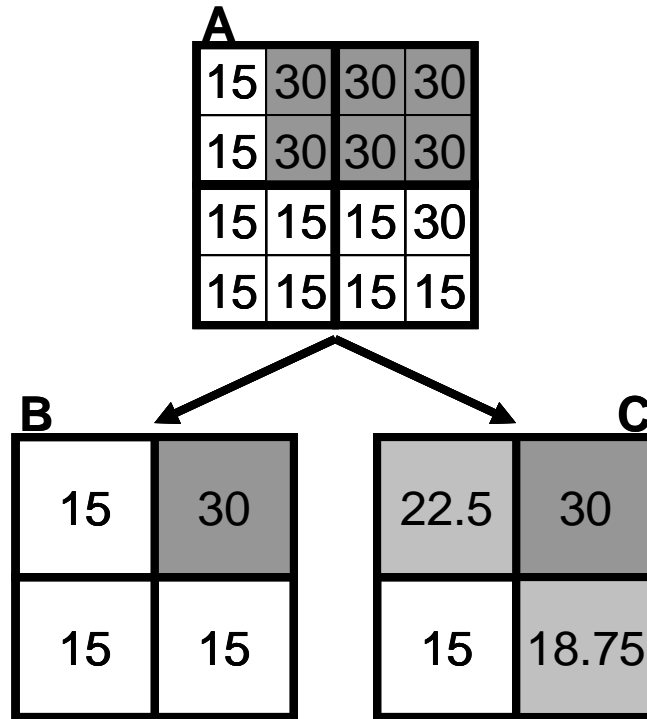


Figure 62. Example of resolution adjustment methods. Box A represents a full resolution DSM, box B and C halve the horizontal resolution using method one (sampling) and two (smoothing) respectively. Gray shading is by elevation.

1. Resolution Reduction for Solar Village Scene

Figure 63 shows examples of reduced resolution DSM images using the sampling and smoothing method with resolution reduced to 1.28 and 1.92 meters. The most notable difference between the two methods is the edges of the objects are less sharp when the smoothing method is applied. The most notable difference between the resolution changes with either method is the larger area of the full DSM that is visible in the 30 pixel by 30 pixel region. Otherwise, resolution reduction using sampling makes the edges appear sharper while smoothing makes the edges less sharp. The configuration values for this test are listed in Appendix D. Resolution reductions beyond 1.92 meters lowered the pixel count below the user-defined minimum of 5.

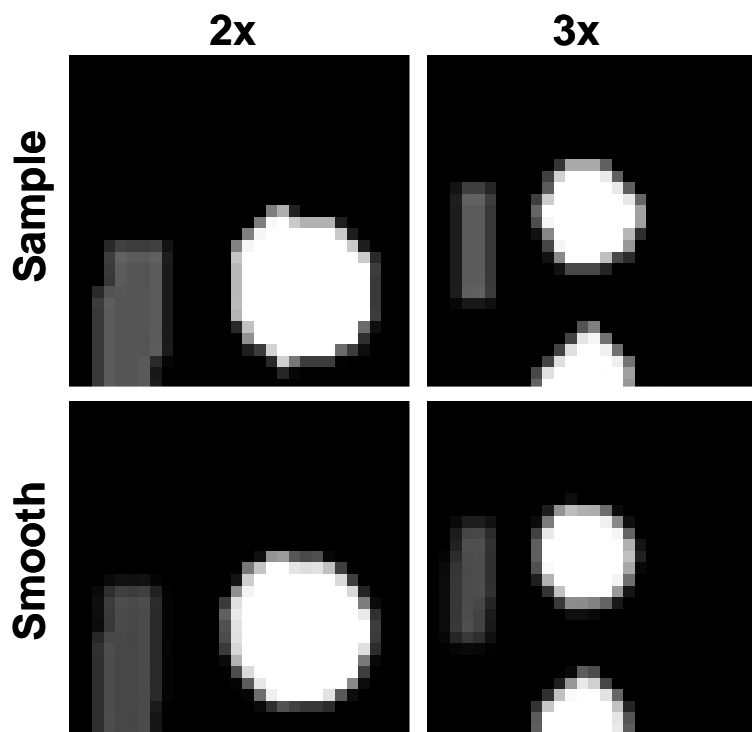


Figure 63. Examples of top left 30 x 30 pixel region in Solar Village DSM after resolution adjustment methods applied.

Table 17 displays the results of resolution reduction testing using the sampling method with the Solar Village elevation file and the multispectral satellite channels. As elevation file resolution is reduced, AOD values decrease with the overall decrease typically 0.05 for the blue channel and about 0.03 for the green, red, and NIR channels. These decreases are primarily due to decreasing shadow radiance. For example, blue channel radiance values decrease by about 1 RU for each unit of resolution decrease on dish 1 and 3 RU for each resolution change on dish 2. These cause an increase the radiance difference and decrease in computed AOD values. The fact that the changes are consistent for each shadow suggests lower resolution elevation data may still be usable, with only the bias needing adjustment.

Date	Dish	Channel	AOD w/ Resolution			
			0.64	1.28	1.92	Truth
10192005	1	Blue	0.301	0.296	0.256	0.372
		Green	0.241	0.232	0.215	0.347
		Red	0.223	0.214	0.195	0.317
		NIR	0.220	0.212	0.198	0.297
	2	Blue	0.293	0.268	x	0.372
		Green	0.253	0.232	x	0.347
		Red	0.254	0.231	x	0.317
		NIR	0.254	0.231	x	0.297
11302007	1	Blue	0.263	0.247	0.213	0.168
		Green	0.202	0.181	0.164	0.149
		Red	0.171	0.155	0.154	0.124
		NIR	0.157	0.140	0.144	0.104
	2	Blue	0.266	0.236	x	0.168
		Green	0.217	0.193	x	0.149
		Red	0.196	0.165	x	0.124
		NIR	0.181	0.156	x	0.104

Table 17. Results of Solar Village resolution reduction using sampling approach and the multispectral channels. x=insufficient pixels for calculation.

Table 18 displays the results of resolution reduction testing using the sampling method with the Solar Village elevation file and the panchromatic satellite channel. With resolution of 1.92 meters, AOD was not calculated on the southern satellite dish (Dish 2) and on the north dish on October 11, 2008. Otherwise, AOD varied less than 0.01 for every image except the November 30, 2007 image where it varied about 0.023. Variation this small suggests FASTEC works with elevation files of up to 1.92 meter resolution and possibly beyond since FASTEC stopped calculating AOD before the values changed significantly.

Results from the smoothing method (not pictured) were very similar to the sampling method with one exception. On October 14, 2008 with resolution at 1.92 meters, the Dish 1 AOD value was 0.777 because shadow radiance increased from around 55 RU to 121.4 RU with only 3 pixels. Otherwise, as with the multispectral case, the AOD value changes appear consistent for each shadow, suggesting using lower resolution data may only affect the bias of the results.

Date	Dish	AOD w/ Resolution			AERONET AOD
		0.64	1.28	1.92	
10112008	1	0.095	0.093	x	0.267
	2	0.096	0.091	x	
10142008	1	0.113	0.109	0.108	0.245
	2	0.115	0.107	x	
10192005	1	0.175	0.167	0.165	0.319
	2	0.183	0.174	x	
11302007	1	0.088	0.084	0.066	0.124
	2	0.087	0.087	x	
12142008	1	0.091	0.090	0.088	0.230
	2	0.104	0.097	x	

Table 18. Results of Solar Village resolution reduction testing using sampling approach and the panchromatic channel. x=insufficient pixels for calculation.

2. Resolution Reduction for GSFC Scene

Figure 64 shows examples of reduced resolution DSM images using the sampling and smoothing method with resolution reduced to 2 and 3 meters. Although more difficult to discern than in the Solar Village image in Figure 63, the edges of the objects are less sharp when the smoothing method is applied. This is most noticeable with the road running north-south and the trees south of the building. The configuration file was set to the values listed in Appendix E with the exception of the minimum pixel count variable that was reduced to from 100 to 6. This change was made to allow the resolution reduction algorithm to work with the expected lower pixel counts. In cases where this change caused a tree shadow to have AOD computed, the tree shadow was removed from the sample.

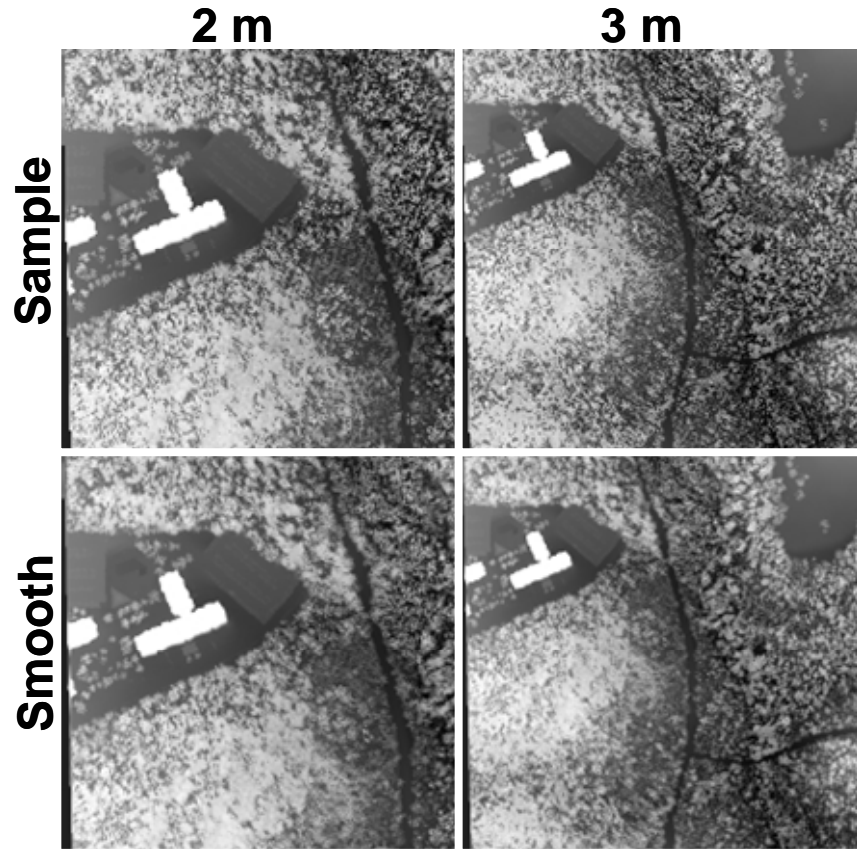


Figure 64. Examples of top left 201 x 201 pixel region in GSFC DSM after resolution adjustment methods applied.

Table 19 displays the results of resolution reduction testing on the October 26, 2006 GSFC multispectral image. The 50th percentile AOD values tend to decrease with reduced elevation file resolution, although the change is on the order of 0.02 for all channels. These decreases are primarily caused by decreasing shadow radiance that increases the radiance difference between the regions. As in the Solar Village test, the fact that the changes are consistent for each shadow suggests lower resolution elevation data may still be usable, with only the bias needing adjustment. This test suggests 4 meter horizontal resolution elevation files may be adequate for computing AOD, although lower resolution may work with very large objects in simple scenes.

DSM	Number of calcs	Blue AOD		Green AOD		Red AOD		NIR AOD	
		50%	Range (75%-25%)	50%	Range (75%-25%)	50%	Range (75%-25%)	50%	Range (75%-25%)
Full	8	0.121	0.049	0.031	0.017	-0.017	0.027	0.020	0.024
Sample 2	6	0.107	0.016	0.025	0.011	-0.017	0.010	0.017	0.016
Sample 3	5	0.106	0.045	0.021	0.007	-0.022	0.006	0.012	0.011
Sample 4	5	0.098	0.004	0.017	0.015	-0.037	0.013	0.003	0.008
Sample 5	2	0.084	0.019	0.007	0.002	-0.031	0.004	0.000	0.007
Smooth 2	6	0.110	0.021	0.026	0.010	-0.020	0.023	0.018	0.010
Smooth 3	5	0.095	0.027	0.016	0.003	-0.030	0.004	0.017	0.010
Smooth 4	5	0.088	0.028	0.014	0.004	-0.029	0.009	0.012	0.003
Smooth 5	1	0.095		0.002		-0.050		-0.016	
Truth		0.104		0.083		0.058		0.040	

Table 19. Results of October 26, 2006 GSFC multispectral resolution reduction testing.

THIS PAGE INTENTIONALLY LEFT BLANK

V. CONCLUSIONS

A. SUMMARY

FASTEC worked well for Solar Village and the Goddard Space Flight Center testing but failed to work properly for other test locations. Shadow selection criteria testing suggested it is important to remove partial shadow edge pixels from the sample. This testing also suggested it is somewhat important to eliminate pixels that are close to the building and eliminate a portion of the extremes from the shadow and sunlit regions. The results from sky dome blockage testing were inconclusive. Whole tile testing does suggest it is useful to calculate AOD over a region although the test set-up and limited data set prevented fully assessing the accuracy (bias correction) or precision (variation) of FASTEC. Finally, the DSM resolution test showed that it is possible to use lower resolution elevation files and still achieve good results. Further testing may reveal that the elevation file resolution must only be capable of discerning shadows to employ FASTEC.

Strengths of FASTEC include the speed with which this method identifies good targets, the objective determination of shadow/sunlit regions, the easily configurable nature of the algorithm, and the consistency in AOD values between targets in the same scene. When offset correction worked properly, the technique consistently calculated AOD values within 0.05 for targets in a scene. Elevation data resolution appears usable up to 4 meters depending on the scene being analyzed. This technique can fill the high surface reflectance region gap in remotely sensed AOD databases. Militarily, FASTEC could enable in-scene correction in intelligence collection and possibly influence electro-optical targeting decisions.

The primary weakness of this study is the failure of the offset correction algorithm in complex urban settings such as Houston and Baltimore. When the output of FASTEC has high standard deviation, the user should locate several target shadows to determine if the cause of the high standard deviation was due to offset correction error, the presence of clouds, or some other problem. Additionally, this study suggested the

shadow technique has bias, which may vary between channels, scenes, or surface types. Although only a few images were used in this study, the automated approach makes future, larger studies using different sensors feasible for shadow analysis. These studies should refine the bias and uncertainty of the shadow method.

FASTEC is capable of supporting operational customers or scientists. An intelligence analyst might use FASTEC to determine the optical depth of a scene and use that value to perform in-scene corrections to the image. A climatologist or numerical modeler might establish a global grid of shadow generators to feed a global aerosol database while the ability to examine detailed shadow characteristics allows researchers to determine different shadow characteristics.

B. FUTURE RESEARCH

Future research should focus on two areas: testing FASTEC with large datasets or different sensors and improving the technique itself. When it comes to large datasets, test locations should include AERONET data or another reliable, accurate means of measuring ground truth. Elevation data can come from LIDAR (as was used in this study), stereo pair imagery, or other sources capable of providing 4 meter horizontal resolution. Using large datasets may enable the user to sort results by surface type, building size, or sensor. The ability to define small sub-regions within the DSM should simplify this type of study. If the user analyzed each shadow generator in one full scene run and created configuration files around the desired target shadows, the output could be sorted for straightforward statistical analysis. Similar experiments employing different sensors with different wavelength bands or resolution are also possible. For example, hyperspectral images provide hundreds of usable wavelength bands and may even allow aerosol size characterization. Additionally, it may be possible to use lower resolution satellites exploiting mountain or cloud (if cloud top heights are known) shadows. Finally, testing FASTEC in complex urban settings with fully orthorectified satellite imagery would determine the feasibility of using FASTEC in such scenes.

There are several possible ways of improving FASTEC to include eliminating dark surfaces, applying a cloud mask, identifying isolated buildings, and improving offset

correction. Optically dark surfaces such as water or trees pose a problem for FASTEC because they could cause offset correction to fail to correctly align the elevation and satellite files. If pixels in the elevation file were identified by surface type, these regions could be avoided. Similarly, it is necessary to employ the shadow technique in cloud-free regions. Adding a cloud mask would eliminate cloud-obscured targets from the calculation and improve the technique. This mask should be applied after identifying shadow pixels but before performing offset correction. A robust cloud mask should account for the shadow cast by the cloud and block off a standard size region around the cloud to eliminate the indirect reflective affects of the cloud. Also, Vincent (2006) suggested selecting isolated shadows for AOD calculation. It may improve the technique to eliminate target shadows when other shadow generators within a user-defined area are present.

Offset correction should improve when working with fully orthorectified imagery. In addition, it may improve with the addition of a dark surface and cloud masks but additional changes may be required. First, the current method works by trying to align the shadow regions in the DSM with low radiance pixels in the satellite file. Incorporating a dark surface mask may eliminate this issue by marking these low radiance pixels *invalid* while a cloud mask would prevent high radiance cloud pixels from skewing the correction. If these masks fail to correct the problem, an alternative approach is to adjust the DSM position to maximize the radiance difference between shadow and sunlit pixels. This approach would take both shadow and sunlit radiance into account unlike the current approach that just examines shadow radiance. Additionally, it may be better to perform offset correction on each individual shadow instead of the entire elevation file. This approach would increase computation time but make each AOD calculation independent, improving the likelihood that some, or most, of the shadows are properly aligned. Regardless, correcting for the offset appears to be the biggest obstacle to implementing this algorithm operationally.

THIS PAGE INTENTIONALLY LEFT BLANK

APPENDIX A: FORTRAN CONFIGURATION VARIABLES

A. GENERAL USE VARIABLES (CITY_VARS)

Name	Description
Sat_path	Path to satellite file
DSM_path	Path to DSM file
op_path	Path to output directory
Sat_name	Base input satellite filename
DSM_name	Base input DSM filename. Do not include a “.hdr” file descriptor
Op_name	Base output filename. Makes “AOD.txt” and “.geninfo.txt” files
DSM_sr/er, DSM_sc/ec	Limits shadow search to sub region of DSM file. If set outside the bounds of the DSM file, the entire DSM file is explored.

B. SHADOW REGION VARIABLES (SHADOW_VARS)

Name	Description
DSM_min_bldg_hgt	Minimum height of shadow generator
DSM_bldg_dist	Percentage of shadow near building that is rejected
DSM_min_bldg_dist	Minimum distance of valid shadow pixel from shadow generator
rlus/rlls	Upper/lower bounds of sorted shadow pixel radiances
max_ediff	Maximum range of elevation differences among shadow pixels

C. SUNLIT REGION VARIABLES (SUNLIT_VARS)

Name	Description
DSM_u_rgn	Size of region around shadow to search for sunlit pixels

nonshad_int	Azimuth interval to use when searching for sunlit pixels
nonshad_dint	Distance interval on each azimuth for finding sunlit pixels
nonshad_ediff	Max elevation difference of sunlit pixel and shadow
rlun/rlln	Upper/lower bounds of sorted sunlit pixel radiances

D. SHADOW/SUNLIT REGION VARIABLES (SHADNON_VARS)

Name	Description
DSM_how_int	Depth of shadow edge to mark <i>invalid</i> due to edge contamination
minpix	Minimum count of shadow/sunlit pixels to calculate AOD

E. MISCELLANEOUS VARIABLES (MISC_VARS)

Name	Description
whichAz	Which azimuth (min/mean/max) in metadata file to use
whichEl	Which elevation (min/mean/max) in metadata file to use
edgeadj	Defunct
off_cor	Set to .true. to perform automated offset correction
r_off, c_off	Used to manually offset DSM row and column
offshad	Defunct
offset	Size of adjustment region for the DSM file
offchan	Offset correction sat channel (set to 1 if value exceeds # of bands)
chk	Defunct
RR	Weighting factor for nearest neighbor determination
DSM_invalid	Value to use for program identified <i>invalid</i> pixels
big_datadump	Set to .true. to dump DSM arrays to text files for detailed analysis

parallel	defunct
----------	---------

F. VARIABLES FOR DOME BLOCKAGE CALCULATION (DOME_VARS)

Name	Description
error_check	Set to .true. to perform dome blockage calculation on each pixel
domesize	Size of region around pixel to calculate dome blockage
aziinc	Azimuth increment for dome calculation
distinc	Distance increment for dome calculation
maxdomes	Maximum allowed dome blockage for shadow pixels
maxdomen	Maximum allowed dome blockage for sunlit pixels

G. AOD CALCULATION VARIABLES

Name	Description
interval	Scattering angle interval in MAR calculation
ssa	Single-scatter albedo for AOD calculation
g	Henye-Greenstein constant

THIS PAGE INTENTIONALLY LEFT BLANK

**APPENDIX B: LIST OF BASELINE USER-DEFINED VARIABLES
FOR SHADOW CHARACTERIZATION TESTS (SOLAR VILLAGE)**

0.0	DSM_min_bldg_hgt		F	off_cor
1.0	DSM_bldg_dist		0	r_off
0.0	DSM_min_bldg_dist		0	c_off
1.0	Rlus		100	offshad
0	Rlls		10	offset
1.5	max_ediff		1	offchan
15	DSM_u_rgn		T	big_datadump
3	nonshad_int		T	parallel
0.99	nonshad_dint		T	error_check
1.0	nonshad_ediff		20	domesize
1.0	rlun		10	aziinc
0.0	rlln		2	distinc
1	DSM_how_int		1.0	maxdomes
15	minpix		1.0	maxdomen
2	whichAz		10	interval
3	whichEl		0.88	ssa
200	edgeadj		0.65	g

THIS PAGE INTENTIONALLY LEFT BLANK

**APPENDIX C: LIST OF BASELINE USER-DEFINED VARIABLES
FOR SHADOW CHARACTERIZATION TESTS (GSFC BUILDING)**

15.0	DSM_min_bldg_hgt		F	off_cor
1.0	DSM_bldg_dist		0	r_off
0.0	DSM_min_bldg_dist		0	c_off
1.0	Rlus		100	offshad
0	Rlls		10	offset
1.5	max_ediff		1	offchan
15	DSM_u_rgn		T	big_datadump
3	nonshad_int		T	parallel
0.99	nonshad_dint		T	error_check
1.0	nonshad_ediff		20	domesize
1.0	rlun		10	aziinc
0.0	rlln		2	distinc
2	DSM_how_int		1.0	maxdomes
15	minpix		1.0	maxdomen
2	whichAz		10	interval
3	whichEl		0.88	ssa
200	edgeadj		0.65	g

THIS PAGE INTENTIONALLY LEFT BLANK

APPENDIX D: LIST OF USER-DEFINED VARIABLES FOR SOLAR VILLAGE AOD CALCULATIONS

6.0	DSM_min_bldg_hgt		T	off_cor
0.8	DSM_bldg_dist		0	r_off
2.0	DSM_min_bldg_dist		0	c_off
0.75	Rlus		100	offshad
0.25	Rlls		40	offset
1.5	max_ediff		4	offchan
15	DSM_u_rgn		F	big_datadump
3	nonshad_int		T	parallel
0.99	nonshad_dint		F	error_check
1.0	nonshad_ediff		20	domesize
0.75	rlun		10	aziinc
0.25	rlln		2	distinc
1	DSM_how_int		1.0	maxdomes
5	minpix		1.0	maxdomen
2	whichAz		10	interval
3	whichEl		0.88	ssa
200	edgeadj		0.65	g

THIS PAGE INTENTIONALLY LEFT BLANK

**APPENDIX E: LIST OF USER-DEFINED VARIABLES FOR
BUCKEYE FILE AOD CALCULATIONS**

35.0	DSM_min_bldg_hgt		T	off_cor
0.5	DSM_bldg_dist		0	r_off
2.0	DSM_min_bldg_dist		0	c_off
0.75	Rlus		100	offshad
0.25	Rlls		150	offset
1.5	max_ediff		4	offchan
15	DSM_u_rgn		T	big_datadump
3	nonshad_int		T	parallel
0.99	nonshad_dint		F	error_check
1.0	nonshad_ediff		20	domesize
0.75	rlun		10	aziinc
0.25	rlln		2	distinc
2	DSM_how_int		1.0	maxdomes
100	minpix		1.0	maxdomen
2	whichAz		10	interval
3	whichEl		0.88	ssa
200	edgeadj		0.65	g

THIS PAGE INTENTIONALLY LEFT BLANK

LIST OF REFERENCES

- Deuzé, J.L., et al., 2000: Estimate of the aerosol properties over the ocean with POLDER. *J. Geophys. Res.*, **105**, 15329–15346.
- Dial, G., H. Bowen, F. Gerlach, J. Grodecki, and R. Oleszczuk, 2003: IKONOS satellite, imagery, and products. *Rem. Sens. Env.*, **88**, 23–36.
- DigitalGlobe, cited June 2010a: QuickBird Imaging satellite. [Available online at <http://www.digitalglobe.com/file.php/784/QuickBird-DS-QB.pdf>]
- , cited June 2010b: WorldView-1 Datasheet. [Available online at <http://www.digitalglobe.com/file.php/785/WorldView1-DS-WV1.pdf>]
- , cited June 2010c: Basic Stereo Pair Imagery. [Available online at http://www.digitalglobe.com/index.php/48/Products?product_id=23]
- Dombrock, R. M., 2007: Automating the shadow method for aerosol optical depth retrieval. M.S. thesis, Dept. of Meteorology, Naval Postgraduate School, Monterey, CA.
- Eng-Tips, cited May 2010: Engineering spreadsheets – Excel Curve Fit Coefficients. [Available online at <http://www.eng-tips.com/viewthread.cfm?qid=184726>]
- Evans, J. R., 2007: A verification of optical depth retrievals from high resolution satellite imagery. M.S. thesis, Dept. of Meteorology, Naval Postgraduate School, Monterey, CA.
- Franke, R. and G. Nielson, 1980: Smooth interpolation of large sets of scattered data. *Int. J. for Num. Methods in Eng.*, **15**, 1691–1704.
- Frolich, C. and G. E. Shaw, 1980: New determination of Rayleigh scattering in the terrestrial atmosphere. *Appl. Opt.*, **19**, 1773–1775.
- GeoVAR, cited July 2009: Def. of Geospatial Registration Accuracy from GeoVAR. [Available online at http://www.geovar.com/inquiries/help_registration.htm].
- Gevers, T. and A.W.M. Smeulders, 1999: Color-based object recognition. *Pattern Recognition*, **32**, 453–464.
- Haywood, J.M. and O. Boucher, 2000: Estimates of the direct and indirect radiative forcing due to tropospheric aerosols: A review. *Rev. Geophys.*, **38**, 513–543.
- Heney, L. C. and J. L. Greenstein, 1941: Diffuse radiation in the galaxy. *Astrophys. J.*, **93**, 70–83.

- Holben, B. N., and Coauthors, 1998: AERONET – A federated instrument network and data archive for aerosol characterization. *Rem. Sens. Environ.*, **66**, 1–16.
- Horvath, H., 1971: On the applicability of the koschmieder visibility formula. *Atm. Environ. (1967)*, **5**, 1971.
- IKONOS, cited May 2010: IKONOS Performance/Technical Update, March 22, 2007. [Available online at http://www.geoeye.com/CorpSite/assets/docs/technical-papers/2007/Taylor_IKONOS2007JACIE_Proceedings.pdf]
- Intergovernmental Panel on Climate Change, 2001. *Climate Change 2001 – The Scientific Basis* (contribution of working group I to the Third Assessment Report of the Intergovernmental Panel on Climate Change). Cambridge University Press, Cambridge, 2001.
- , 2007. *Climate Change 2007: The Physical Science Basis* (contribution of working group I to the Fourth Assessment Report of the Intergovernmental Panel on Climate Change). Cambridge University Press, Cambridge, 2007.
- Kaufman, Y. J. and J. H. Joseph, 1982: Determination of surface albedos and aerosol extinction characteristics from satellite imagery. *J. Geophys. Res.*, **87**, 1287–1299.
- , Y. J. and C. Sendra, 1988: Algorithm for automatic atmospheric corrections to visible and near-IR satellite imagery. *Intl. J. Rem. Sens.*, **9**, 1357–1381.
- Liou, K. N., 2002: *An Introduction to Atmospheric Radiation*. Academic Press, pp. 583.
- Low, C., K. Bannerman, B. Roberston, S. Brunke, and S. Martin, 2006: Operational Exploitation of QuickBird Imagery for High Accuracy Airport Mapping. *Geoscience and Remote Sensing Symposium, 2006. IGARSS 2006. IEEE International Conference on July 31, 2006-Aug. 4 2006*, 4209–4212.
- Martonchik, J.V., D. J. Diner, R. Kahn, and B. Gaitley, 2004: Comparison of MISR and AERONET aerosol optical depths over desert sites. *Geophys. Res. Lett.*, **31**, L16102, doi:10.1029/2004GL019807.
- Odell, A. P. and J. A. Weinman, 1975: The effect of atmospheric haze on images of the earth's surface. *J. Geophys. Res.*, **80**, 5035–5040.
- Rivenbark, B. J., 2009: Investigation of panchromatic satellite imagery sensor low bias in shadow method aerosol optical depth retrieval. M.S. thesis, Dept. of Meteorology, Naval Postgraduate School, Monterey, CA.
- Robles Gonzalez C., J. P. Veefkind, G. de Leeuw, 2000: Aerosol optical depth over Europe in August 1997 derived from ATSR-2 data. *Geophys. Res. Lett.*, **27**, 955–958.

- Russell, P. B., J. M. Livingston, and E. G. Dutton, 1993: Pinatubo and pre-Pinatubo optical depth spectra: Mauna Loa measurements, comparisons, inferred particle size distributions, radiative effects, and relationship to lidar data. *J. Geophys. Res.*, **98**, 22969–22985.
- Sarabandi, P., F. Yamazaki, M. Matsuoka, A. Kiremidjian, 2004: Shadow detection and radiometric restoration in satellite high resolution images. *Geosci. and Rem. Sens. Symp.*, **6**, 3744–3747.
- Sweat, P. C., 2008: Verification of aerosol optical depth retrievals from cloud shadows using satellite imagery. M.S. thesis, Dept. of Meteorology, Naval Postgraduate School, Monterey, CA.
- TEC, 2009: LIDAR Data Readme. [Available on-line at https://tsunami.tec.army.mil/Products/LIDAR/upload/LIDAR_Data_Readme.pdf (CAC required)].
- Veefkind, J.P., G. de Leeuw, and P.A. Durkee, 1998: Retrieval of aerosol optical depth over land using two-angle view satellite radiometry. *Geophys. Res. Lett.* **25**(16), 3135–3138.
- Vincent, D. A., 2006: Aerosol optical depth retrievals from high-resolution commercial satellite imagery over areas of high surface reflectance. Dissertation, Naval Postgraduate School, Monterey, CA.
- von Hoyningen-Huene, W., M. Freitag, J. B. Burrows, 2003: Retrieval of aerosol optical thickness over land surfaces from top-of-atmosphere radiance. *J. Geophys. Res.*, **108**(D9), 4260.
- Wehrli, C. 1985: *Extraterrestrial Solar Spectrum – Publ. 615*. Physical Meteorological Observatory and World Radiation Center, Davos Dorf, Switzerland.
- Young A. T., 1980: Revised depolarization corrections for atmospheric extinction. *Appl. Opt.*, **19**, 3427–3428.

THIS PAGE INTENTIONALLY LEFT BLANK

INITIAL DISTRIBUTION LIST

1. Defense Technical Information Center
Ft. Belvoir, Virginia
2. Dudley Knox Library
Naval Postgraduate School
Monterey, California